

UNIVERSITÀ DEGLI STUDI DI PADOVA

Dipartimento di Ingegneria Industriale DII

Tesi di Laurea Magistrale in Ingegneria dei Materiali

**ADVANCED AFM TECHNIQUES TO CHARACTERIZE ALL-OXIDE
SOLAR CELLS AT THE NANOSCALE**

Relatore: **Prof. Alessandro Martucci**

Correlatore: **Prof. Alberto Vomiero**

Correlatore: **Dott.ssa Federica Rigoni**

Laureando: **ALESSANDRO FACCIN**

Anno Accademico 2018/2019

“Success is not the key to happiness.
Happiness is the key to success.
If you love what you are doing,
you will be successful.”

Albert Schweitzer

Ai miei genitori

ABSTRACT

Solar cells are the most promising renewable technology for environmentally friendly and low-cost energy production. Since the fossil-fuel based economy appears to be no longer sustainable, the interest in the photovoltaic area has been continuously increased over the last years.

Nanomaterials represent a key technology in modern devices. Low-dimensional nanostructures, targeting low cost and high-performance devices, have a great potential to be used in optoelectronic devices like photodetectors (PDs) and solar cells (SCs). Due to biocompatibility, chemical stability, non-toxicity, abundance and simple manufacturing process, metal-oxides (MOs) are attractive candidates in the photovoltaic field. A new emerging class of solar cells, known as all-oxide solar cells, is entirely based on metal-oxides semiconductors, either as thin films or nanostructures. In the last years, researchers have been working on various configurations, mostly based on n-type ZnO nanowires (NWs) covered by Cu₂O as p-type layer. NW based solar cells have been demonstrated to possess advantages in terms of electrical and optical properties over traditional thin film devices. In most of them, the NW array is embedded in a Cu₂O film, which leads to small differences compared to the thin film geometry. Core-shell all-oxide solar cells represent a novel configuration, which exploits all the benefits of the nanostructures. Fast and high-performance photodetectors are made of core-shell p-n junctions, in which a Cu₂O layer forms a conformal shell on top of the ZnO NW array.

In this work, different combinations of oxides and geometrical configurations have been tested. Hydrothermally grown NWs of n-type oxides (ZnO and TiO₂) have been conformally covered by p-type oxides (Cu₂O and Co₃O₄) by different deposition methods, like ALD, CVD and sputtering. The morphological characterization shows conformal core-shell structures, which exhibit good photodetection and photovoltaics performances. These properties have also been evaluated at the nanoscale, by the so-called conductive atomic force microscopy (C-AFM). AFM is a characterization method which allows to obtain functional imaging of surfaces, beyond morphological information with a resolution in the range of the nm. Conductive-AFM (c-AFM) is a powerful technique to obtain nano-electrical characterization related to the

morphology of the surface. Measurements in dark and under illumination allowed to obtain the local photo-electrical properties of the investigated oxide materials at the nanoscale.

TABLE OF CONTENTS

<i>ABSTRACT</i>	<i>i</i>
<i>LIST OF FIGURES</i>	<i>vi</i>
<i>LIST OF TABLES</i>	<i>xi</i>
<i>1 INTRODUCTION</i>	<i>1</i>
1.1 Solar cells.....	5
1.1.1 General principle.....	5
1.1.1.1 Basic fundamentals of semiconductors.....	6
1.1.1.2 p-n junction theory.....	12
1.1.1.3 Photovoltaic effect.....	16
1.1.2 Types of solar cells	20
1.1.2.1 Emerging PV technologies	22
1.1.2.1.1 Dye-sensitized solar cells.....	22
1.1.2.1.2 Organic solar cells	23
1.1.2.1.3 Perovskite solar cells	25
1.1.2.1.4 All-oxide solar cells.....	27
1.2 Metal-oxide semiconductors.....	29
1.2.1 Oxides in photovoltaics	29
1.2.1.1 Types of oxides.....	30
1.2.1.1.1 Zinc oxide	31
1.2.1.1.2 Titanium oxide.....	32
1.2.1.1.3 Copper oxide.....	33
1.2.1.1.4 Cobalt oxide.....	34
1.2.1.2 All-oxide Heterojunctions.....	34
1.2.1.3 Nanostructured heterojunction cells	36
1.3 Atomic force microscopy (AFM).....	39
1.3.1 General principle.....	39
1.3.2 AFM characterizations.....	41
1.3.2.1 Conductive AFM	41
1.3.2.1.1 Effect of the nanoprobe.....	42

1.3.2.1.2	Photoconductive AFM.....	44
1.3.2.2	Impedance Spectroscopy combined with AFM (IS-AFM)	45
1.4	Objectives of the thesis.....	47
2	<i>MATERIALS AND METHODS</i>	49
2.1	Synthesis.....	50
2.1.1	Synthesis techniques.....	50
2.1.1.1	Hydrothermal growth	50
2.1.1.2	Physical Vapor Deposition (PVD)	50
2.1.1.3	Chemical vapor deposition (CVD).....	51
2.1.1.3.1	Atomic layer deposition (ALD).....	52
2.1.2	Samples preparation	54
2.1.2.1	Planar Cu ₂ O/ZnO.....	54
2.1.2.2	1D Cu ₂ O/ZnO	54
2.1.2.3	Planar Co ₃ O ₄ /ZnO	56
2.1.2.4	1D Co ₃ O ₄ /ZnO.....	57
2.1.2.5	Planar Co ₃ O ₄ /TiO ₂	58
2.1.2.6	1D Co ₃ O ₄ /TiO ₂	58
2.2	Characterization.....	61
2.2.1	Electrical characterization	61
2.2.1.1	C-AFM.....	61
2.2.1.2	IS-AFM.....	65
2.2.1.3	Macro electrical measurements	66
2.2.2	Optical characterization.....	67
2.2.2.1	Spectrophotometer.....	67
2.2.2.2	Photoluminescence	68
2.2.3	Structural and morphological characterization.....	69
2.2.3.1	Scanning electron microscope (SEM)	69
2.2.3.2	X-ray diffraction (XRD).....	70
2.2.3.3	Raman Spectroscopy	71
3	<i>RESULTS AND DISCUSSION</i>	75
3.1	List of samples.....	76

3.2	Cu ₂ O/ZnO heterostructures (1D).....	79
3.3	Cu ₂ O/ZnO heterostructures (thin film).....	91
3.4	State-of-the-art p-n heterojunctions	99
3.5	Co ₃ O ₄ /ZnO heterostructures	101
3.5.1	Optical properties.....	101
3.5.1.1	Transmittance.....	101
3.5.1.2	Reflectance.....	101
3.5.1.3	Photoluminescence	104
3.5.2	Morphological and structural characterization	105
3.5.3	AFM analysis: local morphology and electrical behavior	108
3.5.3.1	Bare ZnO nanowires	108
3.5.3.2	ZnO thin film on top of ZnO NWs	112
3.5.3.3	Thin film ZnO.....	115
3.5.4	Macro electrical measurements	118
3.6	Co ₃ O ₄ /TiO ₂ heterostructures.....	121
3.6.1	Morphological and structural characterization	121
3.6.2	Optical properties.....	125
3.6.3	Electrical properties	129
3.6.4	AFM analysis: local morphology and electrical behavior	136
3.6.4.1	TiO ₂ nanowires	136
3.6.4.2	TiO ₂ -Co ₃ O ₄ core-shell nanowires.....	141
4	<i>CONCLUSIONS AND FUTURE WORKS</i>	145
5	<i>ITALIAN SUMMARY</i>	147
6	<i>BIBLIOGRAPHY</i>	151

LIST OF FIGURES

Figure 1.1 World TPES from 1971 to 2016 by fuel (Mtoe, Million Tonnes of Oil Equivalent) [3].	1
Figure 1.2 1973 and 2016 fuel shares of TPES [3].	2
Figure 1.3 World solar PV electricity production from 2015 to 2016 by area (TWh) [3].	3
Figure 1.4 Solar grid parity illustration [6].	3
Figure 1.5 Energy band diagram of conductors, semiconductors, and insulators [18].	7
Figure 1.6 Donor and acceptor levels within the forbidden energy band gap [22].	10
Figure 1.7 Carrier recombination processes in semiconductors.	11
Figure 1.8 Space charge region in a p-n junction.	13
Figure 1.9 Energy band diagram for a p-type and n type semiconductors [22].	13
Figure 1.10 Band bending for a p-n junction in equilibrium [22].	14
Figure 1.11 A p-n junction in: (a) Zero bias; (b) Forward bias; (c) Reverse bias.	15
Figure 1.12 I-V curve of a p-n junction diode [21].	16
Figure 1.13. Solar spectrum out of the atmosphere and at the sea level [31].	17
Figure 1.14. Schematic working principle of a p-n junction solar cell [34].	18
Figure 1.15. Solar cell I-V curves in dark and light [35].	19
Figure 1.16 Solar cell conversion efficiencies from 1976 to 2018 [45].	21
Figure 1.17 Schematic working principle of a DSSC [51].	22
Figure 1.18 OSC device with a bulk heterojunction active layer in normal geometry [66]. ..	24
Figure 1.19 ABX ₃ perovskite structure [71].	25
Figure 1.20 a) Schematic energy diagram of a PSC; b) Basic architecture of a normal PSC with mesoporous scaffold [75].	26
Figure 1.21 Architecture and J-V curve of an all-oxide solar cell [77].	28
Figure 1.22 Different application of oxides in PVs [79].	29
Figure 1.23 Energy band diagram of several metal oxides. The zero of energy corresponds to the vacuum level [85].	30
Figure 1.24 Schematic of ZnO crystal structures [92].	31
Figure 1.25 Crystal structure of Cu ₂ O [99].	33
Figure 1.26 Working principle of AFM [133].	40
Figure 1.27 Force behavior as function of sample-tip distance [132].	40
Figure 1.28 Schematic drawing of a C-AFM [138].	42
Figure 1.29 Effect of the tip radius on semi-log I-V curves [142].	43
Figure 1.30 Schematic set-up of IS-AFM [149].	46
Figure 1.31 Equivalent circuit model for IS-data from single oxides.	46

Figure 1.32 Equivalent circuit model for IS-data from AOSCs.....	46
Figure 2.1 Schematic diagram of a sputter deposition [153].	51
Figure 2.2 Basic schematic of the ALD process [159].	52
Figure 2.3 Sketch of the planar Cu ₂ O/ZnO heterostructure.	54
Figure 2.4 Sketch of ZnO NWs covered by Cu ₂ O thin film.	55
Figure 2.5 Schematic illustration of ZnO thin film covered by a Co ₃ O ₄ layer.	56
Figure 2.6 Sketch of ZnO NWs covered by ZnO and Co ₃ O ₄ ALD layers.	57
Figure 2.7 Schematic illustration of TiO ₂ thin film covered by a Co ₃ O ₄ layer.....	58
Figure 2.8 Annealing steps for the spin coated seed layer solution.	59
Figure 2.9 Sketch of TiO ₂ NWs covered by Co ₃ O ₄ thin film.....	60
Figure 2.10 NTEGRA AFM set-up [166].	61
Figure 2.11 Example of approach in a contact-mode AFM.....	62
Figure 2.12 Outlook of the main operations panel of Nova AFM software.	63
Figure 2.13 AFM force plot [167].....	63
Figure 2.14. Potentiostat ModuLab XM ECS (left) and Signal Access Module SAM01 (right) used coupled with AFM controller for IS-AFM measurements.	65
Figure 2.15 Diagram of signals from the beam-sample interaction and possible techniques [52].	69
Figure 2.16 Schematic illustration of the Bragg's law [173].	71
Figure 2.17 Schematic diagram of different scattering processes (adapted from [174]).	72
Figure 3.1 XRD patterns of bare ZnO NWs (a), ZnO NWs covered by 70 nm Cu ₂ O (b), ZnO and Cu ₂ O reference (c) [168].	79
Figure 3.2 Electronic band bending and photo-response mechanism of Cu ₂ O/ZnO heterojunction.....	80
Figure 3.3 Photoresponsivity of a) bare ZnO NWs, b) 70 nm Cu ₂ O/ZnO NWs and c) 240 nm Cu ₂ O/ZnO NWs [168]......	81
Figure 3.4 Sketch of the C-AFM set-up.....	82
Figure 3.5 Force curves taken on FTO substrate by applying different set-point.....	83
Figure 3.6 Local electric image of FTO (Voltage = 0.1V).	83
Figure 3.7 Dark I-V curves for FTO at different values of set-point.	84
Figure 3.8 Dark I-V curves for ZnO NWs at different values of set-point.	84
Figure 3.9 Dark I-V curves for 70 nm Cu ₂ O/ZnO NWs at different values of set-point.	85
Figure 3.10 Dark and light I-V curves for 70 nm Cu ₂ O/ZnO NWs.	86
Figure 3.11 IS-AFM data from FTO substrate.....	87
Figure 3.12 Fitting results of the IS-AFM data from FTO substrate.....	87
Figure 3.13 Cole-Cole plot of (a) bare ZnO NWs, b) Cu ₂ O/ZnO NWs.....	87
Figure 3.14 IS-AFM data from ZnO NWs.....	88
Figure 3.15 IS-AFM data from 70 nm Cu ₂ O/ZnO.	88

Figure 3.16 Macro and local I-V curves in dark for 70 nm Cu ₂ O/ZnO NWs	89
Figure 3.17 Dark and light J-V curves for Cu ₂ O/ZTF.....	92
Figure 3.18 a) Dynamic response of the J _{SC} ; b) Dynamic response of the V _{OC}	92
Figure 3.19 Backward and forward force curves taken on Cu ₂ O/ZTF.....	94
Figure 3.20 Dark I-V curves taken on different spots of Cu ₂ O/ZTF.....	95
Figure 3.21 Dark I-V curves for the ZnO layer at different values of set-point.....	95
Figure 3.22 Emission spectrum of the low-intense white LED.	96
Figure 3.23 a) Local I-V curves of Cu ₂ O ALD layer in in dark (black line) and light (red line); b) Nanoscale photocurrent profiles of Cu ₂ O ALD layer from dark/light cycles c) Local I-V curves of Cu ₂ O PVD layer in in dark (black line) and light (red line); d) Nanoscale photocurrent profiles of Cu ₂ O PVD layer from dark/light cycles.....	97
Figure 3.24 Local I-V curves of ZnO PVD layer in dark (black line) and light (red line). ..	97
Figure 3.25 Effect of light on the current for Cu ₂ O ALD layer and Cu ₂ O PVD layer.....	98
Figure 3.26 Transmittance spectra of ZnO samples before the deposition of Co ₃ O ₄	102
Figure 3.27 Transmittance spectra of ZnO samples after the deposition of Co ₃ O ₄	102
Figure 3.28 Reflectance spectra of ZnO samples before the deposition of Co ₃ O ₄	103
Figure 3.29 Reflectance spectra of ZnO samples after the deposition of Co ₃ O ₄	103
Figure 3.30 Photoluminescence spectra of ZnO samples (bare NWs and 500 nm thin film) before the deposition of Co ₃ O ₄	104
Figure 3.31 Photoluminescence spectra of ZnO samples (bare NWs and 500 nm thin film) after the deposition of Co ₃ O ₄	105
Figure 3.32 SEM images of the plane view of (a) Z1D; b) 500ZnO/Z1D, and the cross-section of c) and d) Co ₃ O ₄ /Z1D.....	106
Figure 3.33 XRD patterns of bare ZnO NWs.....	106
Figure 3.34 Sketch of the ZnO NWs and C-AFM set-up (light from the bottom).....	108
Figure 3.35 Force curve on bare ZnO NWs.	108
Figure 3.36 a) AFM surface morphology of Z1D; b) Local current map of Z1D collected with C-AFM by applying -1V.	109
Figure 3.37 Average of 10 I-V curve in dark (black line) and light (red line) for Z1D.....	110
Figure 3.38 AFM surface morphology of Co ₃ O ₄ /Z1D.	110
Figure 3.39 Local electrical image of Co ₃ O ₄ /Z1D a) BV= -2V; b) BV= +2V.....	111
Figure 3.40 Average of 10 I-V curve in dark (black line) and light (red line) for Co ₃ O ₄ /Z1D.	111
Figure 3.41 AFM surface morphology of 250ZnO/Z1D.....	112
Figure 3.42 Average of 10 I-V curve in dark (black line) and light (red line) for 250ZnO/Z1D.	113
Figure 3.43 AFM surface morphology of Co ₃ O ₄ /250ZnO/Z1D.	113

Figure 3.44 Average of 10 I-V curve in dark (black line) and light (red line) for $\text{Co}_3\text{O}_4/250\text{ZnO/Z1D}$	114
Figure 3.45 Average of 10 I-V curve in dark (black line) and light (red line) for 500ZnO/Z1D	114
Figure 3.46 AFM surface morphology of ZTF250.	115
Figure 3.47 Average of 10 I-V curve in dark (black line) and light (red line) for ZTF250.	116
Figure 3.48 Average of 10 I-V curve in dark (black line) and light (red line) for ZTF500.	116
Figure 3.49 Average of 10 I-V curve in dark (black line) and light (red line) for $\text{Co}_3\text{O}_4/\text{ZTF500}$	117
Figure 3.50 Macro I-V curves for ZTF500.	118
Figure 3.51 Macro I-V curves for Z1D, in dark (blue line) and light (red line).	119
Figure 3.52 Macro I-V curves for $\text{Co}_3\text{O}_4/\text{Z1D}$, in dark (blue line) and light (red line).	119
Figure 3.53 a) SEM plane view of T1D (compacted); b) SEM plane view of T1D; c) Cross-section of T1D (compacted); d) Cross-section of T1D; e) Cross-section of $\text{Co}_3\text{O}_4/\text{T1D}$ (compacted); f) Cross-section of $\text{Co}_3\text{O}_4/\text{T1D}$	122
Figure 3.54 SEM images of T1D and $\text{Co}_3\text{O}_4/\text{T1D}$	122
Figure 3.55 SEM cross section of TiO_2 thin film.....	123
Figure 3.56 Raman spectra of T1D.	124
Figure 3.57 Raman spectra of T1D (compacted).	124
Figure 3.58 Photoluminescence spectra of TiO_2 samples before the deposition of Co_3O_4 . 126	
Figure 3.59 Transmittance spectra of TiO_2 samples before the deposition of Co_3O_4	126
Figure 3.60 Photoluminescence spectra of TiO_2 samples after the deposition of Co_3O_4	127
Figure 3.61 Transmittance spectra of TiO_2 samples after the deposition of Co_3O_4	127
Figure 3.62 Tauc plot of T1D.	128
Figure 3.63 Forward and reverse bias configuration during the macro-electrical measurements.....	129
Figure 3.64 J-V curves carried out in dark and under 1 Sun illumination for TTF.	130
Figure 3.65 J-V curves carried out in dark (black line) and under 1 Sun illumination (red line) for $\text{Co}_3\text{O}_4/\text{TTF}$	130
Figure 3.66 J-V curves carried out in dark (black line) and under 1 Sun illumination (red line) for T1D (compacted).....	131
Figure 3.67 J-V curves carried out in dark (black line) and under 1 Sun illumination (red line) for T1D.....	131
Figure 3.68 J-V curves carried out in dark (dashed lines) and under 1 Sun illumination (solid lines) for $\text{Co}_3\text{O}_4/\text{T1D}$, $\text{Co}_3\text{O}_4/\text{T1D}$ (compacted), and $\text{Co}_3\text{O}_4/\text{TTF}$, before the deposition of metal contacts.....	133

Figure 3.69 J-V curves carried out in dark (dashed lines) and under 1 Sun illumination (solid lines) for $\text{Co}_3\text{O}_4/\text{T1D}$, $\text{Co}_3\text{O}_4/\text{T1D}$ (compacted), and $\text{Co}_3\text{O}_4/\text{TTF}$, after the deposition of metal contacts.....	133
Figure 3.70 Current density vs time during dark/light cycles of 10 s at 0 V bias voltage applied to $\text{Co}_3\text{O}_4/\text{T1D}$ compacted.....	134
Figure 3.71 Current density vs time during dark/light cycles of 10 s at 0 V bias voltage applied to $\text{Co}_3\text{O}_4/\text{T1D}$	134
Figure 3.72 Electronic band bending and photo-response mechanism of $\text{Co}_3\text{O}_4/\text{TiO}_2$ heterojunction.....	135
Figure 3.73 Force curve on TiO_2 NWs.....	136
Figure 3.74 Overlap between the surface morphology and the local current distribution of T1D (compacted).....	137
Figure 3.75 AFM surface morphology of T1D (compacted).....	137
Figure 3.76 Morphology line profile of T1D (compacted).....	137
Figure 3.77 Local current map of T1D (compacted) collected by applying 1V.....	137
Figure 3.78 Current line profile of T1D (compacted).....	137
Figure 3.79 Sketch of the contact between compacted TiO_2 NWs and the tip.....	137
Figure 3.80 Forward and backward I-V curves in dark and light for T1D (compacted).....	138
Figure 3.81 Overlap between the surface morphology and the local current distribution of T1D.....	139
Figure 3.82 AFM surface morphology of T1D.....	139
Figure 3.83 Morphology line profile of T1D.....	139
Figure 3.84 Local current map of T1D collected by applying 1V.....	139
Figure 3.85 Current line profile of T1D.....	139
Figure 3.86 Sketch of the contact between TiO_2 NWs and the tip.....	139
Figure 3.87 Average of 10 I-V curves in dark (black line) and light (red line) for T1D.....	140
Figure 3.88 Local current map of $\text{Co}_3\text{O}_4/\text{T1D}$ collected with C-AFM by applying -2V (dark).....	142
Figure 3.89 Local current map of $\text{Co}_3\text{O}_4/\text{T1D}$ collected with C-AFM by applying +2V (dark).....	142
Figure 3.90 Local current map of $\text{Co}_3\text{O}_4/\text{T1D}$ collected with C-AFM by applying -2V (light).....	142
Figure 3.91 Local current map of $\text{Co}_3\text{O}_4/\text{T1D}$ collected with C-AFM by applying +2V (light).....	142
Figure 3.92 Dark and light local I-V curves for $\text{Co}_3\text{O}_4/\text{T1D}$ and $\text{Co}_3\text{O}_4/\text{T1D}$ (compacted).....	142
Figure 3.93 Dark and light local I-V curves for $\text{Co}_3\text{O}_4/\text{FTO}$	143

LIST OF TABLES

Table 1.1 All-oxide solar cells and their photovoltaic performance.	35
Table 1.2 Nanostructured Cu ₂ O/ZnO solar cells and their photovoltaic performance.....	37
Table 2.1 Main parameters and achieved thicknesses of the ALD layers.....	56
Table 2.2 ALD parameters used in the synthesis of 1D Co ₃ O ₄ /ZnO.	58
Table 2.3 Summary table of the different Co ₃ O ₄ /TiO ₂ architectures.	60
Table 2.4 Specific features of diamond coated conductive probes.	64
Table 3.1 List of samples having ZnO as n-type material.....	76
Table 3.2 List of samples having TiO ₂ as n-type material.	78
Table 3.3 Forces [nN] applied on the different zones of Cu ₂ O/ZTF.....	94
Table 3.4 Energy band gap of the different samples, calculated through the Tauc plot.	128

1 INTRODUCTION

One of the most discussed topics and issues for today's research relies on the global environment need of a better treatment. Therefore, during the last years, the attention to sustainability has been continuously increased. A remarkable change concerning electricity production has been occurring since the fossil-fuel based economy appears to be no longer sustainable, mainly because of economic, political and environmental reasons. The currently used non-renewable energy sources (i.e., coal, petroleum, and natural gas) cannot effort the increasing global demand of energy and, besides, the global warming effects are strictly related to them [1]. According to the Intergovernmental Panel on Climate Change (IPCC), it is clear that human activities are responsible for the global warming in so far as it can be ascribed to the raised concentration of CO₂ and greenhouse gases (GHG) in the atmosphere over the last two centuries [2]. The GHG emissions are mainly the result of burning fossil fuels used in the production of energy, and this leads towards a necessary transition to a more "green" economy.

Large-scale implementation of renewable energies can give a substantial contribution to this changing, even though fossil fuels will, unfortunately, remain the primary source of energy for the next decades. Indeed, despite the awareness of the consequences of fossil-fuel extensive use, their employment increased during the last decades (*Figure 1.1*) as well as the global investments connected to them [3].

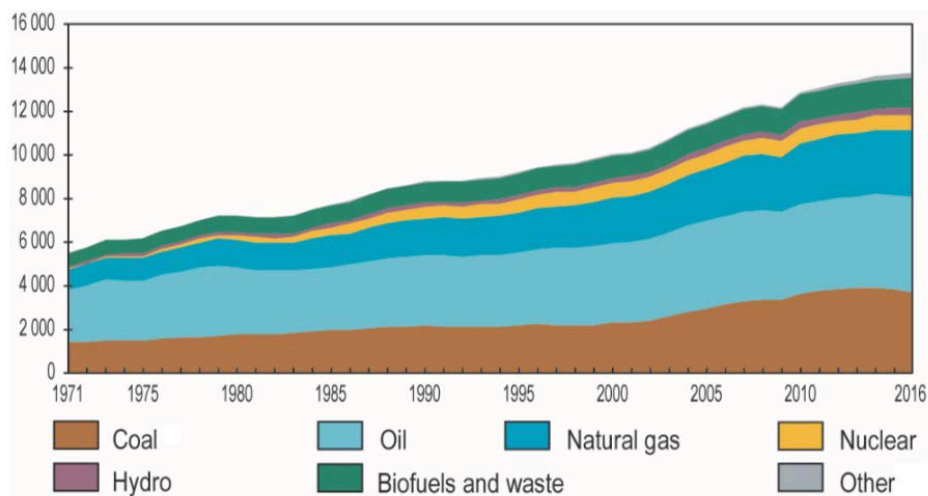


Figure 1.1 World TPES from 1971 to 2016 by fuel (Mtoe, Million Tonnes of Oil Equivalent) [3].

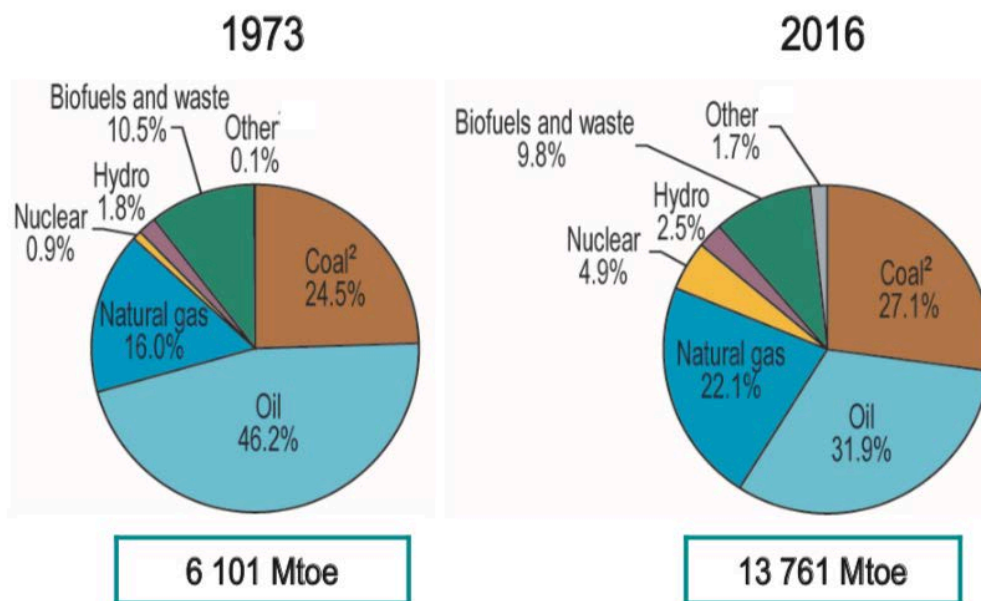


Figure 1.2 1973 and 2016 fuel shares of TPES [3].

As mentioned earlier, the world total primary energy supply (TPES) has been increasing, and renewable energies have undergone a considerable increase as well (*Figure 1.2*). The segment "other" in the graph includes geothermal, solar, wind, ocean and heat and it reached 1.7% over the last 40 years [3]. However, its contribution remains too small with respect to oil and coal. Therefore, in spite of the significant development and the growing investments in the field of renewable energies, a further increase of the production and the diffusion of these clean energy sources is essential to reduce both the global warming and the air pollution [4].

Renewable energy sources involve natural phenomena such as sunlight, hydropower, wind and geothermal heat. These natural sources exist over wide geographical areas, in contrast to the non-renewable ones, which are concentrated in a small number of countries. Among all these types of renewable and sustainable sources, solar energy plays a key role, being a clean, abundant, climate-friendly and inexhaustible energy resource [5]. Solar power can be exploited in several ways, from photovoltaics applications to solar fuels. Photovoltaics (PV) technologies, namely the use of semiconductors to convert sunlight directly into electricity, have been continuously growing over the last years. In particular, photovoltaics grew fastest in China, Japan and OECD (*Organisation for Economic Co-operation and Development*) members, including Italy and Germany (*Figure 1.3*). According to 2016 data, almost a quarter of

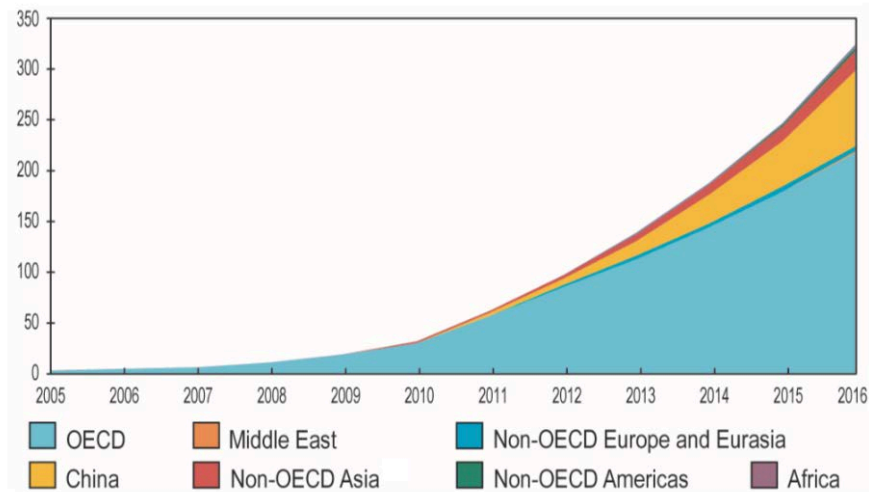


Figure 1.3 World solar PV electricity production from 2015 to 2016 by area (TWh) [3].

the global production of solar PV electricity occurs in China, whereas Italy has the highest share (7.6%) worldwide of solar PV in total domestic electricity generation [3].

Nevertheless, solar energy was never able in the past to economically compete with traditional non-renewable technologies because of the high solar panels production costs and their relatively low efficiencies. Only in the last years, PV has reached the grid parity (*Figure 1.4*), a key factor of the competitiveness of renewable technologies with respect to the conventional electricity sources [6].

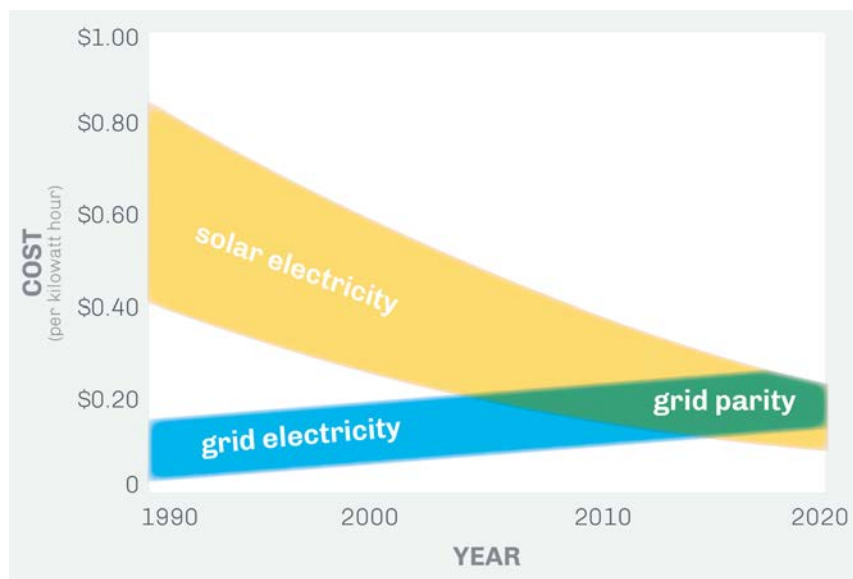


Figure 1.4 Solar grid parity illustration [6].

The drop of the renewable energy technologies cost and the simultaneous prizes raise of the fossil fuels as a source of electricity have led to the achievement of the grid parity and faster adoption of renewables. Over the last decade, the development of the PV market has been extraordinary. The global cumulative installed capacity raised from 23 GW (2009) to 138.9 GW (2013), an amount capable of producing 160 TWh of electricity every year [5].

The costs of solar energy have been already falling rapidly; however, to achieve a full competitiveness of PV energy worldwide (in particular in those regions where the sunlight is lower) and to reduce the price of electricity generated by PV panels, research is required to improve their conversion efficiency and minimize the material usage. In this context, nanomaterials have been successfully used to improve the performance and efficiency of PVs [7].

Before analyzing the new emerging technologies in the PV field and some interesting results related to them, this thesis work goes through a brief discussion about the solar cells working principle and a novel way to characterize optoelectronic devices, the so-called *conductive atomic force microscopy* (C-AFM), is dealt in detail.

1.1 Solar cells

A solar cell is a junction made of semiconducting materials capable of converting light into electricity exploiting the photovoltaic effect. The starting point for this alternative source of energy came in 1839 when the photovoltaic effect was observed by Alexandre Edmond Becquerel using an electrode in a conductive solution exposed to light [8]. In 1876 William Grylls Adams and Richard Day pointed out the same behavior in solidified selenium, but it was not until 1883 that the first solar cell, made from selenium wafers, was produced by Charles Fritts [9]. However, solar cells become well known only in 1905, year of Albert Einstein's publication about the photoelectric effect (i.e., emission of electrons after light exposition). Using this last discover, Daryl Chapin, Calvin Fuller, and Gerald Pearson built the first modern photovoltaic cell at Bell Labs in 1954 [10]. The first ever silicon solar cell had a low conversion efficiency (about six percent efficient), and the high cost was suitable only for aerospace applications. In 1956 the first solar cells were available commercially.

Nowadays, the two most significant issues concern the efficiency and cost. The price has dropped over the past ten years, and the new emerging technologies have led to outstanding results relating to efficiency, which went above 40% in multi-junction solar cells [11].

1.1.1 General principle

In a solar cell, light from the sun is transformed into electrical energy. The process involves two fundamentals steps:

- Absorption of photons making up the light by transferring their energy to the charge carriers (electrons and holes) within the semiconducting materials.
- Separation and extraction of the charge carriers through an external circuit.

A built-in potential barrier in the cell works on these carriers to produce a voltage (the so-called photovoltage), which can be exploited to drive a current through a circuit [12].

Solar cells are mainly made of semiconducting materials. In a semiconductor, absorption of sunlight occurs by the excitation of electrons across the bandgap, the

forbidden region between the valence band and the conduction band. This physical phenomenon leads to the generation of a free electron (negative charge carrier) in the conduction band and a free hole (positive charge carrier) in the valence band. In normal conditions, the excited electrons relax back quickly to their original state or recombine spontaneously with the holes. Before this happens in the material, the task of the photovoltaic device is to separate the two charge carriers and force them to recombine through an external circuit, where the energy difference between the two can be used [13].

This task is solved by the electric field of the p - n junction. When an n-type semiconductor and a p-type semiconductor are joined together, they form a p-n junction. If the regions are composed of the same material, the junction is called homojunction, while when the materials are different, the junction is called heterojunction. To explain how a p-n junction works, a quick clarification of the physics of semiconductors is needed.

1.1.1.1 Basic fundamentals of semiconductors

Semiconductors are materials having conductivities between those of insulators and metals [14]. The atoms in a semiconductor come from either group IV of the periodic table, or from a combination of group III and group V (called III-V semiconductors), or from group II and group VI (called II-VI semiconductors) [15]. The most commonly used semiconducting material is silicon (Si, group IV), which has the most developed technology and most solar cells are made of it.

In a solid, electrons have energies which are quantified and grouped in bands containing allowed energy levels and separated by forbidden bands. At temperature $T = 0$ K, the system tends to minimize its total energy and the electrons fulfill energy levels from the lowest level to a level depending on the semiconductor. The energy level above which there are no occupied states at $T = 0$ K is known as the Fermi level (E_F). The highest energy band containing electrons at 0 K is called the valence band, while the band directly above the valence band is called the conduction band [16]. The gap in energy between the top of the conduction band and the bottom of the valence band is known as the band gap (E_g). On the ideal case, electrons are not allowed to move inside the band gap. However, electrons may be excited by photons having

energy greater than the energy gap. To make this possible, the band gap must be narrow, and the semiconducting materials have to be doped to create energy levels in the forbidden band.

The band theory governs the electronic characteristics of solids. The solids can be electrically classified as conductors, insulators, and semiconductors [17]. In a conductor, the conduction band is partially filled, or the two bands are overlapped, letting electrons free to move. Insulators, by contrast, have a wide band gap (≥ 5 eV) and essentially no electrons can be promoted to the conduction band. Its valence band is completely full of electrons while the conduction band is completely empty. A semiconductor is characterized by a relatively narrow band gap (~ 1 -2 eV) and, at low temperature, behaves like an insulator (*Figure 1.5*). At higher temperature, however, there is a reasonable probability of electron excitation from the valence band to the conduction band so that electrons can play a role in the current in the conduction band. The promotion of an electron leaves a hole in the valence band, creating an electron-hole pair responsible for the current when an electric field is applied [16].

Semiconductors are commonly divided into intrinsic and extrinsic. An intrinsic semiconductor is an undoped semiconductor, where the dopant species or impurities are negligible compared with the thermally generated carriers.

For intrinsic semiconductors, the electron density in the conduction band is given by:

$$n = \int_{E_C}^{\infty} N_C(E) \cdot F(E) dE \quad (1.1)$$

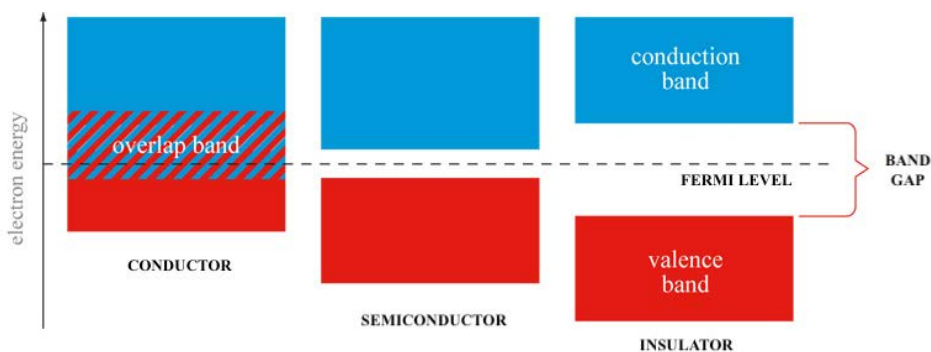


Figure 1.5 Energy band diagram of conductors, semiconductors, and insulators [18].

where:

- $N_C(E)$ is the density of states, which physically represent the allowed energy state per unit volume in the conduction band.
- $F(E)$ is the Fermi Dirac distribution, which provides the probability that an electron occupies an energy level at energy E .

The Fermi-Dirac distribution function is defined as:

$$F(E) = \frac{1}{1 + \exp\left(\frac{E - E_F}{kT}\right)} \quad (1.2)$$

where:

- k is the Boltzmann constant
- T is the temperature [Kelvin]
- E_F is the Fermi energy.

Similarly, in the valence band, the hole density is:

$$p = \int_{-\infty}^{E_V} N_V(E) \cdot (1 - F(E)) dE \quad (1.3)$$

Through the Boltzmann statistics and the Fermi Dirac integral, n and p can be written as:

$$n = N_C \exp\left(-\frac{E_C - E_F}{kT}\right) \quad (1.4)$$

$$p = N_V \exp\left(-\frac{E_F - E_V}{kT}\right) \quad (1.5)$$

where N_C and N_V are, respectively, the effective density of states in the conduction band and the valence band. Therefore, the product of p and n in a semiconductor under thermodynamic equilibrium is given by:

$$pn = N_C \exp\left(-\frac{E_C - E_F}{kT}\right) N_V \exp\left(-\frac{E_F - E_V}{kT}\right) = N_C N_V \exp\left(-\frac{E_g}{kT}\right) = n_i^2 \quad (1.6)$$

where n_i is known as intrinsic carrier concentration and E_g is the energy gap [19].

Every hole in the valence band corresponds to an electron in the conduction band, in the precisely equal number ($p = n = n_i$). The value of n_i for pure semiconductors ($n_i \sim 10^6 \div 10^{13} \text{ cm}^{-3}$) is significantly lower than the concentration of electrons in a metal ($n \sim 10^{22} \text{ cm}^{-3}$) leading to a considerable difference in conductivity [20]. The intrinsic carrier concentration is a function of temperature ($n_i = 0$ at $T = 0K$) and the band gap. When the temperature is raised, a high number of electrons gather sufficient thermal energy to leave the valence band and become free to move in the conduction band. An equal number of holes can move in the crystal and contribute to electrical current as well. Hence, the temperature and the number of carriers act as conduction promoter [19].

An extrinsic semiconductor is a semiconductor doped by impurity atoms which profoundly modify its electrical properties, making it suitable for electronic applications (e.g., transistors and sensor) or optoelectronic applications (e.g., solar cells and detectors). By doping with some other elements, p-type and n-type semiconductors can be formed [21].

Dopants with one more valence electron than group IV atoms result in an n-type semiconductor. These impurities are group V elements in the periodic table, and they have energy levels slightly below the conduction band. Four electrons form covalent bonds with the valence electrons that group IV atoms have, whereas the extra valence electron is free to move, and it participates in conduction. Thus, they are also known as donors.

Atoms with one less valence electron are used to produce p-type semiconductor. These dopants are group III elements in the periodic table, and they have energy levels slightly above the valence band. P-type material has only three valence electrons available to form bonds with group IV atoms. The net result is a hole in the conduction band, resulting from the promotion of an electron in the new energy level introduced by the dopants (in this case, they are called acceptors) (*Figure 1.6*) [22].

Therefore, in doped material, it's possible to distinguish majority and minority carriers. In n-type semiconductors, the majority carriers are electrons, which are primarily responsible for current transport, while the less abundant charge carriers are

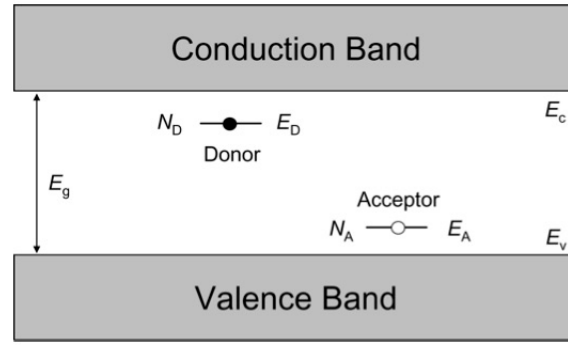


Figure 1.6 Donor and acceptor levels within the forbidden energy band gap [22].

holes. Vice versa, in p-type semiconductors, the higher concentration carriers are holes, while the minority are electrons.

For extrinsic semiconductors, the dopant concentration (N) is always far higher than the intrinsic carrier density (n_i). In the case of n-type semiconductors, the electron density (n) is close to the donor concentration (N_D). Since the law of mass action (1.6) is always valid, the hole density (p) can be written as:

$$p = \frac{n_i^2}{N_D} \quad (1.7)$$

The Fermi level for a n-type semiconductor is then:

$$E_{Fn} = E_C - kT \ln \frac{N_C}{N_D} \quad (1.8)$$

On the contrary, in p-type semiconductors, the hole density is close to the acceptor concentration (N_A). Therefore:

$$n = \frac{n_i^2}{N_A} \quad (1.9)$$

The Fermi level for a p-type semiconductor is:

$$E_{Fp} = E_V + kT \ln \frac{N_V}{N_D} \quad (1.10)$$

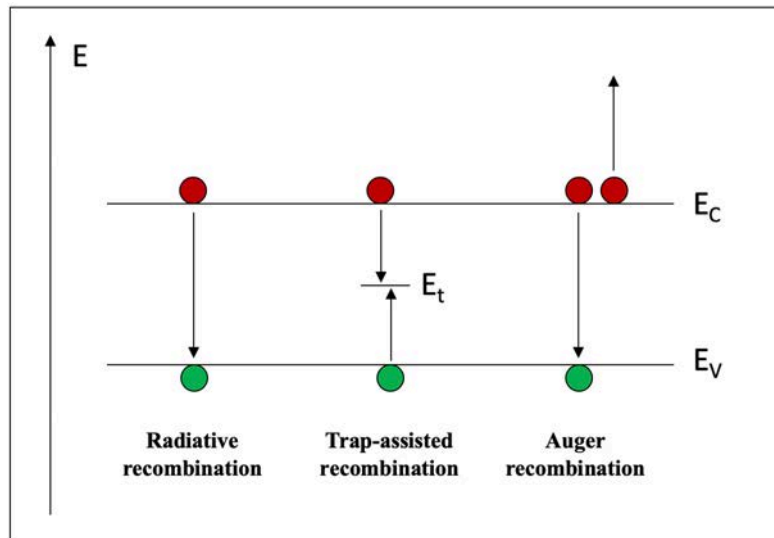


Figure 1.7 Carrier recombination processes in semiconductors.

The Fermi energy level for an intrinsic semiconductor is located near the middle of the band gap. On the other hand, the Fermi level of a p-type semiconductor is closer to the valence band while that of an n-type semiconductor is closer to the conduction band [23].

Generation and recombination are two phenomena that always occur in semiconducting devices. As mentioned earlier, generation is an electronic excitation which increases the number of free carriers available to carry charge. This process requires energy which can be provided by phonons (vibration) or photons (light). On the contrary, recombination is an electronic relaxation process that decreases the number of free carriers releasing energy. For instance, in solar cells, the process (called photogeneration) begins with light absorption and the promotion of electrons from the valence band to the conduction band, generating electrons-holes pairs. Recombination involves the annihilation of both the carriers: an electron decay from the conduction band back to the empty state associated with a hole [24].

There are three main recombination mechanisms in semiconductors (*Figure 1.7*):

- Band-to-band recombination, also known as radiative recombination, is the process in which an electron falls from the conduction band into an empty space in the valence band. During this event, a photon is emitted with the energy corresponding to the band gap.

- Trap-assisted recombination, also called *Shockley-Read-Hall* recombination, occurs when an electron falls into a "trap", which is a new energy state within the band gap caused by the presence of impurities and defects in the lattice. The electron occupying the trap energy can subsequently decay into a space in the valence band, thereby accomplishing the recombination process.
- Auger recombination is a process similar to a band-to-band transition, but now the resulting energy is given off to a third carrier instead of emitting light. After the excitation to a higher energy level, the third carrier relaxes back down to the conduction band edge [25].

In the next section, the physical phenomena that occur joining the two different types of doped semiconductors will be discussed.

1.1.1.2 p-n junction theory

A p-n junction is the classic model of a solar cell. It is formed by joining n-type and p-type semiconductor materials. After the contact, electrons move by diffusion from the n-type side to the p-type side. Similarly, holes migrate from the p-type side to the n-type side. When these carriers move to the other part of the junction, they leave behind fixed ions at the impurity sites which are unable to move. The p-side, losing holes, is charged negatively because of the net acceptor charge left behind, while the n-side conversely becomes positively charged. In the n-region close to the junction interface, free electrons are gone due to the diffusion to the p-side and recombination with holes that are diffused from the p-side. By analogy, there are no free holes in the p-side region near to the interface.

Therefore, a depletion region (or *space charge region*) free of mobile charge carriers is formed around the junction interface. This region has a net charge density due to the fixed ions in the lattice. These charged dopants produce an electric field that provides a drift current opposing the diffusion current. When the drift current is strong enough to cease further diffusion of mobile carriers, the depletion region is at the equilibrium (*Figure 1.8*). The electron (hole) diffusion current and the electron (hole) drift current exactly balance out at the equilibrium, resulting in a net flow equal to zero.

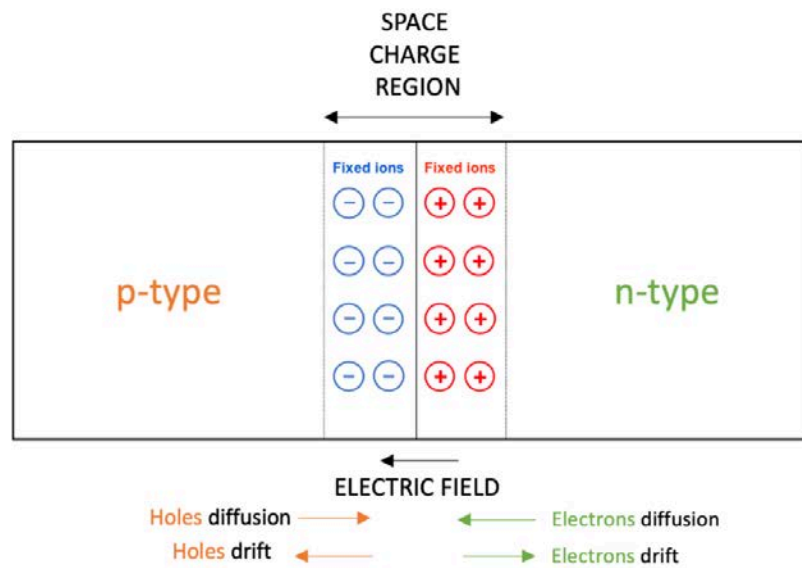


Figure 1.8 Space charge region in a p-n junction.

As already pointed out, the Fermi level of an n-type semiconductor is close to the conduction band, whereas the one of a p-type is near the valence band. This fact implies a difference in the work function (Φ) of the two different semiconductors, as illustrated in *Figure 1.9*. Φ is the minimum energy needed to free an electron from the Fermi level, and it is always smaller for the n-type materials.

After the contact and the formation of the depletion region at the equilibrium, the Fermi energy levels are the same. This fact implies a band bending in the energy diagram, and an internal potential (known as *built-in potential* V_{bi}) is caused by the electric field in the depletion region (*Figure 1.10*). The value of V_{bi} is related to the work function difference between the two zones of the junction.

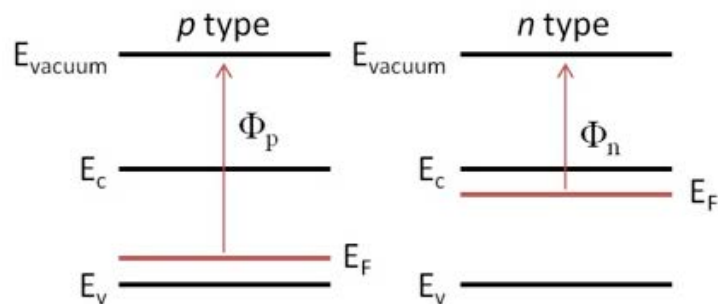


Figure 1.9 Energy band diagram for a p-type and n type semiconductors [22].

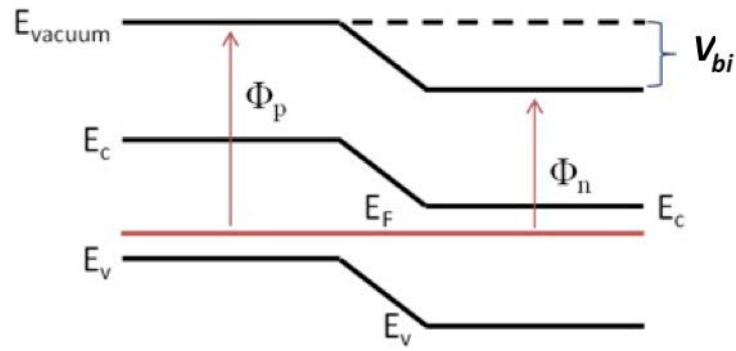


Figure 1.10 Band bending for a p-n junction in equilibrium [22].

According to [1], the *built-in* potential can be expressed as:

$$V_{bi} = \frac{kT}{q} \ln \frac{N_A N_D}{n_i^2} \quad (1.11)$$

V_{bi} acts as a potential barrier which prevents the diffusion of holes into the n-type region and electrons into the p-type region. In other words, the carriers must overcome this barrier in order to further diffuse through the junction [26].

Having dealt with the open-circuited p-n junction, it is now possible to study its behavior when under an applied voltage, either in forward or reverse bias.

In forward bias, the p-type region is connected to the positive terminal and the n-type region is connected to the negative terminal. As set out in *Figure 1.11b*, the applied voltage V_F lowers the potential barrier across the depletion region. The electrons are pushed toward the p-type region; likewise, the holes diffuse into the n-type region. Thus, the diffusion current increases considerably, and it reduces the width of the depletion zone. In summary, the p-n junction in forward bias conducts a current whose value is determined by the applied forward voltage.

In reverse bias, the n-type zone is connected to the positive terminal, whereas the p-type zone is connected to the negative terminal. In this configuration, the applied voltage V_B increases the potential barrier causing a high resistance to the diffusion carriers flow (*Figure 1.11c*). The electrons (holes) are forced to move far from the junction, leaving behind fixed charge ions which broaden the width of the depletion

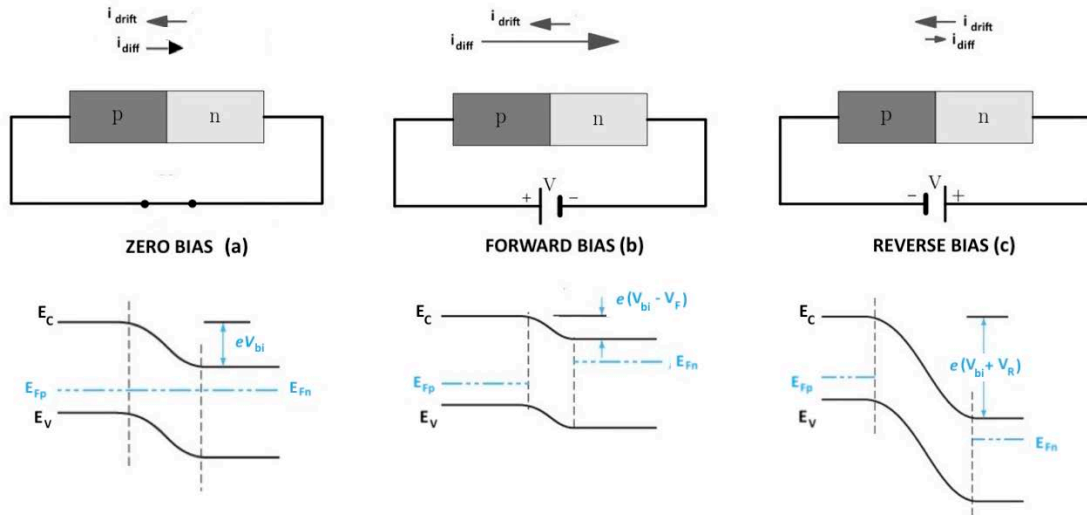


Figure 1.11 A p-n junction in: (a) Zero bias; (b) Forward bias; (c) Reverse bias.

region. Hence, just a very little drift current flows in reverse bias, and the junction behaves as an insulator. The magnitude of the electric field and the width of the depletion region increase with an increase in reverse-bias voltage, up to a certain value. Once the voltage reaches that critical level (known as *breakdown voltage*), the depletion zone breaks down and allows a large reverse current. At this point, a small change in the voltage will rapidly increase the current [27].

The p-n junction behaves like a diode when a voltage is applied. As already pointed out, a diode allows current to pass in the forward direction while blocking it in the reverse direction. The Shockley diode equation describes the electrical behavior of a p-n junction:

$$I = I_S \left(e^{\frac{qV_D}{nkT}} - 1 \right) \quad (1.12)$$

where:

- I is the diode net current;
- I_S is the saturation current;
- V_D is the applied voltage;
- q is the magnitude of the elementary charge;
- k is the Boltzmann constant;

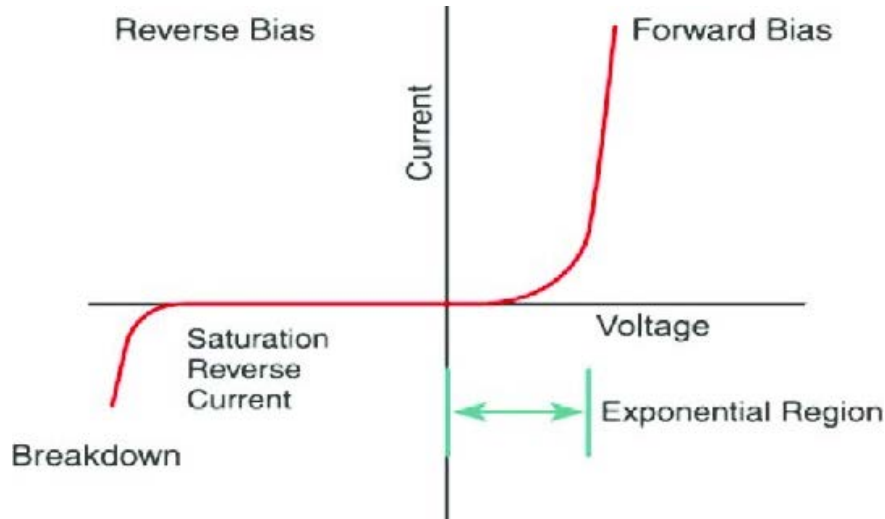


Figure 1.12 I-V curve of a p-n junction diode [21].

- T is the absolute temperature (K);
- n is the ideality factor, which is equal to 1 for an “ideal” diode.

Under reverse bias, the exponential term is close to zero, and the current is near the negative bias saturation current. On the contrary, under forward bias, the current flowing through the diode grows exponentially with the increase of temperature [28]. A current-voltage (I-V) curve of a p-n junction diode is shown in *Figure 1.12*.

1.1.1.3 Photovoltaic effect

Most solar cells are composed of large area p - n junctions. When sunlight strikes on them, they may generate current and voltage, according to the photovoltaic effect. If the photons made up the light have energy bigger than the band gap, they can promote an electron from the valence band to the conduction band that will leave behind an empty state. Hence, an electron-hole pair is generated. Because of the built-in electric field at the junction, the charges flow in the opposite direction as expected. If the p - n junction connects through an external circuit, current will be generated [29].

The Sun emits electromagnetic radiations all over the spectrum of wavelengths (frequencies) like a black body of about 5778 K [30]. Due to scattering and absorption by the atmosphere, only a fraction of the light reaches the surface of the Earth.

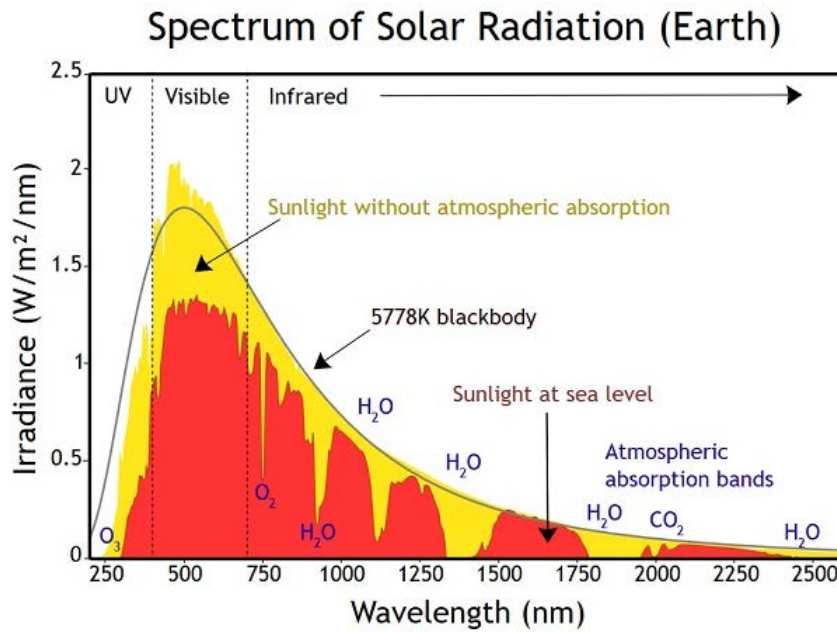


Figure 1.13. Solar spectrum out of the atmosphere and at the sea level [31].

The principal losses on the solar spectrum are due to absorbing agents, such as water vapour, ozone, and carbon dioxide (Figure 1.13). Absorptions are modeled by the air mass coefficient, AM , defined as:

$$AM = \frac{1}{\cos\theta} \quad (1.13)$$

where θ is the angle of the sun relative to the zenith. $AM0$ (i.e., the sun is above the vertical axis) is the spectra outside the atmosphere. The standard reference to compare different solar cell technologies is $AM1.5$, which represent the average spectral distribution of light at mid-latitudes [32]. It can be seen as the highest energy available for a solar cell to be converted in electrical current. Higher energy photons can be absorbed by the solar cell, but the difference between their energy and the band gap is not converted into usable electrical energy. Instead, it will be lost as heat, via phonons emissions.

The basic operations of a solar cell include [33]:

- a. The absorption of light, generating electron-hole pairs.
- b. The separation of charge carriers.
- c. The extraction of the carriers to an external circuit.

Once the charges have been generated, the solar cell must collect them in a current. As already discussed, without any driving force, electrons and holes would recombine. The action of the electric field in the depletion region of a p-n junction avoids the recombination and collects them efficiently. Metal contacts are made to both the sides of the solar cell and the electrodes connected to an external load. Hence, light generated electrons in the n-region may flow through the wire and power the load. They continue to travel through the wire, dissipating their energy until they reach the p-type semiconductor-metal contact. Here, they can recombine with a hole, as shown in *Figure 1.14*. The movement of these light-generated carriers in the external circuit and contacts produce an electric current [34].

An ideal solar cell in dark behaves like a diode, according to the Shockley equation (1.12). The rectifying behavior remains under light, but the I-V curve is shifted down into the fourth quadrant. The current in light is the superposition of the dark current and the photocurrent (I_L). Therefore, the ideal solar cell equation under illumination is:

$$I = I_S \left(e^{\frac{qV_D}{nkT}} - 1 \right) - I_L \quad (1.14)$$

Solar cells are characterized by several parameters. The open circuit voltage (V_{OC}) is the maximum value of the potential difference available from a solar cell [35]. It occurs at zero current when the terminals are isolated with an infinite load resistance [25]. At the V_{OC} , the electric field due to the photo-generated carriers cancels out the built-in electric field.

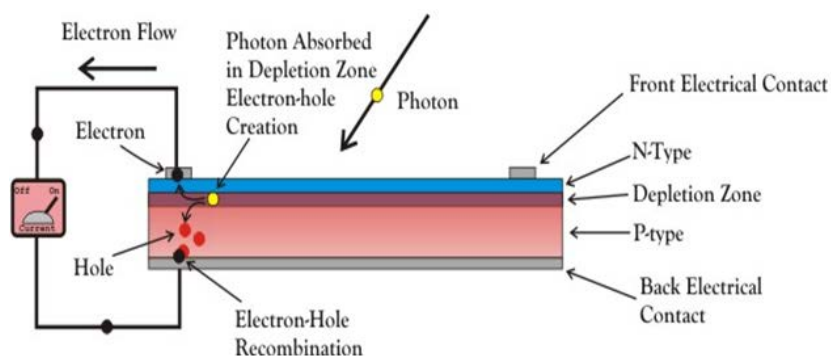


Figure 1.14. Schematic working principle of a p-n junction solar cell [34].

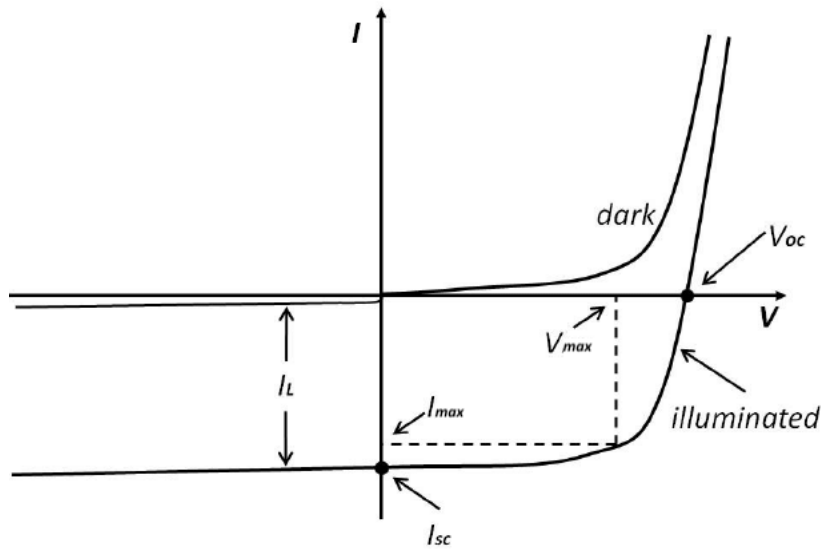


Figure 1.15. Solar cell I-V curves in dark and light [35].

The short-circuit current (I_{SC}) is the maximum current through the solar cell when the two terminals are connected together (i.e., when the device is short-circuited). In this case, there is no applied bias, and only the built-in electric field moves the carriers to the electrodes [36]. These two parameters can be easily read in Figure 1.15. The current density J is often used instead of the current itself since the current generated by a solar cell depends on its area.

Another important parameter in a solar cell is the *fill factor* (FF). It describes the “squareness” of the J-V curve, and it is defined as:

$$FF = \frac{P_{max}}{V_{oc} \cdot J_{sc}} = \frac{V_{max} \cdot J_{max}}{V_{oc} \cdot J_{sc}} \quad (1.15)$$

P_{max} is the maximum power density of the cell, which occurs at a certain voltage V_{max} corresponding to a given current density J_{max} . P_{max} determines the efficiency of the solar cell according to:

$$\eta = \frac{P_{max}}{P_s} = \frac{FF \cdot V_{oc} \cdot J_{sc}}{P_s} \quad (1.16)$$

where P_s is the incident light power. Therefore, the efficiency gives the fraction of incident power which is effectively converted into electricity. It is straightforward to

conclude that an efficient solar cell will have high J_{SC} and V_{OC} , and an FF as close as possible to 1 [37].

1.1.2 Types of solar cells

Photovoltaic technologies can be classified into three generations.

The first generation solar cells are made of silicon, either monocrystalline or polycrystalline [38]. Silicon is a semiconductor material with an energy band gap of 1.1 eV, suitable for PV applications [39]. The conversion mechanism of the first-generation solar cells is entirely based on the p-n junction theory described in the previous sections. Single crystal wafers are grown by the Czochralski process, which requires a high cost of purification. They exhibit up to 26.7% [40] conversion efficiency (laboratory scale). Polycrystalline silicon is the dominant material currently used in most solar panels. These type of cells are much less expensive than the monocrystalline, but they have lower efficiency (~20%) [41]. The first generation is still the commercially predominant PV technology, and one of the most efficient. However, the theoretical maximum conversion efficiency of 31% (known as Shockley and Queisser limit) leaves small improvements to the researches [42]. This is one of the reasons why, over the last decades, different approaches to solar cells have been investigated.

Second generation solar cells are based on thin film technologies. They are currently present on the 5-10% of the market, and they represent a solution towards a cost reduction. Instead of growing silicon crystals, the photovoltaic material is deposited as a thin film (few micrometers) on a large and low-cost substrate, such as polymer, glass or metal. This technology allows the cells to be flexible, lightweight, and suitable to be used in building components [43]. The semiconductors of the most used cells are amorphous silicon, cadmium telluride (CdTe), and copper indium gallium diselenide (CIGS). They have a direct band gap, and the behavior of the cell still relies on the p-n junction design. According to [44] and [40], the highest lab cell efficiencies of CIGS and CdTe are 22.9% and 22.1%, outperforming multi-crystalline silicon. Although they have low costs and good efficiencies, thin film solar cells have some drawbacks hindering commercialization.

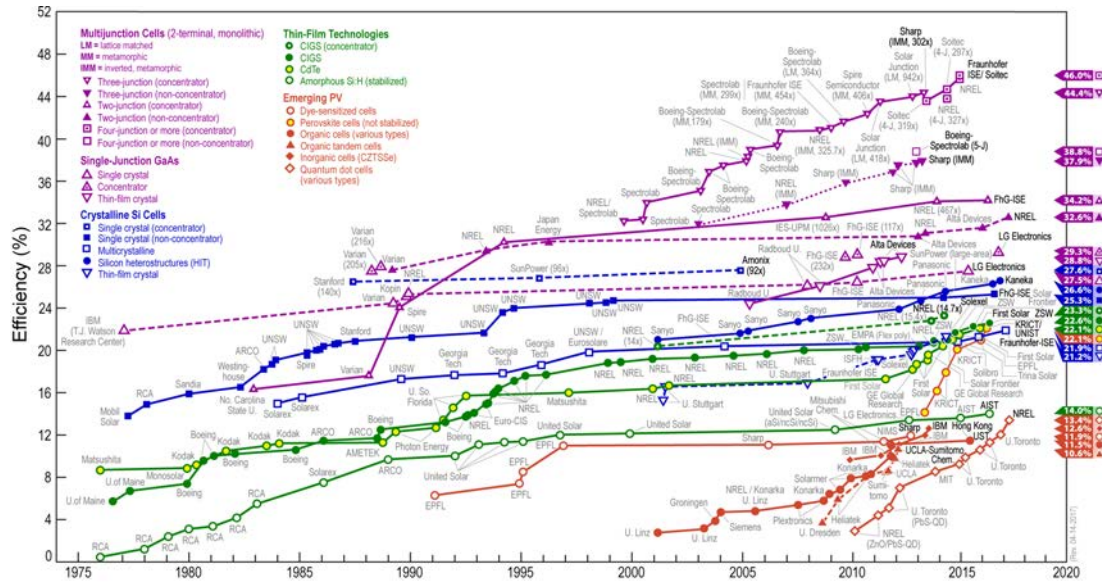


Figure 1.16 Solar cell conversion efficiencies from 1976 to 2018 [45].

Indeed, these cells are made of materials which are either highly toxic (cadmium) or rare (indium) [46]. Nonetheless, there are many ways to enhance the power conversion efficiency. This leads to the third generation of solar cells.

The term “third generation” refers to the new technologies that have arisen after the first two generations of solar cells. The aim for them was to overcome the limitations coming from the previous technologies, which are the high production costs and limited conversion efficiency. Silicon’s low theoretical efficiency is mainly due to the energy band gap, which prevents the conversion of higher-energy photons, such as those emitted by blue light waves, into electrical energy [47]. To minimize the thermalization losses, scientists started to produce multi-junction solar cells using different semiconductor materials, such as gallium arsenide and gallium phosphide. These layered solar cells allow the absorbance of a broader range of wavelengths, harvesting light from different parts of the solar spectrum. To date, a quadruple-junction solar cell developed by a French-German cooperation shows the record conversion efficiency of 46% [11] (Figure 1.16). Nevertheless, this eye-catching efficiency is gained at the cost of very high complexity and manufacturing price. Their extremely high costs have relegated their use to niche roles, notably in aerospace, where other advantages, such as weight, are more important.

Emerging third generation solar cells have the purpose of reducing the production costs. Nowadays the efficiency of these photovoltaic devices is remarkably lower compared to multi-layer solar cells. However, they have received attention in the public, and many researchers have focused their interests on them [48].

1.1.2.1 Emerging PV technologies

Next generation solar cells (NGSCs) include emerging PV technologies, such as dye-sensitized solar cell, organic solar cell, and perovskite solar cell. The record conversion efficiency is 14.1% [49], 17.3% [50], and 27.3% [51], respectively.

1.1.2.1.1 Dye-sensitized solar cells

Dye-sensitized solar cells (DSSCs) belong to the class of thin film solar cells. They are based on the photovoltaic effect, but the working principle is different compared with the p-n junctions. In a traditional cell design, silicon has both responsibilities of light harvesting and charge transfer [52]. In DSSCs, these two functions are separated. The working electrode of a DSSC consists of a porous layer of a wide band gap semiconducting material (e.g., TiO_2 nanoparticles) deposited on a glass plate which is coated with a transparent conductive oxide (TCO). The most widely used TCO are fluorine doped tin oxide (FTO) and indium tin oxide (ITO) [53]. A photosensitized dye, mostly a ruthenium complex, is anchored on TiO_2 . The counter electrode is a platinized TCO glass plate, and an iodide/triiodide solution is used as the electrolyte [54]. The schematic representation of a DSSC is reported in *Figure 1.17*.

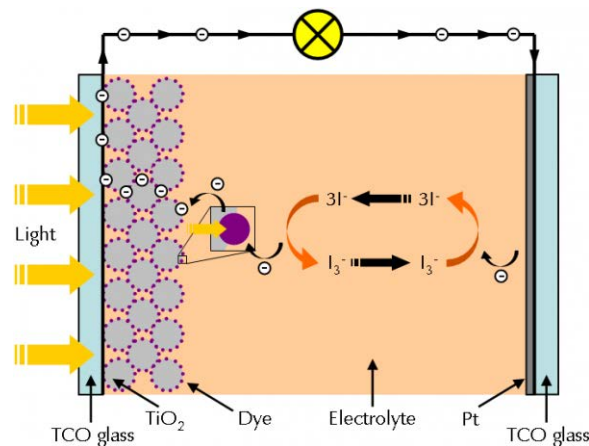


Figure 1.17 Schematic working principle of a DSSC [51].

The sunlight absorption and the photoelectrons generation are provided from the photosensitized dye. It excites electrons into the conduction band of the semiconductor oxide where the charge transport towards the TCO occurs. An external circuit transfers the collected electrons to the counter electrode and then into the electrolyte. These charges will be captured by the oxidized species (I_3^-) from the electrolyte, which gave their electrons to the photo-oxidized dye. In this way, the cycle is completed [55].

In summary, they represent an excellent alternative to the other generations, because of their low cost, good efficiency, simple manufacturing processes, and environmental friendliness [56]. The main limitation of the DSSCs is relevant to the liquid electrolyte:

- It contains volatile organic compounds, which requires a perfect sealing.
- It is not stable at varying temperatures.

1.1.2.1.2 Organic solar cells

Organic solar cells (OSCs) are devices made with organic semiconductors, which are carbon-based molecular materials [57]. They belong to the class of excitonic solar cells which are identified by the presence of an exciton. An exciton is a tightly bound electron-hole pair generated upon illumination. In the case of organic molecular systems, the stability of excitons is relatively high due to the strong electrostatic bond between the electron and the hole. This fact arises from the low dielectric constant of the organic materials which are used in this category of solar cells [58]. Excitons must be broken up into free electron-hole to generate an electric current [59]. The dissociation occurs efficiently at the interface between two dissimilar materials, which set up an electric field. An electron-donor material and an electron acceptor material are blended together forming the so-called bulk heterojunction (BHJ). This blend has a large interfacial area which promotes the generation of free carriers [60]. In organic solar cells, the valence and the conduction band are replaced by the concept of highest occupied molecular orbital (HOMO) and lowest unoccupied molecular orbital (LUMO), respectively.

The physics of the process can be divided into four fundamental steps [61].

1. Light absorption and exciton generation. Upon illumination of the active material (donor), a photon is absorbed and promotes an electron to the LUMO. The excited electron leaves behind a positive charge (hole) in the HOMO. The electrostatic interaction bonds together the charge carriers generating an exciton.
2. Exciton diffusion. The generated exciton diffuses along the donor phase to the heterojunction interface.
3. Exciton dissociation. The exciton dissociates into a free hole and electron at the interface donor-acceptor.
4. Charge carrier transport. The free charge carriers are separated by an internal electric field, which leads electrons to the cathode and holes to the anode. The application of a load to an external circuit generates the photocurrent.

Poly 3-hexylthiophene (P3HT) is the most common donor material, whereas 6,6-phenyl-C61-butyric acid methyl ester (PCBM), a fullerene derivative, is used as acceptor [62]. On the other side, metal oxides (e.g., ZnO and TiO₂) [63] and PEDOT:PSS (*Figure 1.18*) are often used for the extraction of electrons and holes, respectively [64].

The low efficiency of the BHJ devices compared to the silicon-based solar cells has limited their diffusion in the market [65]. However, they are lightweight, inexpensive, flexible, and made of non-toxic materials [60].

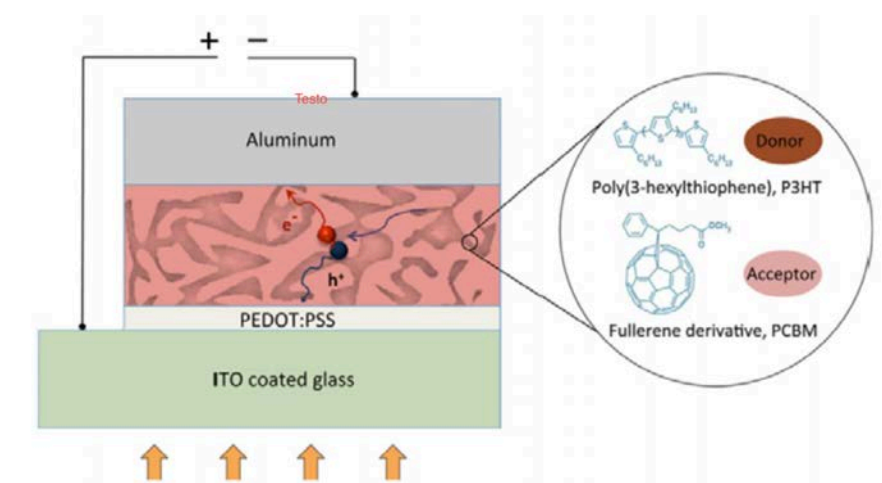


Figure 1.18 OSC device with a bulk heterojunction active layer in normal geometry [66].

All these characteristics have attracted many researchers over the last years, bringing the organic solar cells among the most investigated of the third generation.

1.1.2.1.3 Perovskite solar cells

Perovskite solar cells (PSCs) constitute a new class of PV devices which use a perovskite structure as light-harvesting photoactive layer. Perovskites are characterized by an ABX_3 structure (*Figure 1.19*), which involves particular ions for photovoltaic applications [67]. A-site is the organic part occupied by an amine derivative ion (e.g., $CH_3NH_3^+$) whereas the B-cation is the inorganic part, usually a lead ion (Pb^{2+}). The X-site can be occupied by halogen ions, such as I^- or Br^- . The resultant material is methylammonium lead iodide perovskite ($CH_3NH_3PbI_3$) [68], which is the first compound used in PSCs. $CH_3NH_3PbI_3$ has favorable optoelectronic properties, such as:

- Energy band gap of 1.55 eV [69], suitable for PV applications.
- Low exciton binding energy, which promotes the photocarriers separation.
- High charge mobilities, favoring the diffusion to the electrodes before recombining [70].
- Long charge diffusion lengths.

State-of-the-art PSCs adopt a sandwiched structure in which a hole transport layer (HTL) and an electron transport layer (ETL) enclose the perovskite.

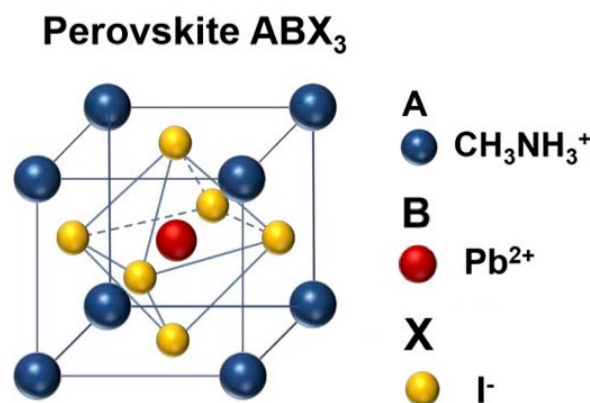


Figure 1.19 ABX_3 perovskite structure [71].

Typical HTL include polymer mixtures such as Spiro-OMeTAD [72] or PEDOT:PSS [73], while ETL are usually made of TiO_2 or SnO_2 . These two layers are placed between a transparent electrode (ITO or FTO) and a metal one (Ag, Al or Au). In a normal architecture, electrons are collected at the transparent electrode. If instead, they move towards the metal electrode, the configuration is called inverted.

In the architecture of a perovskite solar cell, a mesoporous scaffold can be added on top of the ETL [68]. It is made out of electron transport material (e.g., TiO_2) in order to improve the charge transport and the film quality. However, high-temperature processing is required to produce mesoporous layers, and the performances of the planar heterojunction counterparts are close to them.

The working principle of PSCs is similar to traditional p-n junctions, because of the formation of free charges instead of a tightly bonded exciton. Upon illumination, the photons are absorbed by the active perovskite layer, which leads to the creation of an electron-hole pair. The charges are readily separated thanks to the low exciton binding energy, and the perovskite itself can transport them [74]. Hence, photogenerated electrons diffuse to the ETL (either through perovskite or via the mesoporous scaffold), from where they are collected at the transparent electrode. Vice versa, photogenerated holes are transported to the HTL and then collected at the metal electrode.

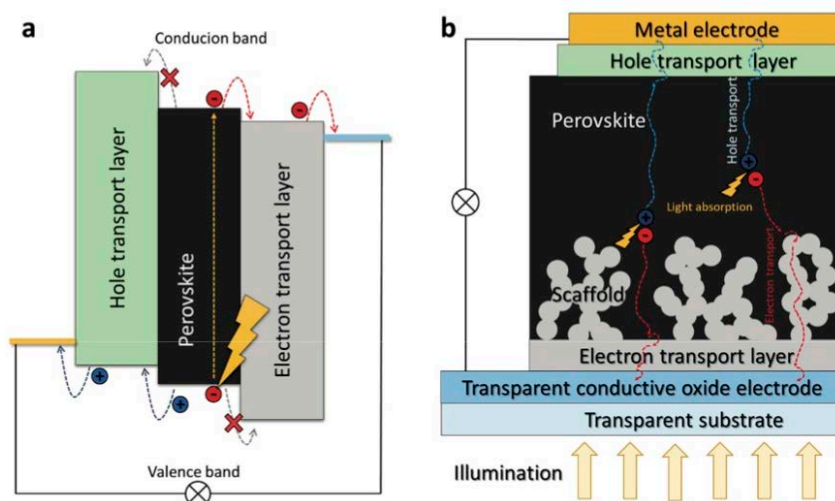


Figure 1.20 a) Schematic energy diagram of a PSC; b) Basic architecture of a normal PSC with mesoporous scaffold [75].

A schematic illustration of the charge generation and transport process is presented in *Figure 1.20*. As can be seen in *Figure 1.20a*, a good ETL material should have its valence band (or HOMO) far below that of perovskite. At the same time, its conduction band (or LUMO) should be just slightly below perovskite's conduction band. In fact, the role of the ETL is to prevent electrons from being collected at the wrong electrode. The opposite is required for HTL materials [75].

PSCs are the rising star in the field of photovoltaics. In 2018, a perovskite-silicon tandem solar cell has achieved a 27.3% conversion efficiency [51], exceeding the performances of a single-junction silicon solar cell. Progresses still need to be done in terms of stability (their power conversion efficiency deteriorates with continued exposure to sunlight) and commercialization (due to the presence of Pb, which is toxic), but the possibility to build an efficient, cheap, light-weight and flexible solar cell has strongly fascinated the photovoltaic research [76].

In addition to all these new technologies, a new field in PVs has emerged, focusing on devices that are entirely made of metal oxides semiconductors.

1.1.2.1.4 All-oxide solar cells

All-oxide solar cells (AOSCs) are promising photovoltaic devices that have attracted considerable attention during the last years. The physical concept of these new third generation solar cells is in between that of the thin film and the novel technologies. The main difference is relevant to the light-harvesting active layer, which, in this case, is a metal oxide. Hence, all-oxide solar cells are entirely based on metal oxides (MOs) semiconductors (*Figure 1.21*). The growing interest is mainly due to the use of inexpensive materials and production methods, which can lead to cheaper solar cells. MOs can overcome limits from the past generation because of their chemical stability, non-toxicity, and abundance. Consequently, all-oxide solar cells are environmentally friendly, very stable, and inexpensive [77]. Owing to the large (and tunable) band gap, many metal oxides are potentially suitable as the active material.

Nevertheless, only few of them have been investigated because of their low charge mobility and short diffusion lengths. To date, Cu₂O/ZnO heterojunctions are the most studied architectures for all-oxide solar cells.

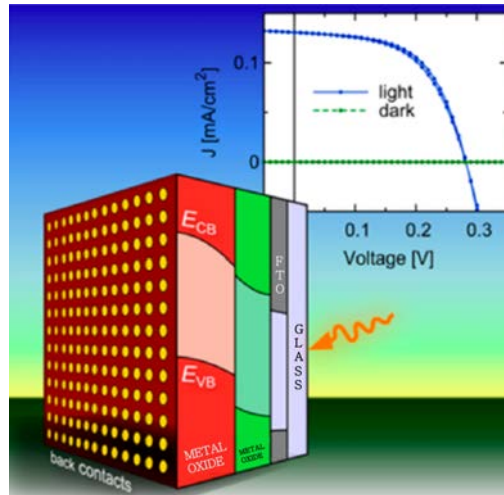


Figure 1.21 Architecture and J-V curve of an all-oxide solar cell [77].

However, the maximum conversion efficiency of 6.1% was obtained by T. Minami and alias in 2015 using a different n-type layer (Al-Ga-O) [78]. Emerging oxides, such as Co_3O_4 and Fe_2O_3 , have been used as light absorbers, but low conversion efficiencies still characterize the devices [79].

As already discussed, reducing cost and enhancing efficiency are the main tasks in the path towards the replacement of the traditional fossil energies. Nanotechnologies seem to be the way by which PVs can effectively accomplish it. In particular, nanostructured MOs are attracting increased attention in the field of the third-generation solar cells. Nanowires, nanorods and nanotubes are using instead of thin films because of their larger surface area, higher charge carrier collection ability, and tunable optoelectronics properties [80]. Many all-oxide solar cells are made of nanostructures, and, in particular, ZnO has been used in several shapes (e.g., nanowires, nanobelts, etc.). In order to better understand these novel devices, the next pages will be dedicated to the metal oxides and their general properties.

1.2 Metal-oxide semiconductors

Transition metal oxide (TMO) semiconductors constitute probably one of the most appealing classes of materials, exhibiting a remarkable variety of physical, electrical and optical properties. Most metal oxides (MOs) are chemically stable, non-toxic, and widespread in nature, making them attractive candidates for several applications [77]. They are widely used in electronic and optoelectronic devices, such as photodetectors [81], LEDs [82], and transistors [83]. Moreover, gas and chemical sensors [84] can be made of MOs. Last but not least, TMOs are suitable semiconductors in next-generation solar cells.

1.2.1 Oxides in photovoltaics

Metal oxides have been applied in solar technologies for many years. They are versatile and indispensable components of solar cells thanks to their rich electronic properties, low-cost fabrication methods, and abundance. In the photovoltaic field, they are employed in the form of thin films or nanostructures as [85]:

- I. Transparent electrodes. ITO, FTO, and AZO are the most common transparent conductive oxides (TCOs), used either in the second generation or NGSCs.
- II. Transport layers. Promising NGSCs such as OSCs and DSSCs are based on MO nanostructured electrodes coated with a thin absorber layer. ZnO and TiO₂ have been widely used as electrons-transport materials, whereas NiO has been applied as holes acceptor.

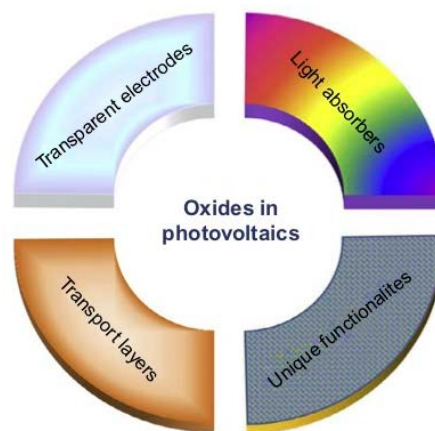


Figure 1.22 Different application of oxides in PVs [79].

- III. Mesoporous scaffolds in PSCs. An electron transport material (e.g., TiO_2) can be added in the architecture of a PSC in order to enhance the charge collection efficiency.
- IV. Active light absorbers (*Figure 1.22*). In AOSCs, metal oxides are not only part of the cell but also act as the light-harvesting active layer. To date, Cu_2O is the most investigated light absorber.

1.2.1.1 Types of oxides

Metal oxides can be either n-type semiconductors or p-type semiconductors. Most of them are “natively” n-type and found challenging to render p-type in a reliable and reproducible way. The reason for this asymmetry derives from the electronic structure of the material and the presence of intrinsic or residual defects in the crystalline lattice. The valence bands of most MOs are composed of oxygen 2p orbitals, which are far below the vacuum level. The energy of these orbitals remains very low even when accounting for the chemical bonding that occurs in the oxide. The generation of holes in the valence band is, therefore, an improbable event, mainly because it is difficult to find suitable acceptor dopants characterized by a very low-energy unoccupied orbitals. On the contrary, their higher energy value of the conduction-band minimum promotes the generation of electrons, explaining the typical n-type conductivity [86].

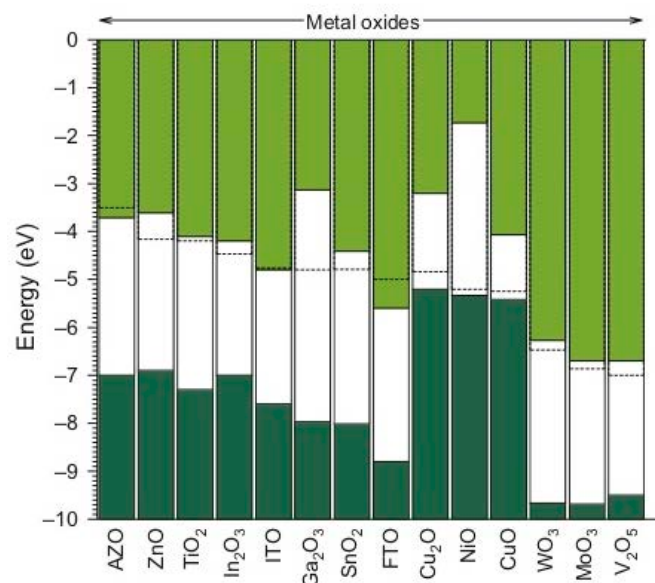


Figure 1.23 Energy band diagram of several metal oxides. The zero of energy corresponds to the vacuum level [85].

These type of metal oxides have a wide band gap, usually greater than 3.2 eV, with low absorption (i.e., high transparency) of visible light [87]. ZnO, TiO₂, and TCOs belong to this category.

Conversely, Cu₂O shows naturally p-type conduction, ascribed to copper vacancies in the lattice. As can be noticed in *Figure 1.23*, Cu₂O has the valence band that lies higher on the energy scale, allowing an easier generation of holes compared to the p-type semiconductors. Since Cu₂O has a high absorption coefficient and a direct band gap of 2 eV, it can be used as the light absorber in nanostructured and thin film solar cells, replacing toxic and less abundant materials, such as indium and cadmium.

1.2.1.1.1 Zinc oxide

Zinc oxide (ZnO) is an n-type semiconducting material with a wide energy band gap of 3.37 eV [88]. It has been employed in several applications, such as photodetectors, gas sensor, solar cells, and thin film transistors [89]. It exhibits a direct band gap and a high exciton binding energy of 60 eV [90], which ensure strong room-temperature luminescence and efficient excitonic emission. ZnO belongs to the II-VI semiconductor group, and it can crystallize in three different forms: hexagonal wurtzite, cubic rocksalt, and cubic zincblende (*Figure 1.24*). The first structure is the most stable and common at ambient conditions, while the others require special synthesis conditions. The wurtzite lattice parameters are $a = 3.25 \text{ \AA}$ and $c = 5.2 \text{ \AA}$, which lead to a hexagonal structure. Due to the absence of a symmetry center, ZnO wurtzite crystal reveals a piezoelectric behavior [91]. Anisotropic structures (e.g., nanowires and nanorods) can be synthesized thanks to the asymmetry in the lattice.

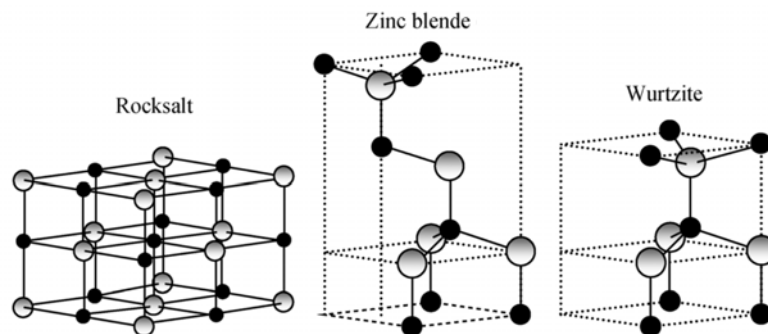


Figure 1.24 Schematic of ZnO crystal structures [92].

ZnO is a native n-type material. This fact was initially attributed to intrinsic defects, such as oxygen vacancies [93] or zinc interstitials. However, recent studies have ascribed the n-type behavior of ZnO to residual impurities (e.g., hydrogen molecules) coming from the growth techniques. The p-type doping of this oxide is still a big issue, although many efforts are being developed to achieve reliability and reproducibility [86].

In NGSCs, such as OSCs and PSCs, ZnO is mainly employed as ETL [94]. In DSSCs, ZnO and TiO₂ can be chosen as the cathode material [88]. The two oxides are characterized by similar band gap but ZnO has higher electron mobility (~120 cm²/Vs) and longer electron lifetimes [95]. This leads to lower charge recombination, which is a crucial aspect for the conversion efficiency of the solar cell. Moreover, it can be obtained in different shapes (e.g., thin film, nanowires, nanobelts, etc.) through simple and low-cost synthesis techniques. Lastly, coupled with a light-absorber oxide, ZnO is used as window material in AOSCs.

1.2.1.1.2 Titanium oxide

Titanium dioxide (TiO₂), also known as titania, is a semiconductor oxide which exhibits a wide band gap energy and catalytic properties [96]. Like ZnO, it has a natural n-type behavior deriving from oxygen vacancies or residual defects. There are several crystallographic structures found in nature, but the most important are rutile (tetragonal), anatase (tetragonal), and brookite (orthorhombic) [86]. Although rutile is the most thermodynamically stable phase, the anatase structure is more suitable for solar cell applications. This is due to its higher band gap (3.2 eV) with respect to that for the rutile structure (3 eV) and a lower rate of electron-hole pairs recombination [97].

The application of TiO₂ in solar cells has increased together with the growth of research activities in the field of nanotechnologies. TiO₂ in the form of nanotubes, nanowires, and nanosheet have been widely applied in PV devices, offering a larger surface area and higher electron mobility [98]. The large band gap allows the sunlight conversion only in the ultraviolet region, which means that TiO₂ is transparent in the visible part of the solar spectrum. Thus, it can be used as ETL in NGSCs: it facilitates the injection and transport of electrons, simultaneously avoiding the collection of holes

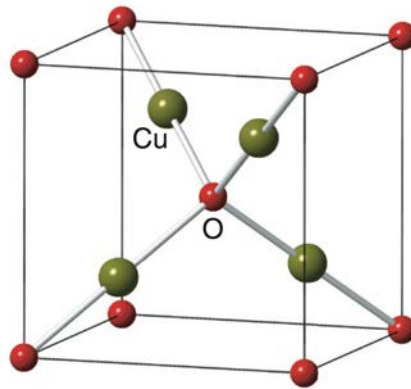


Figure 1.25 Crystal structure of Cu_2O [99].

at the cathode [100]. In AOSCs, it can be merged with a lower band gap light absorber (e.g., Cu_2O or Co_3O_4) to improve the conversion efficiency of the cell.

1.2.1.1.3 Copper oxide

Copper (I) Oxide, or Cu_2O , is one of the most used metal oxides in novel solar cells. It is an abundant and non-toxic semiconductor with a direct band gap of 2.2 eV [79]. Its structure is cubic, with O and Cu atoms arranged in a body-centered cubic (bcc) and face-centered cubic (fcc) sublattice, respectively *Figure 1.25*. Cu_2O has a spontaneous p-type conductivity induced by a large concentration of Cu vacancies, and so far it was not possible to obtain efficient n-type doped Cu_2O [101]. The Shockley-Queisser efficiency limit of Cu_2O is about 20% [102], thanks to its relatively high charge mobility at ambient condition and its sufficiently long minority carrier diffusion length [103]. Nonetheless, this promising theoretical limit has never been reached in Cu_2O -based solar cells. This is largely because of manufacturing issues, which can lead to Schottky junctions in the presence of metallic Cu or CuO. Combined with lattice defects, they can cause non-radiative recombination as well as degradation of conductivity and charge mobility [104]. Despite all these limitations, Cu_2O is still the most investigated as the active layer for AOSCs.

In the 1970s and early 1980s, Cu_2O -based solar cells were mostly Schottky-type junctions $\text{Cu}_2\text{O}/\text{Cu}$. The highest report efficiency for this structure is 1.8%, with a $V_{OC} = 0.525 \text{ V}$ and $J_{SC} = 7.35 \text{ mA/cm}^2$ [105]. The impossibility to achieve higher conversion efficiencies has moved the interest of researchers on new architectures, such as metal-insulator-semiconductor (MIS) structures and p-n heterojunctions. Their PV

performances are better than the Schottky-type junctions, but still far from the theoretical limit. To date, the average conversion efficiency for p-n heterojunctions is 3-4%, and new nanostructured based solar cells have been shown remarkable advantages over traditional thin film devices. This is the reason why nanorods and nanowires of ZnO and TiO₂ have been employed as the windows layer in the Cu₂O based all-oxide solar cells of this thesis work.

1.2.1.1.4 Cobalt oxide

Cobalt oxide (Co₃O₄) has recently captured a lot of interest among researchers as a potential alternative to Cu₂O in AOSCs. Co₃O₄ is one of the few p-type semiconductors having two direct energy gap of 1.48 and 2.19 eV [106]. It has been demonstrated that the power conversion efficiency increases if the band gap of the absorbing layer material is in between 1.1 and 1.6 eV [107]. Co₃O₄ has a cubic spinel crystal structure which contains Co (II) ions in the tetrahedral sites and Co (III) ions in the octahedral sites. It shows remarkable stability during oxygen reduction as well as noticeable electro- and photochemical properties [108]. Therefore, Co₃O₄ is a promising material for fuel cells [109], sensors [110], catalysts [111], and optoelectronic devices. Co₃O₄ is synthesized by numerous techniques: spray pyrolysis [112], sputtering [113], electrodeposition [114], CVD [114], and ALD. Despite its promising applications, the amount of theoretical and experimental information on the electronic structure of Co₃O₄ is limited. In particular, the origin and the size of the optical band gaps are still widely investigated by the researchers.

Co₃O₄ has been studied as the hole transport layer in carbon-based PSCs [115]. Being a p-type semiconductor, it can enhance the performance of the cell by avoiding the charge recombination. Moreover, it can be employed as the absorber layer in AOSCs coupled with window layers like ZnO and TiO₂. This architecture and the one relative to Cu₂O will be discussed in the next paragraph.

1.2.1.2 All-oxide Heterojunctions

As already pointed out, Cu₂O is the most used metal oxide in heterojunction architectures. Combined with n-type semiconductors, such as ZnO and TiO₂, Cu₂O has been widely investigated in the new generation of solar cells.

The most popular Cu₂O-based solar cells employ ZnO as the window material.

Table 1.1 All-oxide solar cells and their photovoltaic performance.

Heterojunction structure	V_{oc} (V)	J_{sc} (mA/cm ²)	η (%)	Ref
AZO/ZnO/Cu ₂ O/Au	0.69	10.09	3.83	[116]
AZO/Zn _{0.91} Mg _{0.09} O/Cu ₂ O/Au	0.80	9.00	4.31	[104]
MgF ₂ /AZO/Al _{0.025} Ga _{0.975} O/Cu ₂ O:Na/Au	0.84	10.95	6.10	[78]
MgF ₂ /AZO/Zn _{0.38} Ge _{0.62} O/Cu ₂ O:Na/Au	1.10	11.00	8.10	[117]
FTO/TiO ₂ /Cu ₂ O/Au	0.36	8.9	1.25	[118]
FTO/TiO ₂ /Co ₃ O ₄ /Au	0.43	0.20	0.022	[107]

The valence band maximum (VBM) of Cu₂O is higher than the VBM of ZnO, and the conduction band minimum (CBM) of ZnO is a little lower than the CBM of Cu₂O [119]. This favorable energy configuration promotes the separation of photogenerated carriers. Cu₂O/ZnO heterojunctions have been synthesized using several fabrication techniques (e.g., pulsed laser deposition, atomic layer deposition, and sputtering), but the power conversion efficiency (PCE) is still very low compared to the silicon-based solar cells. It has been noticed that the PCE increases using ITO or AZO as n-type doping layer. High conversion efficiencies of 3.83% [116] and 4.08% [120] were obtained in an AZO/non-doped ZnO/Cu₂O heterojunction solar cells.

In 2016, Minami et al. demonstrated the highest PCE (over 8%) employing multicomponent oxide thin films as the buffer layer [117]. In *Table 1.1*, the structure of the two most efficient cells, as well as their photovoltaic properties, have been reported.

Besides ZnO, TiO₂ has been used to form a bilayer heterojunction with Cu₂O. Sahena et al. (2013) reported a PCE of 1.05% in a Cu₂O/TiO₂ solar cell [121]. Moreover, TiO₂ nanowires covered by an electrodeposited Cu₂O thin film were synthesized by a hydrothermal method. Luo et al. found a PCE of 1.25% in this nanostructured device [118].

Co_3O_4 can theoretically replace Cu_2O in all-oxide heterojunctions. In 2014, Kupfer et al. have produced an FTO/ TiO_2 / Co_3O_4 /Au solar cell [107]. The TiO_2 window layer and the Co_3O_4 solar absorber were prepared by spray pyrolysis and pulsed laser deposition (PLD), respectively. They noticed that the Co_3O_4 deposition temperature affected the crystallinity of the compound. The maximum PCE (0.022%) was achieved for the highest deposition temperature (600 °C) with a V_{OC} of 430 mV and J_{SC} of 200 $\mu\text{A}/\text{cm}$.

Lastly, it is possible to combine ZnO and Co_3O_4 resulting in a p-n heterojunction. Since they share the same crystalline structure and suitable electronic band structures, a good junction can be formed at the interface. Nanostructures play a key role in these two oxide semiconductors. In 2014, Wei et al. investigated three kinds of Co_3O_4 /ZnO nanostructures [122], obtaining a significant photovoltaic effect for ZnO nanowires and Co_3O_4 nanoparticles.

1.2.1.3 Nanostructured heterojunction cells

To date, the most efficient all-oxide solar cells are based on thin film structures. However, ZnO in the form of nanorods (NRs), nanowires (NWs), nanotubes (NTs), nanofibrous network (NF) or nanopillars (NPs) has been widely investigated in nanostructured all-oxide Cu_2O solar cells. For what concerns the n-type oxide, ZnO nanowires (NWs) are predominantly grown through hydrothermal methods. Then, Cu_2O , which is deposited by sputtering, electrodeposition, or ALD, fills the voids of the nanostructured electrode. The folded heterojunction exhibits a twofold benefit:

1. The p-n junction area is amplified, which should enhance the photogenerated current.
2. Light absorption and exciton extraction are decoupled, reconciling thick absorbing layer with short exciton diffusion [85].

Furthermore, the NW arrays, providing a direct path to the substrate, show improved charge carrier mobility and collection [123]. Nonetheless, nanostructured solar cells have not reached so far outstanding performance. The best result was reported by Chen et al. [124] on glass/AZO/ZnO-NRs/ Cu_2O /Au solar cells.

Table 1.2 Nanostructured Cu₂O/ZnO solar cells and their photovoltaic performance.

Heterojunction structure	V_{OC} (V)	J_{SC} (mA/cm ²)	η (%)	Ref
glass/AZO/ZnO-NR/Cu ₂ O/Au	0.42	9.89	1.52	[124]
glass/ITO/ZnO-NP/Cu ₂ O/Au	0.29	8.20	0.88	[125]
glass/ITO/ZnO-NR/Cu ₂ O/Au	0.36	7.80	0.86	[126]
glass/ITO/ZnO-NT/Cu ₂ O/Au	0.66	2.42	0.80	[127]
glass/ITO/ZnO-NF/Cu ₂ O/Au	0.43	4.28	0.77	[128]
glass/ITO/ZnO-NW/Cu ₂ O/Au	0.28	4.40	0.47	[129]

ZnO was electrodeposited, while Cu₂O thin film was obtained by chemical bath deposition (CBT). The PCE was 1.52%, with $V_{OC} = 0.42$ V and $J_{SC} = 9.89$ mA/cm². In place of NWs, Cui et al. [125] have electrodeposited ZnO nanopillars on a glass/FTO substrate. The efficiency of the Cu₂O/ZnO solar cell was 0.88%, higher than the one (0.55%) of the planar counterpart. In *Table 1.2*, the performance of the most efficient nanostructured Cu₂O/ZnO heterojunctions has been reported.

In 2016, Abd-Ellah et al. [127] obtained the largest value of V_{OC} (0.66 V) on an annealed device. The heat treatment has played a crucial role by decreasing the defect density, enhancing the crystallinity of Cu₂O, and increasing the carrier concentration. Apart from this exception, the V_{OC} of the nanostructured heterojunctions is smaller than in planar solar cells.

Concerning titanium oxide, TiO₂ NRs are produced by hydrothermal methods or spray pyrolysis. In the previous chapter, the best Cu₂O/TiO₂ solar cell has been discussed [118]. In 2015, Pavan et al. [130] used spray pyrolysis to produce both the oxides. They measured $V_{OC} = 0.35$ V and $J_{SC} = 0.4$ mA/cm², resulting in $\eta = 0.035$ %. Although the lack of eye-catching results, the advantages over traditional bilayer have been driving the researchers to find new structures and oxides combinations.

1.3 Atomic force microscopy (AFM)

Nanotechnology and surface science have attracted many fields of research over the last decades. The trend towards the nanoscale is strictly connected to the material properties, which are ultimately based on the atomic structure. Detailed atomic-scale understanding of electrical and morphological properties has become an essential part of the characterization of materials. This growing interest has led to a rapid development of nanoscale-based techniques, all belonging to the scanning probe microscopy (SPM) family. Among these techniques are conductive atomic force microscopy (C-AFM) and photoconductive atomic force microscopy (PC-AFM), which are based on a conductive probe. Before describing advanced-AFM characterizations, a short paragraph will be dedicated to the working principle of the base technique.

1.3.1 General principle

Scanning Probe Microscopy (SPM) is a unique tool for characterizing materials at the nanoscale. In SPM, a small tip is moved upon a surface in order to detect the local properties. Among all the surface science analysis tools, Scanning Tunnelling Microscopy (STM) and Atomic Force Microscopy (AFM) are the oldest and most applied techniques in both research and industry. AFM has proved to overcome some issues concerning STM, which is not feasible for insulating surfaces. Instead of the tunneling current, which is measured in STM, the AFM detects the force between the surface of the sample and the tip [131].

The AFM provides a nanoscale profile of the surface, by allowing a nanosized probe to come in contact to the sample that is being investigated. The tip, which is fabricated by semiconductor processing techniques, is supported at the end of a flexible cantilever. The sample is then scanned underneath the tip, while a piezoelectric element maintains a constant deflection of the cantilever. A laser beam detects the bending of the cantilever by reflecting towards a position-sensitive photodetector (*Figure 1.26*). Thus, these deflections are sent to a controller and processed using imaging software, resulting in a topographical image of the sample [132].

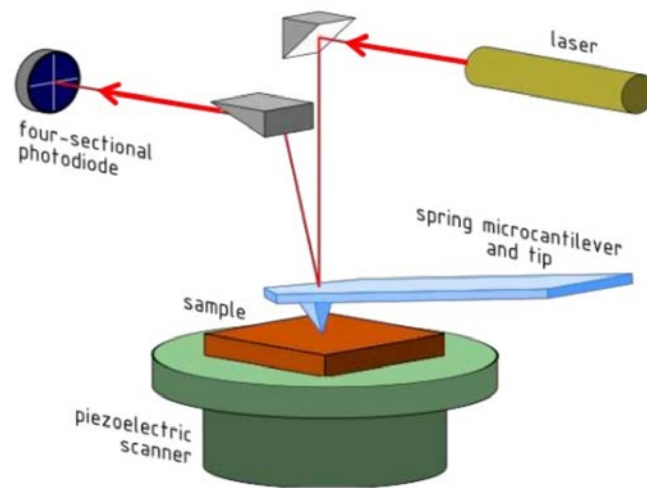


Figure 1.26 Working principle of AFM [133].

The Hooke's Law describes the force (F) between the sample and the tip:

$$F = -k \Delta x \quad (1.17)$$

where k is the stiffness (spring constant), and Δx is the deflection of the cantilever. Among the weak forces, van der Waals interactions are predominant in AFM. These forces can be either repulsive or attractive, as shown in *Figure 1.27*. When the distance between the sample and the probe is less than few angstroms, the tip experiences repulsive van der Waals force. On the contrary, when the cantilever is held several angstroms away from the surface, the interatomic force is attractive [134].

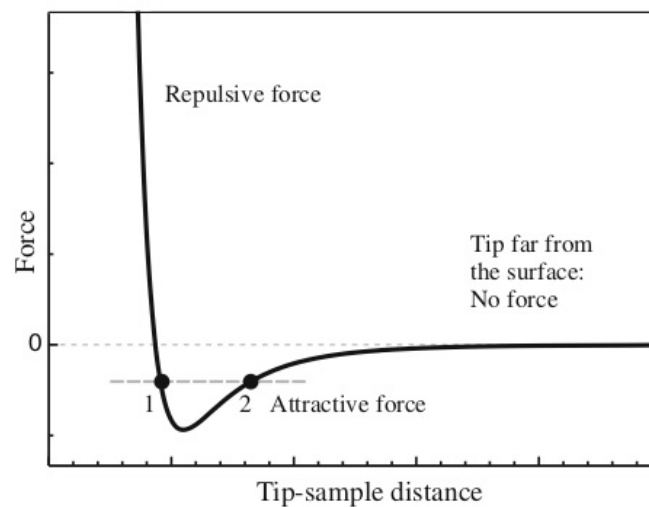


Figure 1.27 Force behavior as function of sample-tip distance [132].

The different regions of the curve describe the three AFM scanning modes:

- Contact mode, which operates in the repulsive region and detects the deflection.
- Non-contact mode, which works in the attractive part and detects the amplitude of the oscillation of the tip.
- Tapping mode, which oscillates between the two.

The tapping mode overcomes some drawbacks concerning the other two modalities. Compared with the contact mode, it ensures lower lateral forces as well as less sample and tip damages. With respect to the non-contact mode, it leads to higher lateral resolution. In general, AFM is widely used for the characterization of materials since it does not require minimal sample preparation, providing a three-dimensional surface profile even in ambient conditions [135].

1.3.2 AFM characterizations

In this work, AFM has been used in contact mode, with a conductive probe, to measure the local conductivity and photoconductivity of all-oxide optoelectronic devices. Moreover, this technique has been coupled with an impedance spectroscopy set-up, in the so-called impedance spectroscopy-AFM (IS-AFM).

1.3.2.1 Conductive AFM

The conductive atomic force microscopy (C-AFM) was reported for the first time in 1993 by Murrel et al. [136]. C-AFM is an advanced mode of the AFM that simultaneously records the surface topography and the current distribution at the tip-sample contact point. This powerful current sensing technique gives information about the local conductivity down to the nanoscale. For instance, by scanning a large area of the surface, it is possible to characterize NW forests and, at the same time, to obtain a single wire resolution. However, finding a direct link between the local electrical properties and the morphology is still a big issue for nanostructured samples [137].

The C-AFM operates in contact mode regime using a conductive tip. Besides the conventional AFM set-up, a voltage source and a preamplifier are required in C-AFM (*Figure 1.28*).

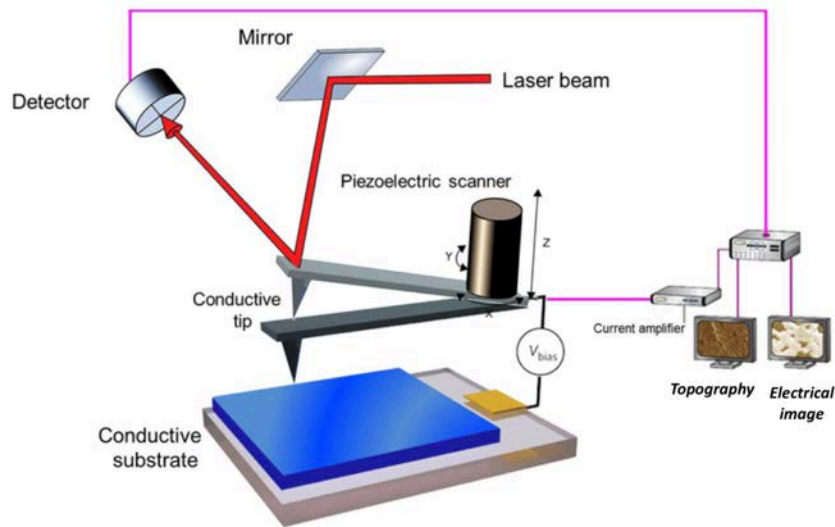


Figure 1.28 Schematic drawing of a C-AFM [138].

An electric potential difference is applied between the sample and the nanoprobe to get the local electrical information [139]. The external bias voltage, which can scan between -10 V and +10 V, is applied to the sample.

The tip can either scanning the surface under a constant voltage or be kept at a specific location while changing the voltage. C-AFM usually operates in air, adopting a Faraday cage that protects the sample from external noise and electrical interference [140].

STM and C-AFM have a striking resemblance in the instrument set-up. However, the working principle of the two is different. In C-AFM, the current-to-voltage preamplifier and the optical system (laser-photodiode) independently detect the current and the topography. This is a substantial advantage over STM, where the two detection systems are not separated, and the topography is based on the current that flows between the sample and the tip [141].

1.3.2.1.1 Effect of the nanoprobe

The choice of the tip is one of the most important operations in a C-AFM experiment. Conventionally, the conductive probes are made of silicon, which is covered by a conductive, wear resistive coating. There are several types of thin film that can be used for this purpose. Among them are heavily doped diamond, titanium nitride (TiN),

platinum-iridium (PtIr), and gold (Au). They guarantee high stability of the tip enhancing, at the same time, the electrical properties. To date, diamond coated tips, either heavily nitrogen doped (n-type) or boron doped (p-type), have shown the best results. Their behavior is close to that of metallic varnished tips, with a film resistivity of about $0.5 - 1 \Omega \cdot cm$ [141]. An important parameter is the thickness of the coatings, which affects the radius of the tip apex. It must be thin enough to ensure high lateral resolution while keeping the tip sharpness. On the other hand, the friction forces and the large current densities that occur in a C-AFM experiment require high thicknesses. Thus, the choice of the appropriate probe arises from a compromise between its lifetime and desired resolution.

The curvature radius and the work function of the coating are other two fundamental characteristics. Diamond coated conductive probes (e.g., DCP20) have a curvature radius of about 100 nm, which is higher than the one with a metal coating. Despite a lower spatial resolution on rough surfaces, they guarantee longer stability and more reliable results (soft layer wears out faster, the tip is no more conductive). Furthermore, it has been demonstrated by Rezeq et al. [142] that the size of a metal coated nano-probe affects the I-V curves. In particular, they pointed out a transition from a reversed rectifying behavior, when the tip radius is small, to a normal Schottky junction at large contact. This tip effect on the nano-Schottky diode behavior is shown in *Figure 1.29*, and it will be helpful to justify some experimental results.

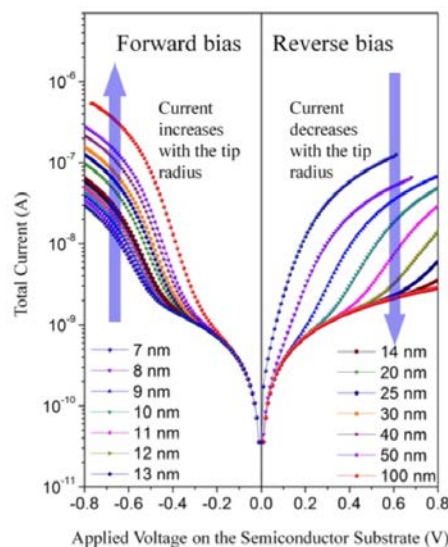


Figure 1.29 Effect of the tip radius on semi-log I-V curves [142].

The work function of the metal coating influences the type of electrical contact between tip and sample. In this work, the samples are semiconducting oxides having a lower work function compared to the diamond coated nano-probe ($\phi = 5.57 \text{ eV}$). Due to this fact, a Schottky junction is formed, which generates an effective potential barrier. As previously explained, the barrier is reduced in forward bias, allowing a current which increases exponentially with the voltage. On the other hand, when a reverse bias is applied, the barrier for the electron flow becomes higher, and the current remains constant and small [143].

1.3.2.1.2 Photoconductive AFM

Photoconductive AFM (PC-AFM) is the result of an implementation of the C-AFM set-up, initially employed for analyzing photoelectric properties of organic thin films. An illumination system is usually mounted on the back side of the sample while the sample is biased. The light reaches the sample passing through an FTO/ITO layer, which becomes the cathode in the electric circuit originated with the metal tip (anode). The light interaction with the surface of the sample can produce a photocurrent, providing electrical information down to the nanoscale.

The PC-AFM is mainly used on the surface of NGSCs, outlining the mapping of the photocurrent and photoactive regions, determining the J-V curves, and providing the power conversion efficiency of the cell. The technique has been successfully employed to map the local photocurrent in OSCs [144] and ZnO based solar cells [145]. The focus of solar cells towards nanostructures will lead to a growth of these local characterization methods, which can accurately measure nanoscale properties. The main drawback of this technique concerns the light source. As a matter of fact, when a “strong” LED shines the samples, the tip is no longer stable (the initial deflection can vary in the range $\pm 0.5 \text{ nA}$).

1.3.2.2 Impedance Spectroscopy combined with AFM (IS-AFM)

Impedance spectroscopy (IS) is a useful technique for the characterization of frequency-dependent electron transfer processes, which are analyzed through equivalent electrical circuits. Impedance (Z) is defined as a function of the frequency [146]

$$Z(\omega) = \frac{V_{ac}}{I_{ac}} \quad (1.18)$$

where:

- $V_{ac} = V_0 \sin(i\omega t)$, is the ac bias applied.
- $I_{ac} = i_0 \sin(i\omega t + \theta)$, is the sinusoidal current response.

The impedance is represented as a complex number,

$$Z(\omega) = Z_r + i \cdot Z_i = |Z| \exp(i\theta) \quad (1.19)$$

where:

- Z_r is the real part of Z .
- Z_i is the imaginary part of Z .
- $|Z|$ and θ are the modulus and the phase of Z , respectively.

Impedance Spectroscopy is widely used in the PV field to obtain information about minority carrier lifetimes, acceptor impurity densities, and electrical resistance in the device [147]. Depending on the type of solar cell, which is mainly a silicon-based, DSC or OSC, different equivalent electrical circuits can fit the experimental data.

Nowadays, researches have focused their interest in submicron phenomena, which require reliable characterization techniques. Local electrical properties can be obtained by coupling IS and AFM (IS-AFM), known in the literature as scanning impedance microscopy (SIM) or nano-impedance microscopy (NIM) [148]. The set-up (*Figure 1.30*) includes a standard C-AFM with a commercial impedance analyzer (potentiostat).

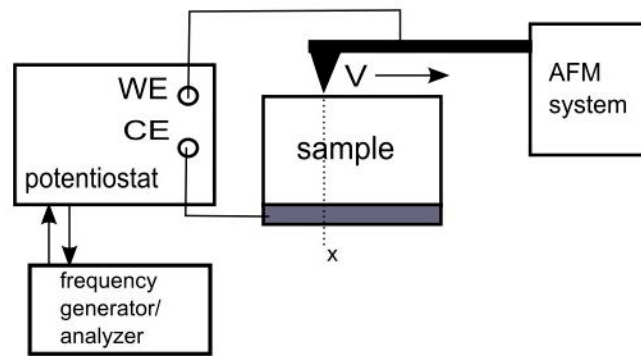


Figure 1.30 Schematic set-up of IS-AFM [149].

Local electrical parameters concerning the tip-sample nano-junction, such as stray capacitance and inductance, can be determined. The IS data can be simulated by equivalent circuits, like the ones reported in *Figure 1.31* and *Figure 1.32*. *Figure 1.31* points out a circuit with a series resistance and a resistance-capacitance (R-S) pair, which results in a single semi-circle in the graph. While this fitting works with single junctions, an extra RC pair is necessary to simulate the data that show an evident deviation from a single semi-circle. The equivalent circuit in *Figure 1.32* takes into account the double junctions that occurs in AOSCs: n-type oxide/FTO and p-type oxide/n-type oxide.

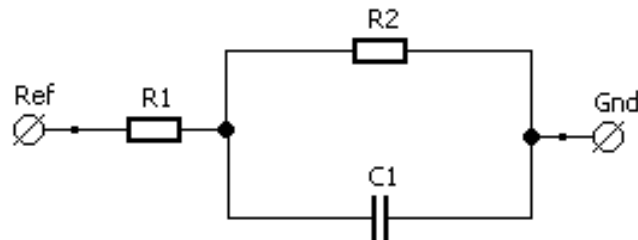


Figure 1.31 Equivalent circuit model for IS-data from single oxides.

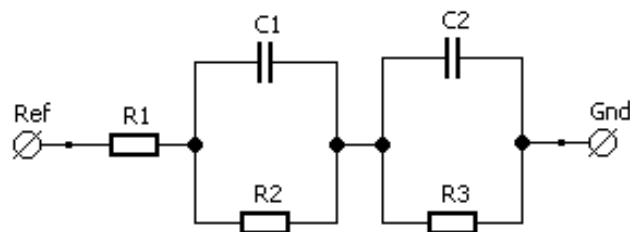


Figure 1.32 Equivalent circuit model for IS-data from AOSCs.

1.4 Objectives of the thesis

The main goal of this thesis is the electrical characterization of nanostructured optoelectronic devices, either in a macro or nanoscale. Four different types of oxides have been used in this work. As n-type material, ZnO and TiO₂ NWs have been grown by hydrothermal method on an FTO substrate. Different techniques, such as chemical vapor deposition (CVD), atomic layer deposition (ALD) and reactive magnetron sputtering, have been applied for the thin film deposition of p-type oxides (Cu₂O and TiO₂).

Cu₂O/ZnO, Co₃O₄/ZnO, and Co₃O₄/TiO₂ heterojunctions have been investigated by means of structural, morphological, optical and electrical techniques. The most important parameters for photodetectors or solar cells are the photoresponse and the power conversion efficiency (PCE). For this purpose, C-AFM and macroscopic J-V measurements revealed exciting results. In particular, C-AFM in dark and light allowed to obtain the local photo-electrical properties of the investigated oxide materials at the nanoscale.

1-dimensional (1D) nanostructures, as well as thin films, have been used as the n-type layer. A comparison between the two architectures is discussed in the results chapter, with the intent to confirm the advantages of NWs based solar cells over their thin film counterparts. In fact, according to [150], they enable much faster charge transport and a higher probability of photon absorption because of the light confinement inside the nano-array.

2 MATERIALS AND METHODS

In this section, the synthesis and the characterization of the p-n heterojunctions will be treated. It is important to specify that the primary goal of this thesis concerns the nano and macro electrical characterization of the devices, to greater importance than their synthesis. However, a brief discussion about the preparation of the different samples is reported, starting from the general technique principles.

2.1 Synthesis

2.1.1 Synthesis techniques

Many techniques have been used for the synthesis of the p-n heterojunctions. All the samples are grown on top of FTO/glass or ITO/glass, which are widely used in photovoltaics because of their optical transparency and high conductivity.

2.1.1.1 Hydrothermal growth

ZnO NWs and TiO₂ NWs are grown on top of FTO/glass substrate by hydrothermal method. The basic principle of the technique involves the crystallization of insoluble materials using high temperatures and pressures. The crystal growth is performed in an autoclave, where precursors are added in an aqueous solution. A specified temperature remains constant during the process ensuring the good quality of the crystals. According to [151], different molar concentrations of precursors solution lead to different nanostructures. Specifically, ZnO NWs require a more diluted aqueous solution compared to ZnO NRs. The specific precursors and molar concentrations are reported in *section 2.1.2*.

Nanostructured metal oxides are not directly synthesized on the FTO surface. Indeed, to produce vertical well-aligned NWs, a seed layer is required. It is usually deposited by spin coating, providing nucleation sites for the growth of the nanostructures.

2.1.1.2 Physical Vapor Deposition (PVD)

Physical Vapor Deposition (PVD) describes a variety of techniques used to deposit thin layers ($nm \div \mu m$) of material. All the vacuum deposition methods consist of three fundamental steps [152]:

1. Vaporization of the target material from a solid or liquid source by means of heating or low-pressure plasma.
2. Transportation of the vaporized material to the substrate surface.
3. Condensation onto the substrate.

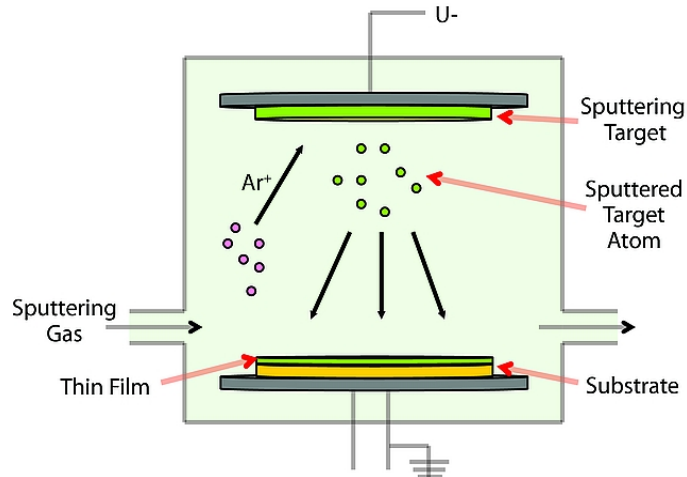


Figure 2.1 Schematic diagram of a sputter deposition [153].

The most common PVD processes are evaporation and sputtering, which are assisted by high-temperature vacuum and gaseous plasma, respectively. Specifically, during sputter deposition (*Figure 2.1*), the target material for the coating is bombarded and vaporized by accelerated gaseous ions (argon).

PVD techniques can be used to deposit a wide range of different materials, such as metals, ceramics, and semiconductors. Coatings of alloys are based on co-deposition from multiple sources, while compound materials (such as ZnO, TiO₂ or Cu₂O) are deposited by introducing oxygen during the transportation stage [154].

Environmentally friendly PVD processes produce coatings with high hardness, durability, and resistance to corrosion and wear. PVD coatings are used in a variety of applications, including thin film solar cells, automotive industry, and cutting tools [155].

2.1.1.3 Chemical vapor deposition (CVD)

Chemical vapor deposition (CVD) is a deposition technique, which is widely used in semiconductor applications to produce thin films. In contrast to PVD, the formation of the thin coating on the substrate is due to a chemical reaction of vapor phase precursors [156]. Gaseous phase chemical reactants are delivered into the reaction chamber, where they react or decompose on the surface of the thermal heated solid wafer (substrate). Temperature and duration of the deposition control the thickness of the deposited coating.

Thin films produced by CVD are uniform, pure, and compacted. On the other hand, the processes require a much higher temperature than PVD, and, moreover, some precursors are flammable, corrosive, and toxic [157].

In case the precursor is a metal-organic compound, the process is called metalorganic chemical vapor deposition (MOCVD). Another important “subclass” of CVD is the atomic layer deposition (ALD), a key method in the synthesis of thin films for semiconductor devices.

2.1.1.3.1 Atomic layer deposition (ALD)

Atomic layer deposition (ALD) is a chemical vapor phase technique which can be used to produce thin films of a variety of materials. The deposition process relies on sequential alternating pulses of the different vapor precursors, which are separately introduced into the chamber under vacuum. The reaction of the single gas phase precursor with the substrate is called ‘half reaction’ and leaves only one monolayer at the surface (self-terminating surface reactions). After the first deposition, the ALD reactor is purged with an inert gas to avoid reactions with further precursors which would lead to inaccurate thicknesses. Then a second reactant precursor can be introduced in the chamber, following the same steps (*Figure 2.2*). Several cycles of vapor precursor pulses and purging pulses are needed to achieve the desired film thickness [158].

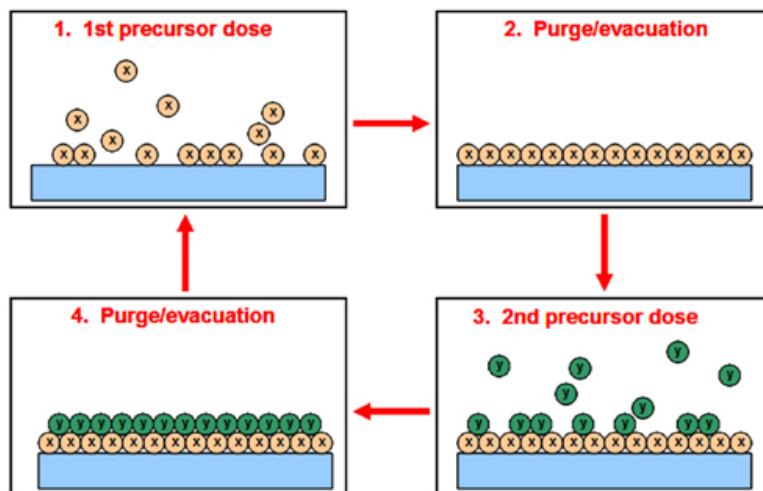


Figure 2.2 Basic schematic of the ALD process [159].

ALD has emerged as a powerful synthesis technique for the deposition of metal oxide thin films in photovoltaic applications. This is due to its advantages arising from the peculiar deposition process [160]:

- Exceptional conformality of the thin film.
- Tunable film composition.
- Simple thickness control, which is tailored by the number of ALD cycles.
- Modest deposition temperature (< 350 °C).

2.1.2 Samples preparation

2.1.2.1 Planar $\text{Cu}_2\text{O}/\text{ZnO}$

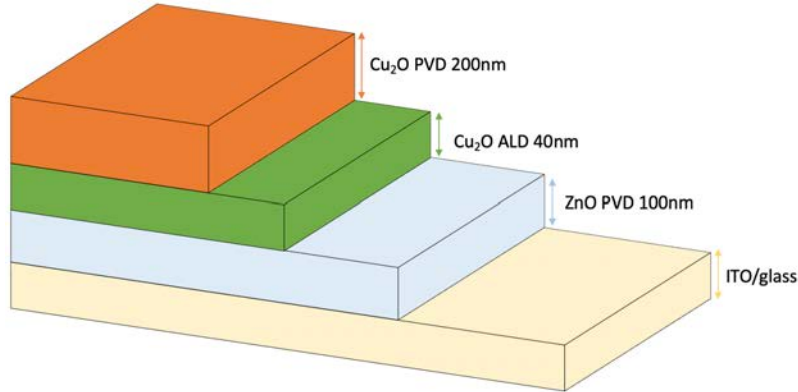


Figure 2.3 Sketch of the planar $\text{Cu}_2\text{O}/\text{ZnO}$ heterostructure.

This sample is in collaboration with the University of Lorraine (Nancy). It has been prepared by subsequent deposition on an ITO/glass substrate, as follow: first, 100 nm thick layer of ZnO has been deposited by sputtering, 40 nm of Cu_2O deposited by ALD and an additional 200 nm Cu_2O layer deposited by reactive magnetron sputtering (*Figure 2.3*). More details on both the sputtering and ALD processes have been reported by de Melo et al. [161].

The novelty of this architecture is the 40 nm of Cu_2O deposited by ALD, sandwiched between the two sputtered layers. This additional film is amorphous, and it acts as “blocking layer”, which helps the charges separation.

2.1.2.2 1D $\text{Cu}_2\text{O}/\text{ZnO}$

ZnO NWs have been synthesized by hydrothermal method [151] on a fluorine doped tin oxide (FTO) coated glass (Pilkington TEC 15, 15 ohm/sq). Firstly, the FTO glass was accurately washed using distilled water, acetone, and ethanol, sequentially. Then, a seed layer of ZnO was deposited by spin coating 0.1 M of zinc acetate dihydrate ($\text{Zn}(\text{CH}_3\text{COO})_2 \cdot 2\text{H}_2\text{O}$) in ethanol ($\text{C}_2\text{H}_6\text{O}$). Finally, the sample is inserted in an ambient atmosphere furnace at 450°C for one hour. Once the seed layer is formed, the nanowires are grown starting from two aqueous solutions: 100mM of zinc nitrate hexahydrate ($\text{Zn}(\text{NO}_3)_2 \cdot 6\text{H}_2\text{O}$) and 100mM of hexamethylenetetramine (HMT).

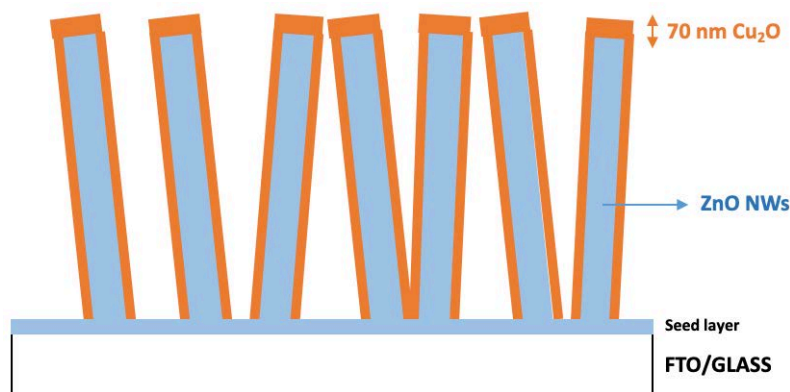


Figure 2.4 Sketch of ZnO NWs covered by Cu₂O thin film.

They are mixed together for a few minutes and then put in an autoclave, in which the FTO/seed layer sample was placed. Then, the autoclave is closed and placed in an oven at 95°C for 3 hours. At the end of the procedure, the sample is washed in distilled water to remove surface impurities, and it looked opaque, a witness of the growth of ZnO NWs.

The p-type copper oxide layer has been synthesized through metalorganic chemical vapor deposition (MOCVD). A horizontal, reduced pressure hot-wall reactor made of a silica tube was employed to perform the deposition of copper oxide. $Cu(tmhd)_2$ (Copper bis (2,2,6,6-tetramethyl-3-5-heptandionate), that is the precursor purchased from Sigma-Aldrich, has been used without further purification. Firstly, the reactor was evacuated by means of a scroll pump unit. An MKS Baratron 12AAX manometer measured the total pressure, which was in the range 4-5 Torr. Oxygen (O₂) and argon (Ar), which have been previously purified, were used as reaction and carrier gases, respectively. The mass flow rates were controlled using MKS type 247 electronic control unit and MKS 1160 flow controllers.

The thickness and the phase composition of the Cu₂O layer are related to the deposition parameters of the MOCVD process. Specifically, the sample 70nm Cu₂O/ZnO (*Figure 2.4*) has been obtained using:

- Deposition temperature = 250 °C.
- Deposition time = 30 minutes.
- Precursor temperature = 130 °C.

2.1.2.3 Planar $\text{Co}_3\text{O}_4/\text{ZnO}$

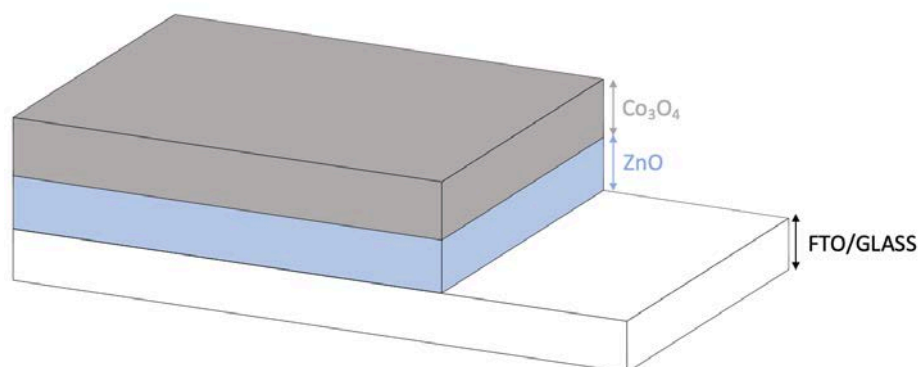


Figure 2.5 Schematic illustration of ZnO thin film covered by a Co_3O_4 layer.

All the samples are prepared on FTO/glass, which is firstly cleaned with tap water, distilled water, and ethanol. The ZnO thin film was deposited by atomic layer deposition (ALD), using diethyl zinc ($(\text{C}_2\text{H}_5)_2\text{Zn}$) and water (H_2O) as precursors. A set-up of 1.01 Å per cycle at a temperature of 150 °C allowed to achieve two different thicknesses (*Table 2.1*):

- 250 nm, by applying 2150 cycles.
- 500 nm, by applying 4300 cycles.

Co_3O_4 , which is the p-type oxide, was deposited on the ZnO thin film by ALD (*Figure 2.5*). Cobalt Alkyl Amidinate and water were used as precursors with a set-up of 0.66 Å per cycle at 200 °C. At the end of the process, the achieved thickness of Co_3O_4 is about 100 nm.

Table 2.1 Main parameters and achieved thicknesses of the ALD layers.

<i>Name of the sample</i>	<i>ZnO [nm]</i>	<i>Temperature [°C]</i>	<i>Cycles</i>	<i>Co₃O₄ [nm]</i>	<i>Temperature [°C]</i>
$\text{Co}_3\text{O}_4/\text{ZTF250}$	250	150	2150	100	200
$\text{Co}_3\text{O}_4/\text{ZTF500}$	500	150	4300	100	200

2.1.2.4 1D $\text{Co}_3\text{O}_4/\text{ZnO}$

The synthesis of the ZnO NWs followed the same steps of the 1D $\text{Cu}_2\text{O}/\text{ZnO}$. The seed layer is prepared by spin coating from a 0.01 M solution of zinc acetate dihydrate ($\text{Zn}(\text{CH}_3\text{COO})_2 \cdot 2\text{H}_2\text{O}$) in ethanol. 100 μL of the solution is spin-coated on the substrate center at 3000 rpm. More precisely, the spin coater rotates slower the first five seconds (500 rpm), reaching and keeping 3000 rpm for the next 55 seconds. Then the FTO/glass is dried on a heater plate at 120°C for 10 minutes. All these steps are repeated four times before completing the seed layer synthesis with the heat treatment. The samples were placed in an ambient atmosphere furnace for 1 hour at 450 °C and let they cool down slowly inside the furnace. A solution 100mM of zinc nitrate hexahydrate ($\text{Zn}(\text{NO}_3)_2 \cdot 6\text{H}_2\text{O}$) and 10mM of hexamethylenetetramine (HMT).is then prepared and mixed in an autoclave, where the substrates were previously placed inside. The autoclave was heated at 95 °C for 3 hours. After the treatment, the samples are washed with distilled water and cooled down at room temperature

Before covering the NWs with Co_3O_4 , in four of the six samples, a ZnO thin film has been deposited by ALD (*Figure 2.6*). The achieved thicknesses, as well as cycles and temperatures, are reported in Table. Finally, the p-type material was deposited by ALD over the six samples. Cobalt Alkyl Amidinate and water were used as precursors with a set-up of 0,66 Å per cycle at $T=150$ °C, to achieve a thickness of 100nm. In *Table 2.2*, the ALD parameters of the different samples are summarized.

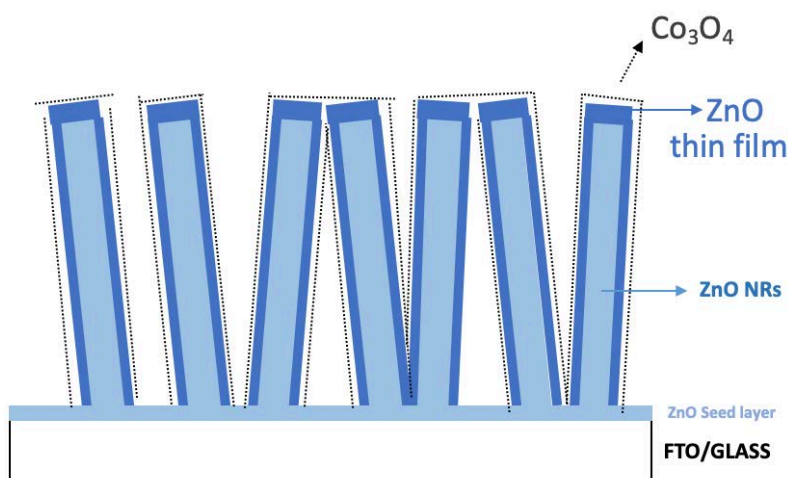


Figure 2.6 Sketch of ZnO NWs covered by ZnO and Co_3O_4 ALD layers.

Table 2.2 ALD parameters used in the synthesis of 1D Co₃O₄/ZnO.

Name of the sample	ZnO ALD [nm]	Temperature [°C]	Cycles	Co ₃ O ₄ ALD [nm]	Temperature [°C]
Co ₃ O ₄ /Z1D	-	-	-	100	150
Co ₃ O ₄ /ZnO250/Z1D	250	200	2150	100	150
Co ₃ O ₄ /ZnO500/Z1D	500	200	4300	100	150

2.1.2.5 Planar Co₃O₄/TiO₂

A thin film of TiO₂ is deposited by ALD on FTO/glass, after the standard procedure for cleaning the substrate. Titanium tetraiodide (TiI₄) and water (H₂O) are required as precursors, and a thickness of about 100 nm is achieved. Adopting the same deposition temperature (150°C) and 0.66 Å/cycle, the cobalt oxide layer is synthesized from Cobalt Alkyl Amidinate (preheated at 110°C) and water (*Figure 2.7*). The theoretical thickness of the Co₃O₄ layer should be 100 nm.

2.1.2.6 1D Co₃O₄/TiO₂

While the p-type layer is always prepared according to the same parameters, the n-type material is in the form of nanowires (NWs).

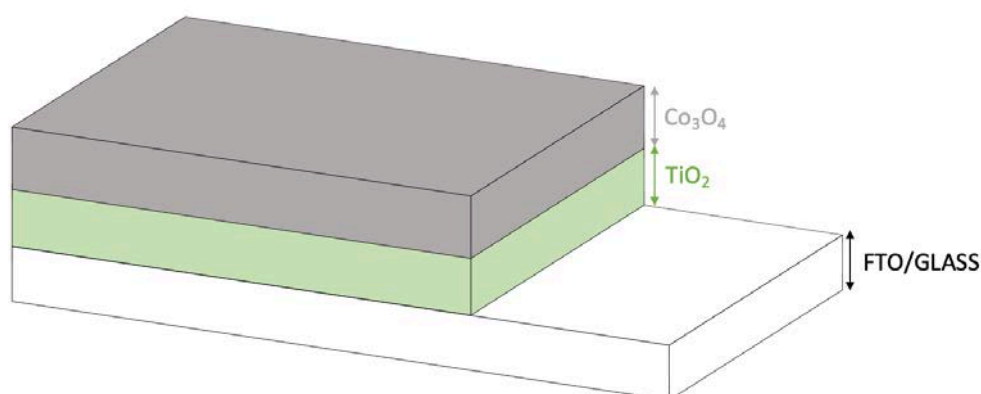


Figure 2.7 Schematic illustration of TiO₂ thin film covered by a Co₃O₄ layer.

Titanium butoxide ($Ti(OCH_2CH_2CH_2CH_3)_4$), absolute ethanol (C_2H_5OH), and acetic acid (CH_3COOH) are used to synthesize the seed layer. Hydrochloric acid (HCl), Titanium butoxide, acetone (C_3H_6O) and deionized water are used to grow the TiO_2 NWs. Two different procedures have been followed for the growth of the TiO_2 -seed layer and the TiO_2 NWs.

In the first approach [162], the cleaned substrate is immersed in a 1:25 (v/v) solution of titanium butoxide and absolute ethanol for 2 h under ultrasonic irradiation [9]. Then, the sample is annealed in argon for 1 h at $450^\circ C$. After the seed layer deposition, TiO_2 NWs are grown by solvothermal method. The samples are placed into a Teflon-lined stainless-steel autoclave with acetone (10 mL), hydrochloric acid (10 mL), and titanium butoxide (1.5 mL). Subsequently, the autoclave is put in an oven where the solvothermal reaction is performed for 1 h at $180^\circ C$. Then, the samples are ultrasonically cleaned in an isometric solution of deionized water and absolute ethanol for 10 minutes. As the last step, the samples are dried in air at $80^\circ C$ for 2 h.

In the second procedure [163], the TiO_2 -seed layer was grown onto the conductive side of the FTO glass by spin coating. 0.35 g of titanium butoxide, 10 mL of ethanol, and 2 mL of acetic acid are stirred for 2 h before 24 h of aging at room temperature. The obtained solution is coated on the substrate using a spin coater, at the rate of 500 rpm for 5 s and 3000 rpm for 30 s. The FTO/glass is then heated at $120^\circ C$ for 10 minutes, with the possibility to repeat the cycle. After this operation, the samples are annealed in a furnace, following the steps shown in *Figure 2.8*.

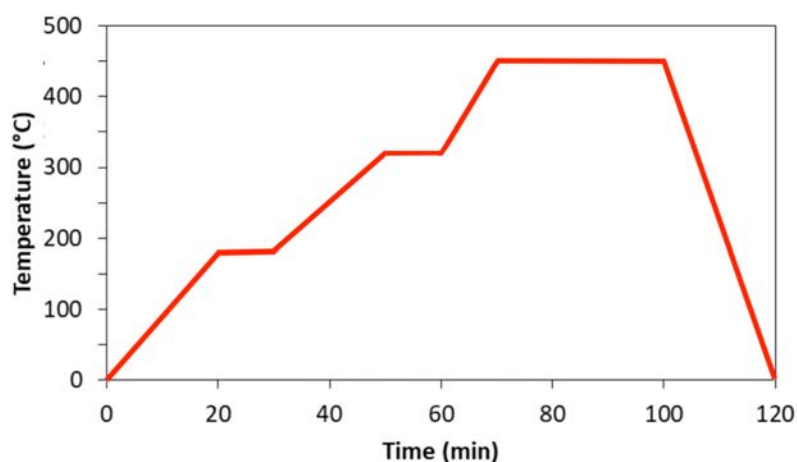


Figure 2.8 Annealing steps for the spin coated seed layer solution.

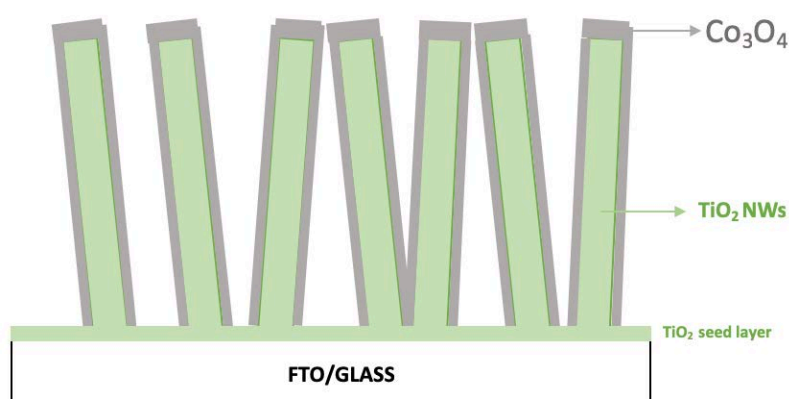


Figure 2.9 Sketch of TiO₂ NWs covered by Co₃O₄ thin film.

Once the seed layer is deposited, a hydrothermal method [164] is used for the synthesis of TiO₂ NWs. In this case, the solution contains titanium butoxide (0.03 M) and a mix (1:1v) of concentrated hydrochloric acid (37% by weight) and deionized water. The solution is stirred for 5 min, then 28 mL are transferred in an autoclave with the samples, and the thermal synthesis is carried out in an oven at 150°C for 4 h. Lastly, the samples are washed with deionized water and dried in a furnace (2h at 60°C).

In both the procedures, the NWs are covered by a Co₃O₄ thin film by ALD (*Figure 2.9*). The three different morphologies, as well as the different synthesis parameters, are summarized in *Table 2.3*.

Table 2.3 Summary table of the different Co₃O₄/TiO₂ architectures.

<i>Structure</i>	<i>Method</i>	<i>TiO₂</i> <i>ALD [nm]</i>	<i>Temperature</i> <i>[°C]</i>	<i>Co₃O₄</i> <i>ALD [nm]</i>	<i>Temperature</i> <i>[°C]</i>
Thin film	ALD	100	150	100	150
NWs	Solvothermal	-	180	100	150
NWs	Hydrothermal	-	150	100	150

2.2 Characterization

2.2.1 Electrical characterization

2.2.1.1 C-AFM

The electrical behavior at the nanoscale is studied by measuring local I-V curves with an NTEGRA AFM (NT-MDT) (*Figure 2.10*) in contact mode. Before any operations, the following initial procedures are needed [165]:

1. Launch the control program (*Nova 1.0.26, NT-MDT*);
2. Turn the instrument on;
3. Install the conductive nano-probe and adjust the cantilever detection system;
4. Mount the sample in a sample-holder;
5. Install the measuring head (STM for contact mode);
6. Approach the sample toward the tip at the distance of 0.5:1 mm.
7. Mount the protective hood, for a reduction of acoustic noises.

Subsequently, it is possible to run the measurements according to the next basic procedures [165]:

- i. Set the electronic configuration by selecting *Contact*.



Figure 2.10 NTEGRA AFM set-up [166].

- ii. Set the initial level for the deflection (DFL) and lateral force (LF) by clicking on *Aiming*. The value of the DFL depends on the position of the photodiode with respect to the laser reflected from the cantilever. It is important to set both the parameters at ~ 0 to have reliable measurements.
- iii. Select an optimal value of *set-point*. The *set-point* is a parameter concerning the magnitude of interaction between the sample surface and the tip. In contact mode, where the set-point correspond to the deflection of the cantilever, a small value of *set-point* leads to inadequately weak interactions, while big value may cause damage to both the probe and the sample.
- iv. Setting the *Feedback Gain* Factor. The greater its value, the higher the feedback loop data processing speed. However, above a threshold value, the signal becomes noisy. As for the *set-point*, the research of optimal *Feedback Gain* conditions requires operator experience.
- v. Approach the sample to the probe by clicking the buttons *Approach* and *Landing*. A good approach is reported in *Figure 2.11*.



Figure 2.11 Example of approach in a contact-mode AFM.



Figure 2.12 Outlook of the main operations panel of Nova AFM software.

- vi. Set parameters of scanning (Figure 2.12). By selecting *Scan* from the main operations panel, it is possible to modify several parameters, such as scanning frequency and size. In C-AFM is useful to record the morphology and the current distribution simultaneously by selecting the *Spreading Resistance* mode
- vii. Scanning. Depending on the selected mode, morphological and electrical images are taken and analyzed by the IA (Image Analysis) software. Furthermore, it is possible to record force curves and local I-V characteristics by clicking on *Curves*.

The force-versus-distance curves are a very important tool to measure the force (F) applied by the tip on the sample. In these curves, the deflection (DFL) of the tip is measured while varying the distance from the surface of the sample. As shown in Figure 2.13, the forward direction refers to the approach of the tip while the backward to its retraction from the surface. The force F can be determined by

$$F = \frac{DFL \cdot k}{b} \quad (2.1)$$

where k is the spring constant of the cantilever and b is the slope of the force curve.

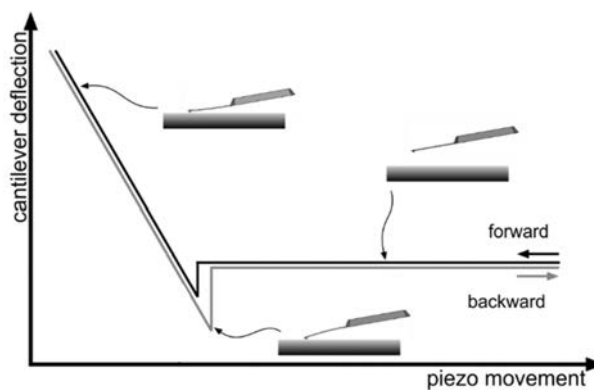


Figure 2.13 AFM force plot [167].

Table 2.4 Specific features of diamond coated conductive probes.

<i>Cantilever DCP20</i>	<i>Minimum</i>	<i>Typical</i>	<i>Maximum</i>
Length (μm)	-	90	-
Width (μm)	-	60	-
Thickness (μm)	1.7	2	2.3
Force Constant (N/m)	28	48	91
Resonant Frequency (kHz)	260	420	630

The C-AFM measurements are taken both in dark and light. The light source is a small white LED, which shines the samples from the bottom. Local I-V curves were produced on different sample positions by applying the voltage onto the FTO/ITO substrate while the AFM tip is grounded. The curves are reliable within the current range between -10 and +10 nA, then the response of the system is not linear.

In this work, diamond coated conductive probes (DCP20) have been used for analyzing the local electrical properties of the oxide heterojunctions. These chips are the best choice for long-term electrical characterizations, and their features include:

- Triangular cantilever;
- Standard thickness (0.4 mm) and sizes (1.6 x 3.6 mm) of cantilever chip;
- Au high reflectivity coating on the cantilever;
- Diamond coated tip, doped by nitrogen for conductivity;
- Curvature radius of the tip $\approx 100 \text{ nm}$;
- Other characteristics in *Table 2.4*.

2.2.1.2 IS-AFM

In order to perform IS-AFM measurements, a potentiostat (ModuLab XM ECS) has been coupled with AFM controller. The electronic connection between the potentiostat and the AFM was done thanks to the external box Signal Access Module SAM01 (Figure 2.14). In this way it was possible to control the input signal from an external source (the potentiostat) and modulate the range of frequency for the IS measurements from 1 MHz to 1 Hz.



Figure 2.14. Potentiostat ModuLab XM ECS (left) and Signal Access Module SAM01 (right) used coupled with AFM controller for IS-AFM measurements.

2.2.1.3 Macro electrical measurements

The macro electrical measurements were carried out by a source picometer (Keithley 2401) equipped with a solar simulator (LOT QuantumDesign). The sample is held in place by two brass metal screws, which also work as the contacts onto which the voltage is applied. The working electrode is in contact with the FTO substrate while the top oxide layer is grounded. This set-up replicates the AFM configuration, where forward bias occurs for $V < 0$ (negative voltage applied to the n-layer) and reverse bias for $V > 0$ (positive voltage applied to the n-layer).

The Keithley can measure the current and voltage in the range of 10 pA–1 A and 1 μ V–21 V, respectively. The solar simulator consists of a Xe lamp with an AM 1.5 - Global filter, which can generate UV-vis light with the power intensity of 1 Sun (1000 W/m²). The light intensity of the solar simulator is controlled through a calibrated silicon solar cell.

The samples were electrically characterized by tracking the J-V curves in dark and light, which shines the samples from the bottom on an area of 0.16 cm. The light passes through the FTO/glass substrate and reaches the active oxide layer of the device. Moreover, the time-dependent self-powered photo-response was measured at 0 V applied bias, under 1 sun simulated light irradiation in air and at room temperature [168].

2.2.2 Optical characterization

2.2.2.1 Spectrophotometer

Optical properties, such as absorbance and transmittance, are measured using a Cary 5000 spectrophotometer from Agilent technologies. It involves wavelength in the range of ultraviolet (UV) and visible (Vis), which have high energies capable of causing electronic transitions from HOMO to LUMO [169]. The visible range in the solar spectrum is 400-700 nm, while the UV light represents the wavelength 10-400 nm.

The working principle of the UV-Vis spectrophotometer is based on the amount of light absorbed or reflected by the sample. The intensity of the transmitted light (I) and the intensity of the incident light (I_0) from the UV-Vis source are compared to determine the amount of absorbed light. The ratio between them is called transmittance (T):

$$T = \frac{I}{I_0} \quad (2.2)$$

The absorbance (A) is defined according to the following equation:

$$A = -\log_{10} T \quad (2.3)$$

For quantitative analysis, the absorbance is expressed as a function of the concentration (C) of the absorbing molecules of the sample, the length (L) of the light path, and the molar extinction coefficient (ε). The expression, known as Lambert-Beer law, is:

$$A = -\log_{10} \frac{I_0}{I} = C \cdot L \cdot \varepsilon \quad (2.4)$$

ε [$M^{-1}cm^{-1}$] has a constant value for each specific compound, and it is a measure of the probability of electronic transitions.

An integrating spectralon sphere with reflectance > 95% in the 300 ÷ 1000 nm range is applied to get the diffuse reflectance. The reflectance is the ration of the amount of light reflected by a surface to the incident light.

UV-Vis spectroscopy can be used to determine the maximum absorption wavelength (λ_{max}) as well as the band gap of semiconductors through the Tauc plot, which is explained in *Chapter 3*.

2.2.2.2 Photoluminescence

Photoluminescence (PL) spectroscopy is a non-destructive, contactless technique in which electronic properties of semiconductors are determined by absorption of energy and subsequent emission of light. When photons with energy greater than the band gap are absorbed in the semiconductor sample, they create electron-hole pairs. The electron is excited to a higher electronic state (conduction band or energy levels within the band gap), then it returns to a lower energy state by emitting a photon [170].

The photons emitted from the specimen surface are the result of multiple recombinations of holes and electrons, which are witnesses of the variety of energy states in the semiconductor. These states are caused by the presence of different defects in the lattice. Their presence and typology (vacancies, interstitials, and impurities) can be determined by analyzing the photon emission spectrum. The energy redistribution due to recombination mechanisms causes the emission of a photon with lower energy than the absorbed light. Indirect transitions and excitonic recombinations are typical processes in which impurities trap the charge carriers. Besides the detection of defects and recombination methods, the PL spectrum can be used to determine the electronic band gap of the semiconductor.

Fluorescence and phosphorescence are particular forms of photoluminescence, depending on the lifetime of the excited state. While fluorescence is a very “fast” process, phosphorescence is a mechanism where the material does not immediately re-emit the absorbed photons.

In this work, PL spectroscopy is performed by an Edinburgh Instruments FLS980 Photoluminescence Spectrometer. The excitation wavelength and the spectral detection range changes between different samples. Thus, the detailed parameters are reported in *Chapter 3*.

2.2.3 Structural and morphological characterization

2.2.3.1 Scanning electron microscope (SEM)

Scanning electron microscope (SEM) is a microscope that used a finely focused electron beam as source of illumination. Since electrons have shorter wavelengths than those of visible light photons, SEM achieves higher resolving power, producing detailed images down to 1 nm. The accelerated electrons pass through a combination of lenses, which demagnify and focus the beam on the surface of the sample. The main components of an SEM are [171]:

- Electron gun (source of electrons);
- Electromagnetic lenses;
- Scan coils, which control the position of the high-energy beam;
- Electron detectors, which record the different signals from the electron-sample interaction;
- Sample chamber, where the sample is mounted;
- Computer and display to analyze the images.

As the electrons interact with the surface of the specimen, various signals are generated and collected by detectors. The displayed images give information about composition, surface topography, morphologies, etc. The interaction with the surface produces secondary electrons and Auger electrons. The former provides surface imaging and topography, while the latter deal with a surface chemical and elemental topography.

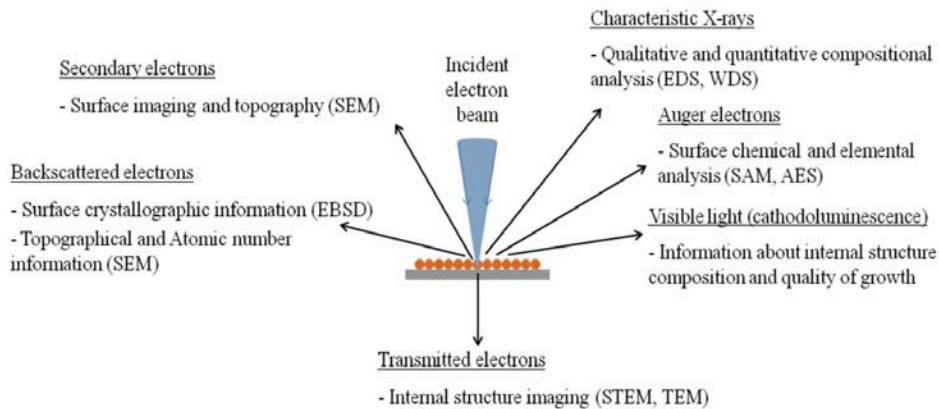


Figure 2.15 Diagram of signals from the beam-sample interaction and possible techniques [52].

Other signals rise when the beam penetrates to a depth of a few microns. Backscattered electrons give information about the crystal structure and grain orientation of crystals, by means of the electron backscatter diffraction (EBSD). At higher penetration depths, characteristic X-rays are used in techniques, such as energy-dispersive spectroscopy (EDS) and wavelength-dispersive spectroscopy (WDS), for a qualitative and quantitative compositional analysis. These and other signals are illustrated in *Figure 2.15*.

The samples in this thesis were characterized using a field emission scanning electron microscope (FE-SEM) ZEISS SUPRA 55 VP.

2.2.3.2 X-ray diffraction (XRD)

X-ray diffraction (XRD) was performed on a PANalytical X'Pert instrument operated in reflection mode. XRD is one of the most important non-destructive and versatile techniques to analyze the structure and the phase composition of different kind of samples. An X-ray beam is focused toward the surface of a crystalline sample: the interaction between the two goes through different processes, such as absorption, attenuation, and scattering. Remarkable information is revealed by measuring the angle and the intensity of the coherent scattering beam, according to the Bragg's law

$$n\lambda = 2d\sin(\theta) \quad (2.5)$$

where:

- n (an integer) is the order of reflection.
- λ is the wavelength of the incident X-rays.
- d is the interplanar distance between atomic planes in a crystal.
- θ is the scattering angle.

This law describes the conditions for constructive interference [172]. Since the wavelength of the incident radiation (0.1-100 Å) is comparable to atomic spacings, the X-rays can be reflected by the planes of the crystalline lattice, which are described by the Miller indices and separated by d . Intense scattered waves originate from the constructive interference, which occurs when the difference between the optical path length of the

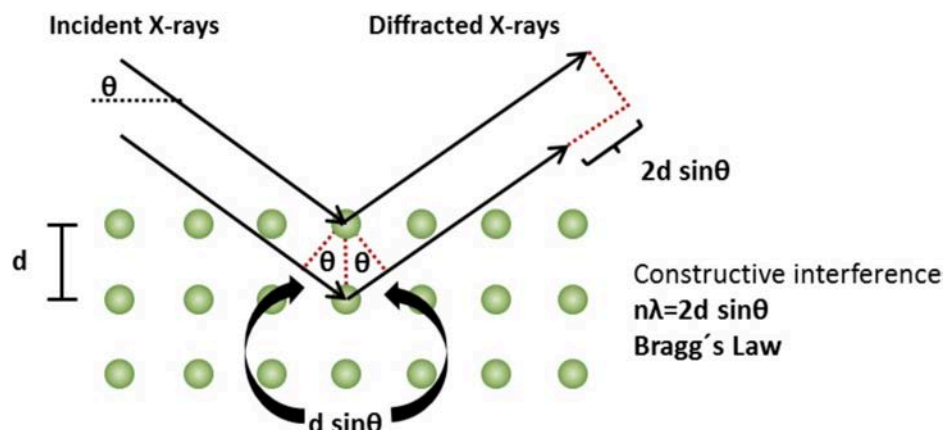


Figure 2.16 Schematic illustration of the Bragg's law [173].

reflected waves ($2d \sin(\theta)$) is an integer multiple of the wavelength ($n\lambda$) (Figure 2.16).

The output from an XRD analysis is a diffractogram, which shows the intensity of the diffracted radiation as a function of the angle of diffraction. It can be seen as the fingerprint of the sample since every crystalline material has a specific diffractogram. The obtained x-ray diffraction pattern helps to identify the crystalline phases in the target sample, by comparison with reference database and patterns.

2.2.3.3 Raman Spectroscopy

Raman Spectroscopy is a non-destructive characterization technique which detects vibrations in molecules by the interaction with the light. It provides information on chemical structures, physical forms, crystallinity, impurities, etc. Furthermore, the identification and the amount of a specific substance can be determined through the comparison with characteristic spectral patterns [174].

The working principle of Raman is based on the interactions of the light with matter. When a sample is exposed to visible light, the photons may be absorbed, transmitted, or, in a minute part, scattered by the molecules in all the directions. The energy of the incoming light must be different from any possible electronic transition, and the

scattered photons are collected by a detector installed in a right angle to the incident beam.

Raman spectroscopy adopts a monochromatic light to irradiate the sample, and the energy spectrum of scattered radiations is detected. The photons which make up the light interact with the molecules of the sample by polarizing the electronic cloud round the nuclei. Hence, an electron from a ground state rises to a short-lived energy state (*virtual state*). In this process, the transferred energy is given by the formula

$$E = h \cdot \nu \quad (2.6)$$

where h is the Planck constant and ν is the frequency of the incident photons. The virtual state is unstable, and the electron falls back to a lower energy level. If the energy lost equalizes that of the incident light, the electron returns to its initial vibrational level by emitting a photon. The emitted photon has the same frequency of the incident ones, and the process is called Rayleigh Scattering. However, when losing energy from the virtual state, electrons can fall back to a different vibrational level. In this case, the energy lost by the electron is different from that of the incident light. This is due to the different frequencies between the emitted photon (ν_s) and the incident ones (ν_i), and the process is known as Raman Scattering.

Depending on the final energy level of the electron, it is possible to distinguish Stokes Scattering and anti-Stokes Scattering. The former concerns an electronic transition that ends up to a higher vibrational level by absorbing energy.

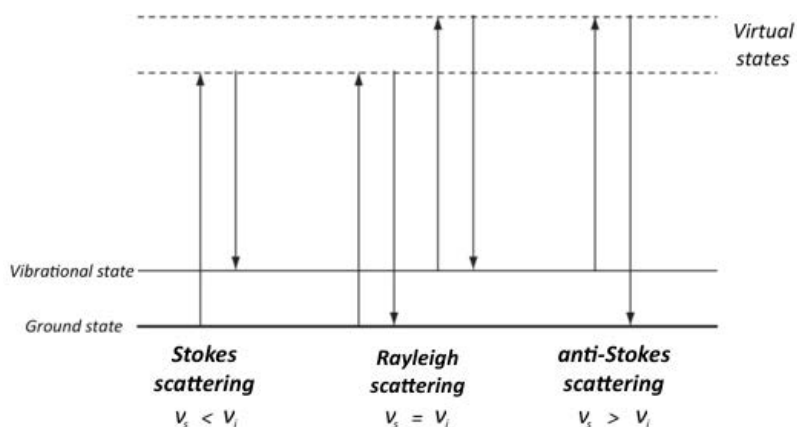


Figure 2.17 Schematic diagram of different scattering processes (adapted from [174]).

The latter involves emitted photon having a greater frequency than the one of the incident light, while the electron from a higher vibrational level falls back to the ground state energy level. Rayleigh and Raman scattering processes are shown in *Figure 2.17*.






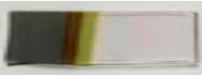


A Raman spectrum shows a number of peaks, which correspond to a specific molecular bond vibration. The position and the intensity of the Raman scattered light provides a unique molecular fingerprint, either for qualitative or quantitative analysis. In this work, the scattered intensity versus wavenumber spectra have been obtained with an excitation wavelength of 532 nm, using a SENTERRA Raman microscope.

3 RESULTS AND DISCUSSION

Different samples and geometrical combinations have been analyzed in this work. They are discussed with the aim of comparing 1D nanostructures with their thin film counterparts. $\text{Cu}_2\text{O}/\text{ZnO}$ heterostructures are one of the most mature technologies in the field of AOSCs, whereas the use of Co_3O_4 as the absorbing layer represents a recent challenge in PV applications.

3.1 List of samples

Table 3.1 List of samples having ZnO as n-type material.

<i>1D ZnO</i>			<i>Planar ZnO</i>		
<i>Name of the sample</i>	<i>Description</i>	<i>Picture</i>	<i>Name of the sample</i>	<i>Description</i>	<i>Picture</i>
<i>Z1D</i>	Bare ZnO NWs		<i>ZTF250</i>	250 nm ZnO thin film	
<i>250ZnO/Z1D</i>	250 nm of ZnO on top of Z1D		<i>ZTF500</i>	500 nm ZnO thin film	
<i>500ZnO/Z1D</i>	500 nm of ZnO on top of Z1D		<i>Cu₂O/ZTF</i>	Double layer of Cu ₂ O (PVD and ALD) on top of planar ZnO	
<i>Cu₂O/Z1D</i>	Cu ₂ O on top of Z1D		<i>Co₃O₄/ZTF250</i>	Co ₃ O ₄ on top of ZTF250	








$Co_3O_4/Z1D$	Co_3O_4 on top of Z1D		$Co_3O_4/ZTF500$	Co_3O_4 on top of ZTF500	
$Co_3O_4/250ZnO/Z1D$	Co_3O_4 on top of 250ZnO/Z1D				
$Co_3O_4/500ZnO/Z1D$	Co_3O_4 on top of 500ZnO/Z1D				

Table 3.2 List of samples having TiO₂ as n-type material.

<i>1D TiO₂</i>			<i>Planar TiO₂</i>		
<i>Name of the sample</i>	<i>Description</i>	<i>Picture</i>	<i>Name of the sample</i>	<i>Description</i>	<i>Picture</i>
<i>T1D</i>	TiO ₂ NWs		<i>TTF</i>	TiO ₂ thin film	
<i>T1D (compacted)</i>	Compacted TiO ₂ NWs		<i>Co₃O₄/TTF</i>	Co ₃ O ₄ on top of TTF	
<i>Co₃O₄/T1D</i>	Co ₃ O ₄ on top of T1D				
<i>Co₃O₄/T1D (compacted)</i>	Co ₃ O ₄ on top of T1D (compacted)				

3.2 Cu₂O/ZnO heterostructures (1D)

The sample *Cu₂O/Z1D* has been previously described in *paragraph 2.1.2.2*. The synthesis and most parts of the analysis have been carried out in the Department of Engineering Sciences and Mathematics at Luleå University of Technology. The sample, together with others having different thicknesses of the Cu₂O layer, has been already discussed by Ghamgosar et al. [168]. Since their results are helpful for this work, a summary of morphological, structural and electrical properties is reported.

The SEM analysis points out a grass-like layer of quasi-perpendicular ZnO NWs, which have a length of 1.1 μm and an average diameter of (71 ± 7) nm. They are covered by a smooth and homogenous layer of Cu₂O, resulting in a core-shell diameter of about (110 ± 10) nm. The XRD patterns (*Figure 3.1*) show an intense (002) diffraction peak at 34.4°, both before and after the copper oxide deposition.

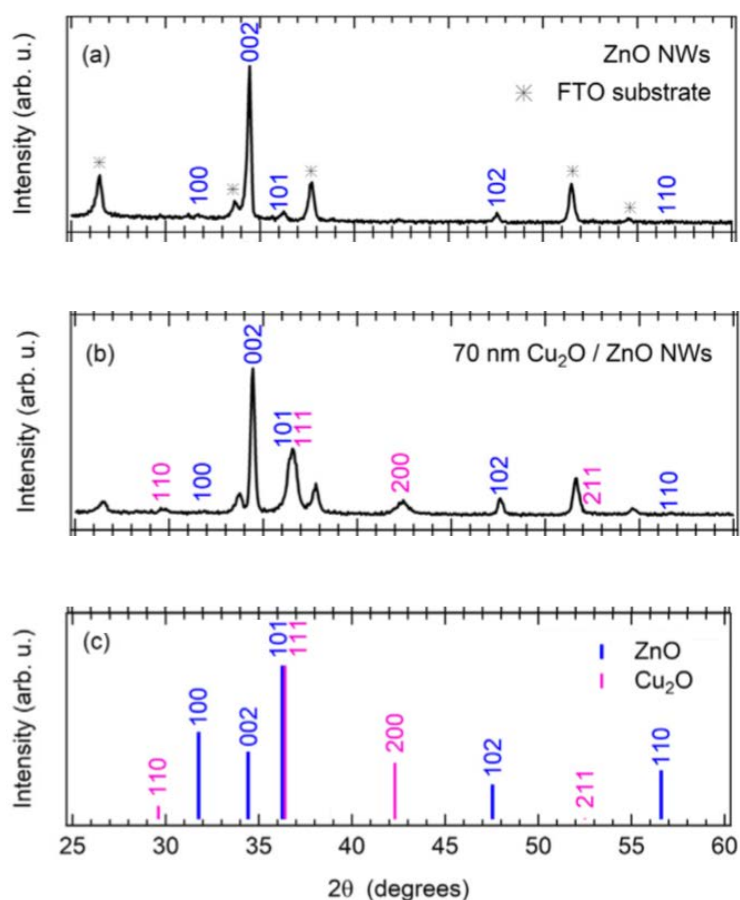


Figure 3.1 XRD patterns of bare ZnO NWs (a), ZnO NWs covered by 70 nm Cu₂O (b), ZnO and Cu₂O reference (c) [168].

This peak confirms ZnO NWs characterized by a wurtzite structure with a hexagonal unit cell. The angles equal to 29.6°, 36.5°, and 42.3° correspond to the diffraction of (110), (111) and (200) lattice planes of Cu₂O, which is the only crystalline phase present for copper oxide.

J-V curves in dark and light reveal the electrical behavior of the ZnO NWs covered by Cu₂O. By exposing 0.16 cm² of the sample to 1 Sun, the photo-response mechanism is investigated. As subsequently confirmed by C-AFM measurements, the FTO substrate exhibits a linear ohmic behavior, while the bare ZnO NWs show a rectifying J-V curve in dark. This rectifying behavior could be due either to the n-n junction with FTO or the Schottky junction with the brass screws (metal contact). When the NWs are illuminated, they become more conductive for both forward and reverse bias, overcoming the weak effect of the junction. On the contrary, a p-n junction is formed when Cu₂O is deposited on ZnO NWs, and the sample keeps a rectifying behavior also under illumination. They observed that the flowing current is maximized by increasing the thickness of the Cu₂O layer up to 240 nm. Although an enhanced conductivity under illumination, no photovoltaic effect was observed in the J-V curves. Therefore, these ZnO-Cu₂O core-shell nanowires cannot work as solar cells.

Nevertheless, it is possible to take advantage of the underlying properties under light in stable and fast response photodetectors. The photo-response mechanism is illustrated in *Figure 3.2*. The sketch shows the depletion region and the electronic band bending, which promote the separation of charge carriers generated under illumination, at 0 V bias applied.

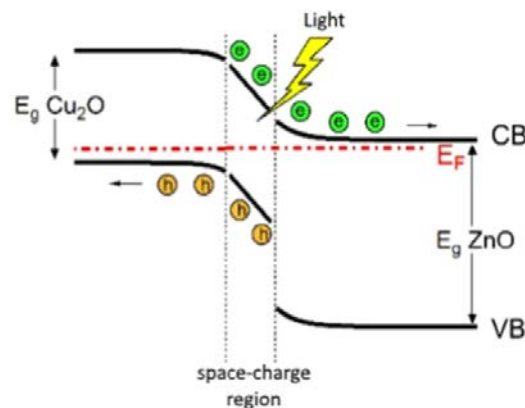


Figure 3.2 Electronic band bending and photo-response mechanism of Cu₂O/ZnO heterojunction.

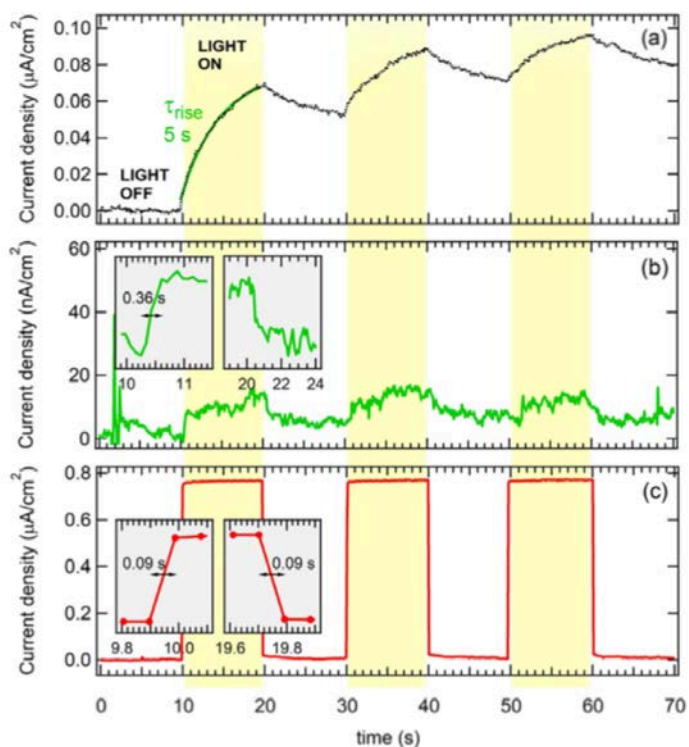


Figure 3.3 Photoresponsivity of a) bare ZnO NWs, b) 70 nm Cu₂O/ZnO NWs and c) 240 nm Cu₂O/ZnO NWs [168].

The photoresponsivity of the sample is measured through dark and light cycles of 10s, as depicted in *Figure 3.3*. The sample with 70 nm Cu₂O (*Figure 3.3b*) shows a very low current density (10 nA/cm²) and slow response and recovery to light exposure. Although the rise time (0.36 s) is higher than the bare ZnO NWs (*Figure 3.3a*), the performance under illumination are not optimized. In particular, they found out that the fastest response to light and recovery times are achieved by increasing the thickness of Cu₂O up to 240nm (*Figure 3.3c*), which guarantees at the same time a high photogenerated current density (of the order of μA/cm²). Besides the suitable thickness, the enhanced photo-response can be ascribed to the favorable Cu₂O band gap (2.48 V), which gives a substantial contribution in the light absorption.

In order to deeply understand the electronic properties of the sample, local current and impedance measurements have been carried out by using C-AFM. DCP 20 nanoprobe have been used to analyze the electrical behavior down to the nanoscale, and the sketch of the instrument is shown in *Figure 3.4*.

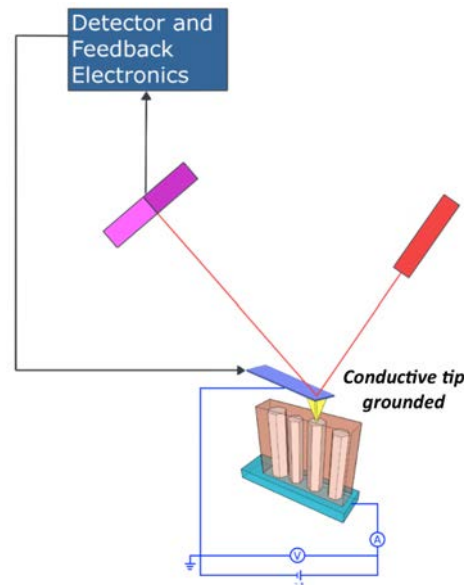


Figure 3.4 Sketch of the C-AFM set-up.

The conductive tip is grounded, and the bias is applied on the FTO substrate. According to this configuration, the forward bias corresponds to $V < 0$, while the reverse to $V > 0$.

I-V curves have been measured on FTO substrate, bare ZnO NWs and Cu₂O/ZnO NWs. As for FTO, force curves (*Figure 3.5*) and I-V characteristics (*Figure 3.7*) were taken by applying different values of set-point. Taking into account the formula (2.1), the force applied on the sample was calculated from the slope of the curves, the spring constant of the tip (48 N/m) and the initial deflection (0.01 nA). The force approximately varies from 200 nN to 1200 nN by changing the value of the set-point from 0.1 to 0.6. Then a $1\mu\text{m} * 1\mu\text{m}$ electric image (*Figure 3.6*) was taken by applying a voltage of 0.1 V and a set-point of 0.1. As pointed out by the figure, the FTO substrate shows a lack of homogeneity in terms of current at the nanoscale. This is at the end expected, since FTO is not a metal, but a semiconductor presenting conductive grains. In other words, it was possible to get current just when the tip was in contact with the brightest area of the image. Lastly, the I-V curves (*Figure 3.7*) confirm the linear ohmic behavior previously found with the macro electrical measurements. A less stable curve was obtained with the highest set-point probably because of micro-movement of the sample during the scanning. In the case of FTO, the different forces between the sample and the tip do not affect the value of the local current.

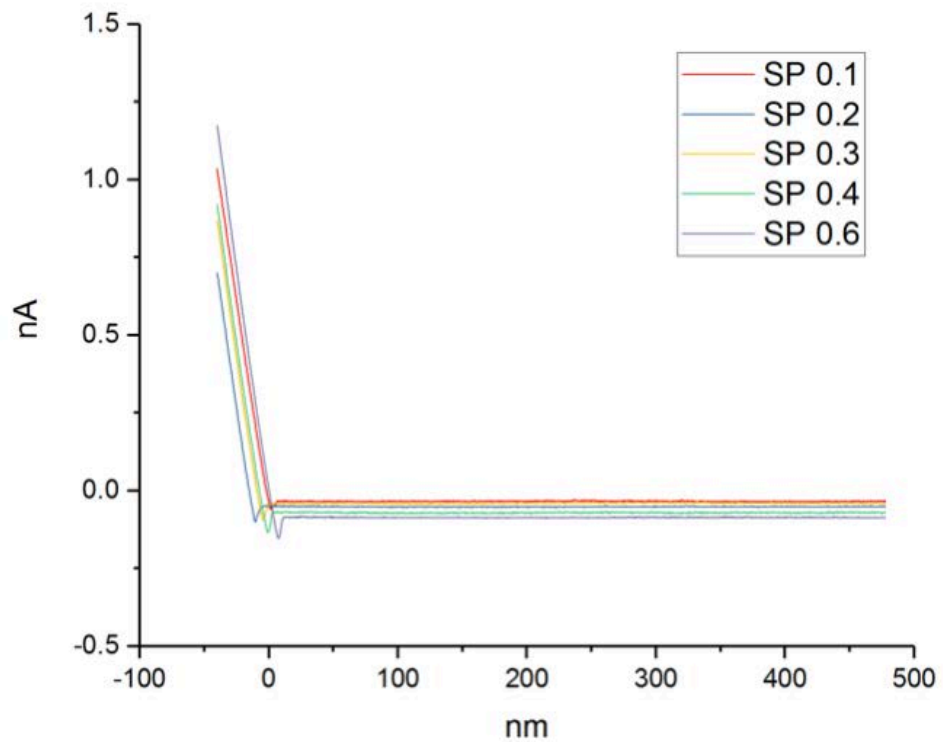


Figure 3.5 Force curves taken on FTO substrate by applying different set-point.

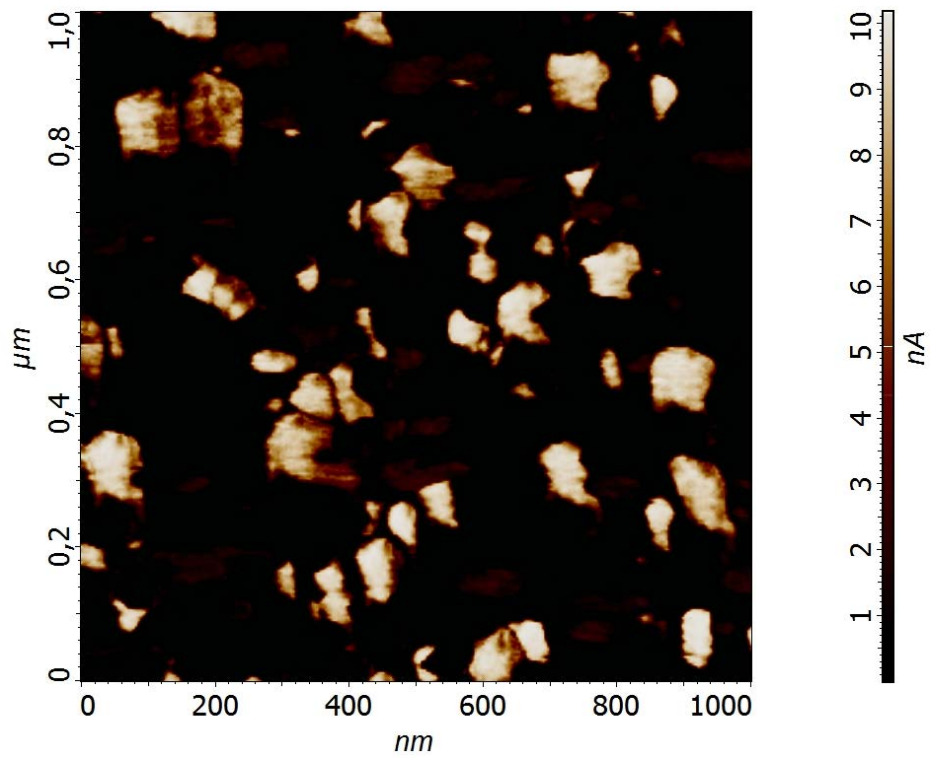


Figure 3.6 Local electric image of FTO (Voltage = 0.1V).

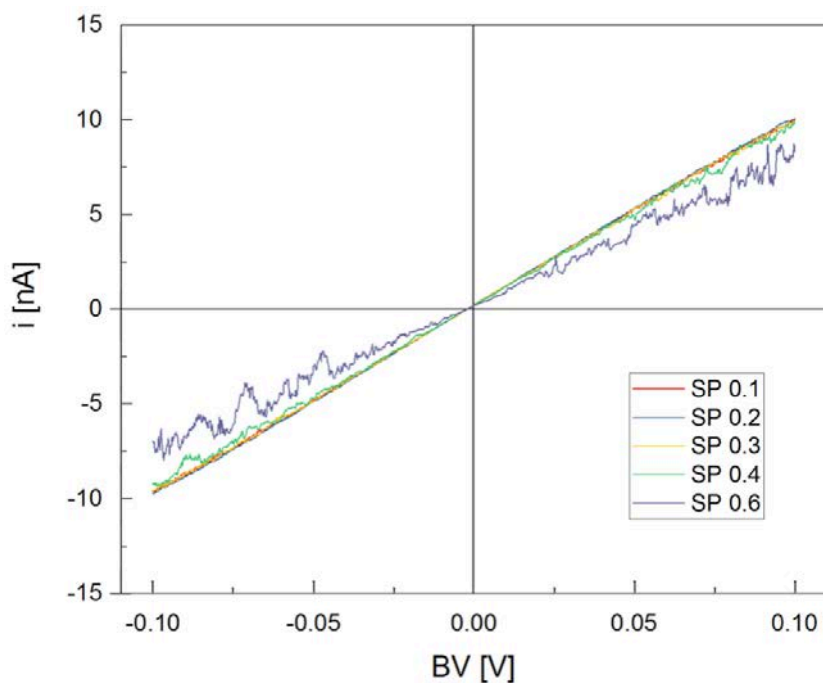


Figure 3.7 Dark I-V curves for FTO at different values of set-point.

The same procedure was performed on bare ZnO NWs. As depicted in *Figure 3.8*, they show a rectifying behavior also at the nanoscale. The nano-Schottky junction between the tip and the sample allows the flow of the current only in forward bias, which occurs at negative voltages.

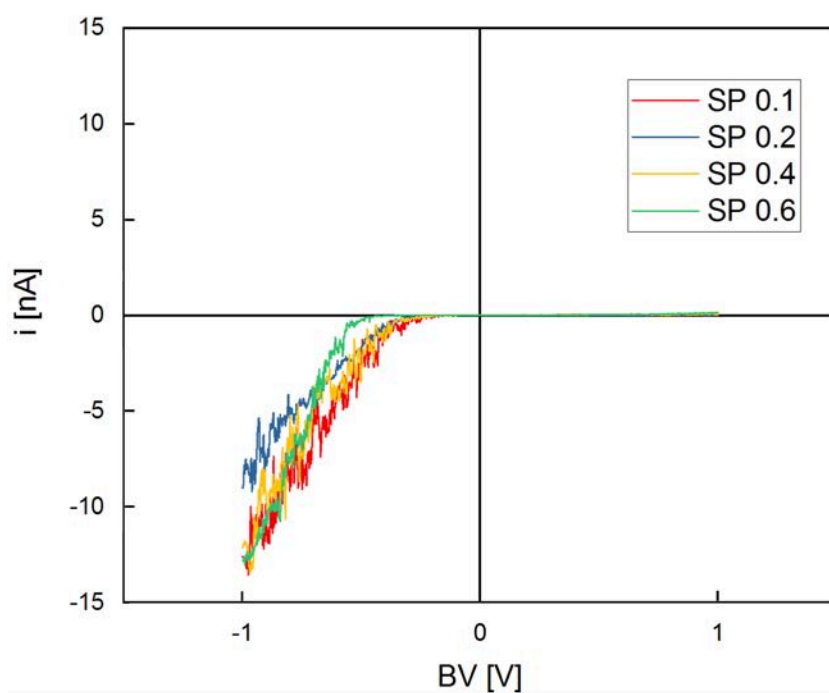


Figure 3.8 Dark I-V curves for ZnO NWs at different values of set-point.

Lastly, 70 nm $\text{Cu}_2\text{O}/\text{ZnO}$ NWs was electrically characterized by using the same parameters and set-up. The first C-AFM measurements (*Figure 3.9*) display very noisy curves, most likely caused by a bad contact of the tip with the surface of the sample. This can be due either to the presence of dust or damage on the tip.

The same measurements were repeated after changing the probe: by using a new DCP20, the approach was easier, and the curves look stable (*Figure 3.10*). The local I-V curves were obtained in a specific area of the sample, by sweeping the voltage between -1V and +1V. The rectifying behavior highlights the presence of the p-n junction, which allows current up to 10nA when a negative voltage is applied. The shape of the curve did not change when a small LED was turned on (yellow line in *Figure 3.10*). As already pointed out in the macro measurements, the performance under light for this specific sample are weak, and it is necessary to increase the thickness of the p-type oxide to enhance its photoresponsivity.

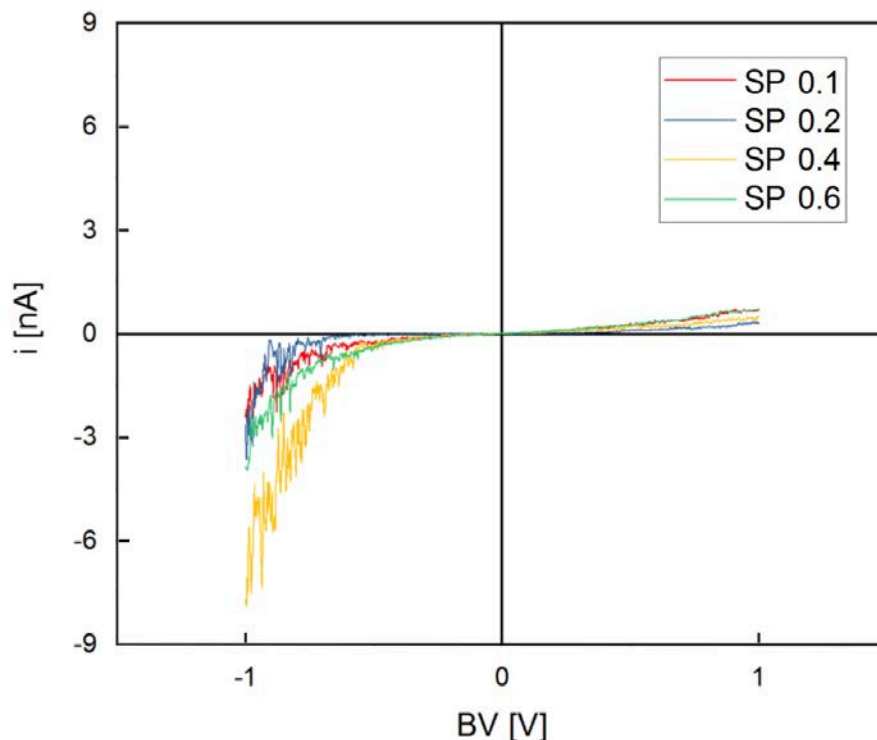


Figure 3.9 Dark I-V curves for 70 nm $\text{Cu}_2\text{O}/\text{ZnO}$ NWs at different values of set-point.

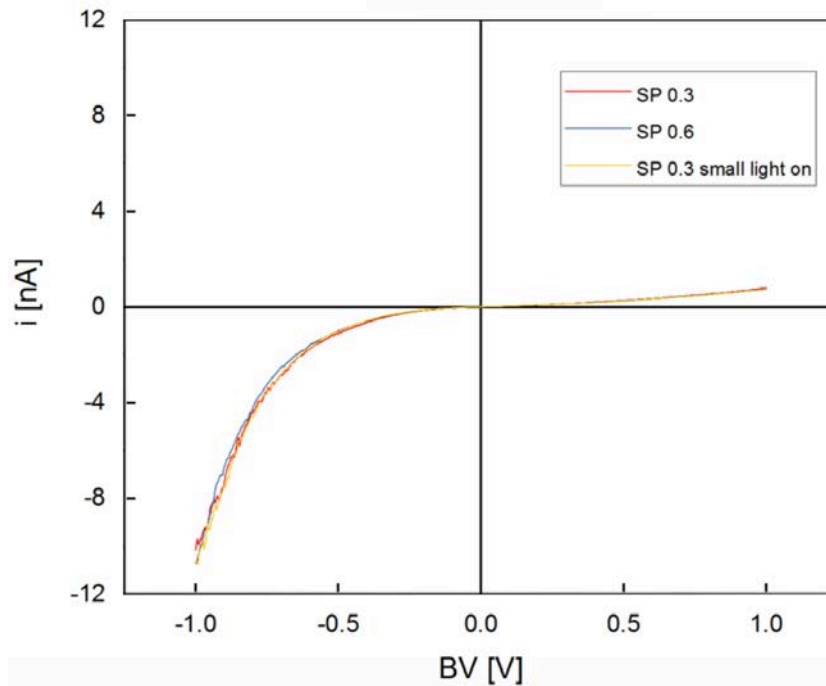


Figure 3.10 Dark and light I-V curves for 70 nm Cu₂O/ZnO NWs.

To determine the sample series resistance at the nanoscale, a novel characterization technique consists in coupling the AFM configuration with a potentiostat, which carries out impedance spectroscopy measurements. The IS-AFM spectra on the FTO substrate are reported in *Figure 3.11*, in which the circular shape of the curves remains the same, regardless of the value of the set-point. The colored dots can be fitted by equivalent circuits, through which the Cole-Cole plot is built (*Figure 3.12*). The series resistance of FTO is in the order of $10^7 \Omega$, which is higher than the value from the macro-measurements. This is due to the nano-contact between the tip and the surface, in which quantum effects can play an important role.

IS-AFM data of *Z1D* and *Cu₂O/Z1D* are difficult to be treated through equivalent circuits. The use of a nanoprobe as counter electrode leads to a new interface, which shall be added to the existing ones (ZnO/FTO, Cu₂O/ZnO, ...). However, these data can qualitatively be compared with macro IS measurements, previously taken on the same samples. *Figure 3.13a* and *Figure 3.14* show macro- and nano-impedance spectroscopy results, respectively. A simple equivalent circuit made of a series resistance (R_1) and an RC pair (R_2 - C_1 , which is related to the ZnO/FTO interface) is used to fit the data.

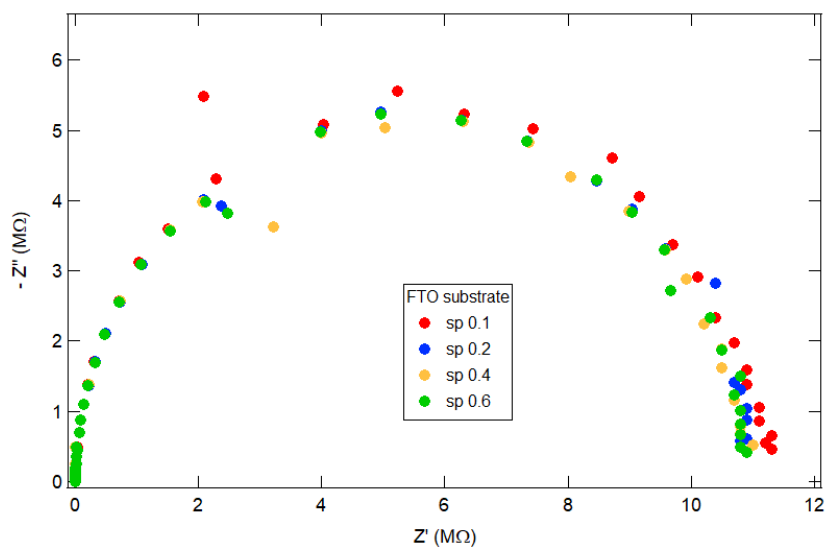


Figure 3.11 IS-AFM data from FTO substrate.

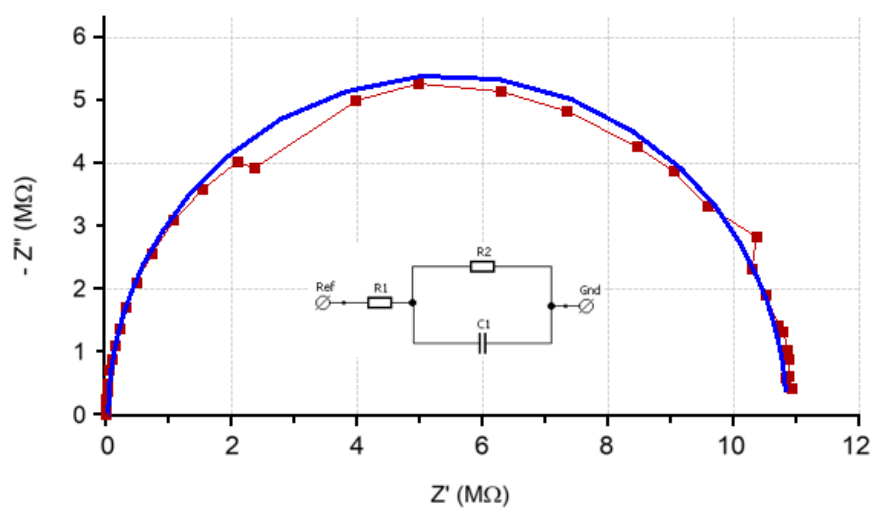


Figure 3.12 Fitting results of the IS-AFM data from FTO substrate.

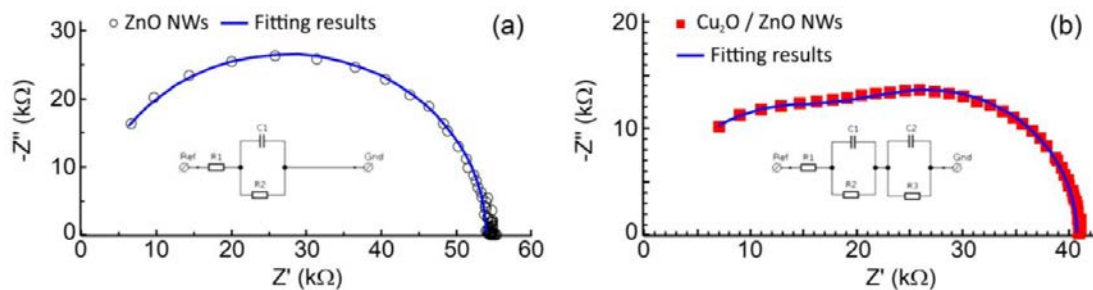


Figure 3.13 Cole-Cole plot of (a) bare ZnO NWs, b) Cu₂O/ZnO NWs.

As far as the local results are concerned, the high resistance of the sample does not allow a complete circle, and it is difficult to simulate the data. Adding the NWs on top of FTO results in a higher (of about two orders of magnitude) local resistance.

A more complex equivalent circuit is required to fit the data of Cu₂O/ZnO. The second RC pair in *Figure 3.13b* takes into account the presence of the Cu₂O/ZnO junction. When a set-point 0.1 is applied on the sample, the effect of the double junction is visible through the presence of a double circle (red curve in *Figure 3.15*). When the force applied to the sample increases (set-point 0.6), the curve is similar to the one of ZnO NWs, which means that the tip is in contact with the FTO substrate.

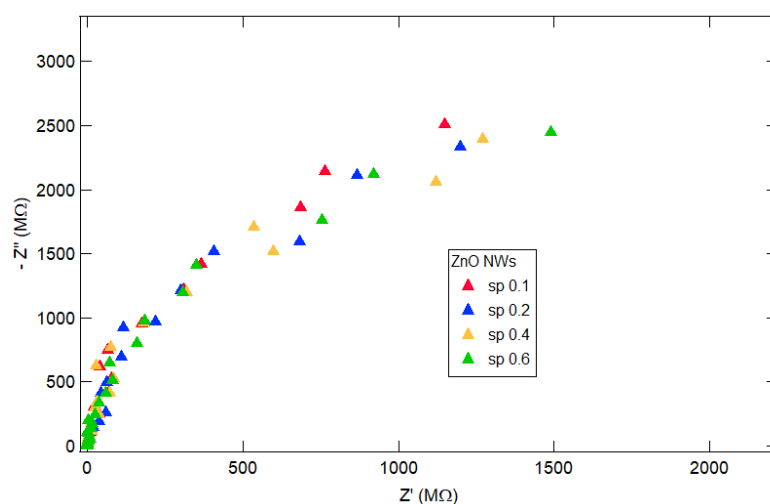


Figure 3.14 IS-AFM data from ZnO NWs.

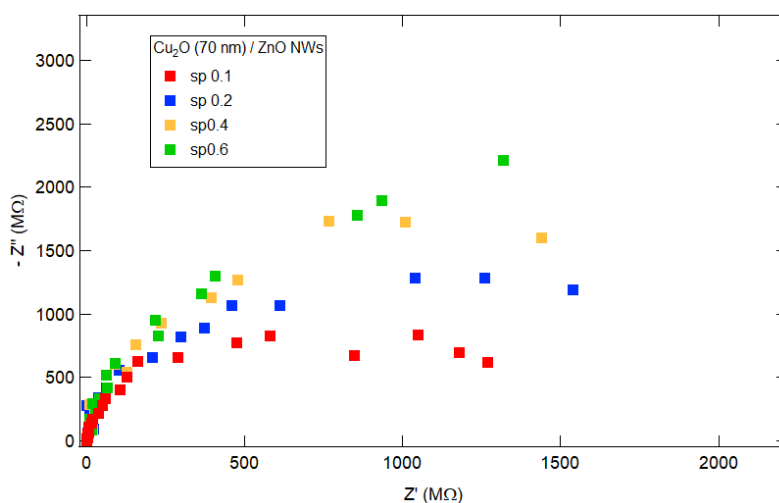


Figure 3.15 IS-AFM data from 70 nm Cu₂O/ZnO.

In summary, both the macro and the local electrical characterization confirm the presence of a p-n junction (*Figure 3.16*). The sample can work as a diode, that is an electronic device that conducts current only in one direction. The presence of the p-n junction seems confirmed by IS data, in both local and macro measurements (*Figure 3.15* and *Figure 3.13b*, respectively). Unfortunately, the sample does exhibit very less efficient photovoltaic properties.

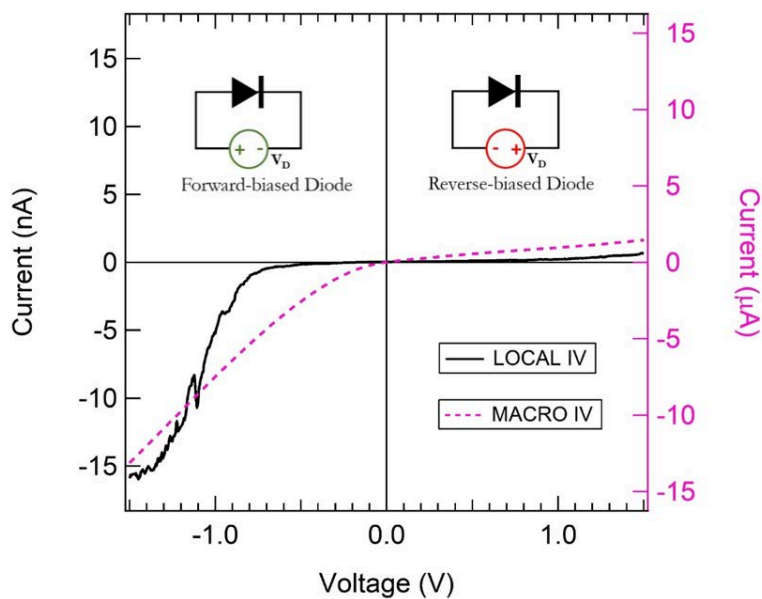


Figure 3.16 Macro and local I-V curves in dark for 70 nm $\text{Cu}_2\text{O}/\text{ZnO}$ NWs

3.3 Cu₂O/ZnO heterostructures (thin film)

To date, in the field of AOSCs, thin film technology is much more developed compared to nanostructured architectures. Optoelectronic devices made of thin layers of ZnO and Cu₂O are widespread both in a research scale and in the market. Cu₂O/ZnO heterostructures are generally synthesized by reactive magnetron sputtering or ALD. A novel approach consists in adding an ALD layer of the p-type material between two thin films deposited by sputtering. The sample is described in *paragraph 2.1.2.1*, and its electrical characterization is discussed in the next pages.

When the contacts are on Cu₂O and ITO, a rectifying behavior is observed. The sample is then illuminated by 1 Sun irradiation (standard air mass 1.5 global, AM 1.5G, 1000 W/m²) on an area of 0.16 cm². Although the illuminated area is not all covered by Cu₂O PVD, the sample shows a good photovoltaic response at 0 V, as depicted in *Figure 3.17*. The current density in the y-axis of the J-V curves is the ratio between the measured current and the illuminated area. The V_{OC} and J_{SC} are 320 mV and 0.8 μA/cm², respectively. The dynamic response of the J_{SC} and V_{OC} is reported in *Figure 3.18* during 10 s dark/light cycles. The sample show enhanced response and recovery times to the light illumination (< 0.09s, which is the upper limit due to the response time of the Keithley). The response time is defined as the time needed to reach 90% of maximum intensity, while the recovery time is the period required to recover the initial intensity within 10%.

Lastly, the photoresponsivity to visible light (current density/incident power density) is about 8 μA/W. The enhanced photoresponse might be due to the Cu₂O amorphous layer deposited using ALD, which acts as a blocking layer, helping charge separation and preventing the charge recombination.

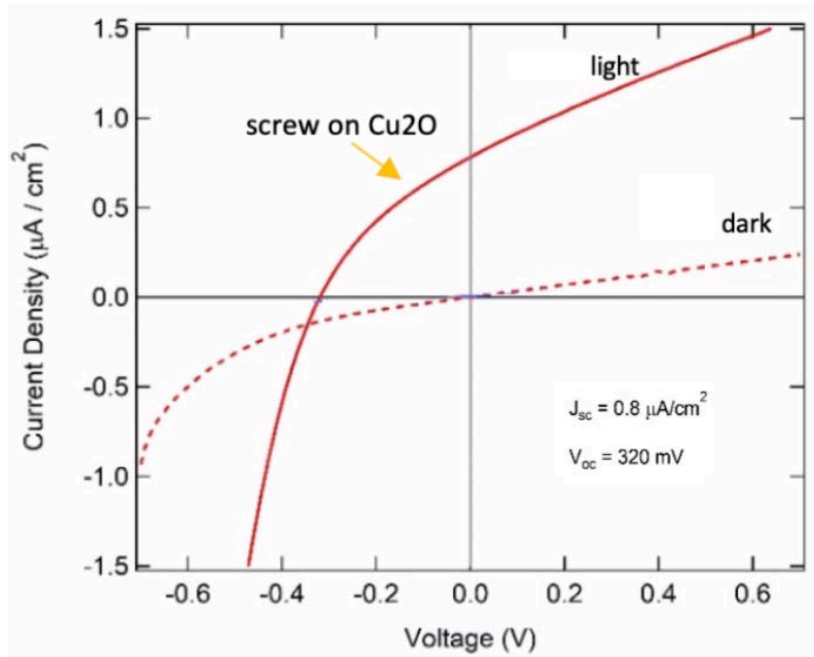


Figure 3.17 Dark and light J-V curves for Cu₂O/ZTF.

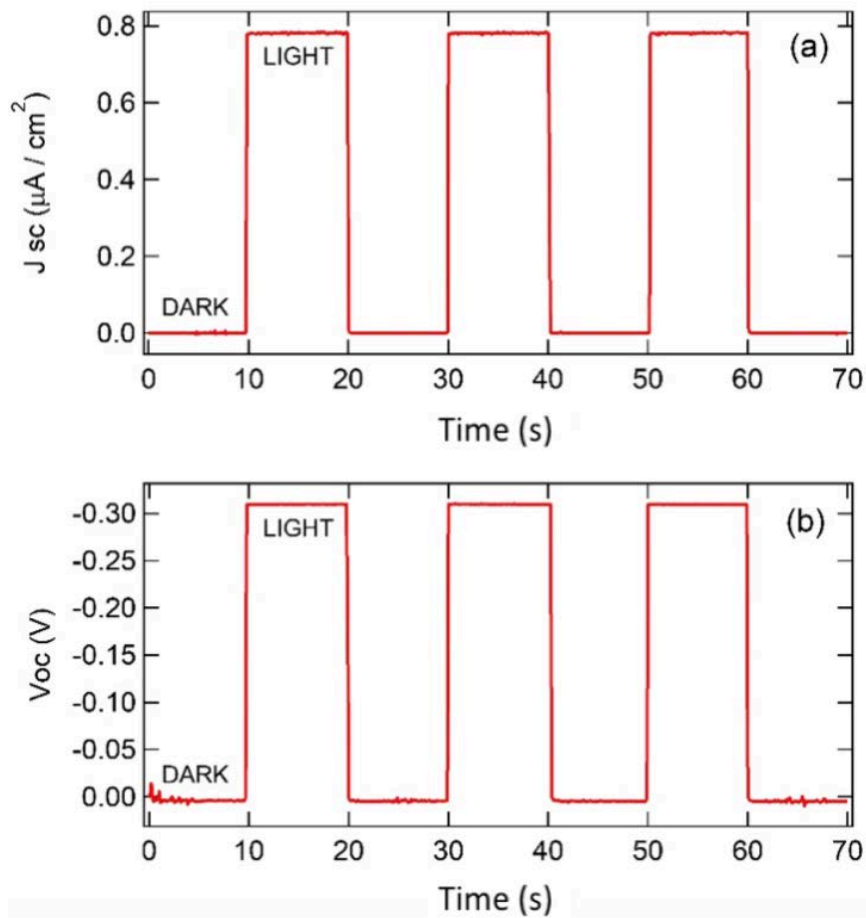


Figure 3.18 a) Dynamic response of the J_{sc} ; b) Dynamic response of the V_{oc} .

After the macro-electrical measurements, the sample was characterized by C-AFM. Once again, the conductive tip is a DCP20, which guarantees high stability and reliable results. The specimen is mounted in a sample holder, and the metallic clamp is in contact with the ITO substrate. The voltage is applied on the substrate, while the tip is grounded. Local I-V curves were taken on each layer of the sample (Cu₂O PVD, Cu₂O ALD, ZnO PVD, and ITO). Firstly, *Figure 3.19* gives the force applied to the sample by the tip. *Figure 3.19* refers to the ITO substrate, but it can be taken as reference also for the other layers. According to (2.1) and depending on the set-point, the forces are calculated and reported in *Table 3.3*. As long as the set-point is below 0.4, the involved forces remain sufficiently small, and no further effects affect the measurements. ITO has a linear ohmic behavior, and the ZnO layer shows a rectifying curve, which can arise either from the ohmic contact with the DCP20 or from the junction with FTO. As far as the Cu₂O layers are concerned, it is not possible to observe the rectifying behavior of the p-n junction, previously noticed in the macro-measurements. However, the I-V curves confirm the benefit of the ALD layer, which allows a higher current flow when a voltage is applied to the sample (orange curve in *Figure 3.20*). A greater set-point leads to higher pressure on the surface, causing:

- An increase of the nano-current, which is due to a bigger contact area of the edges of the tip with the surface.
- Change of the electrical behavior, as pointed out in the I-V curves concerning the ZnO layer (*Figure 3.21*). In this case, the weak effect of the nano-junction is overcome by the high value of the force, which allows the current flow also for a positive voltage.

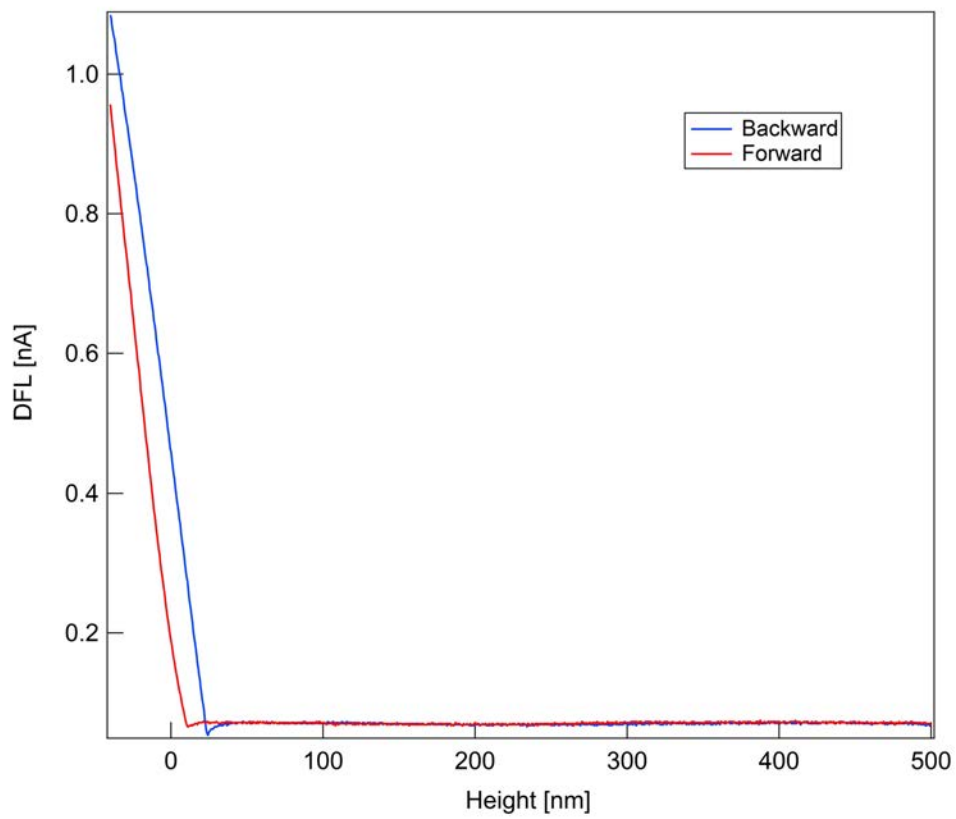


Figure 3.19 Backward and forward force curves taken on *Cu₂O/ZTF*.

Table 3.3 Forces [nN] applied on the different zones of *Cu₂O/ZTF*.

<i>ZONE</i>	<i>SP 0.1</i>	<i>SP 0.4</i>	<i>SP 0.8</i>	<i>SP 1</i>	<i>SP 1.2</i>
<i>ITO</i>	343	1371	2742	3428	4114
<i>ZnO</i>	343	1371	2742	3428	4114
<i>Cu₂O ALD</i>	282	1129	2258	2823	3388
<i>Cu₂O PVD</i>	253	1010	2020	2525	3030

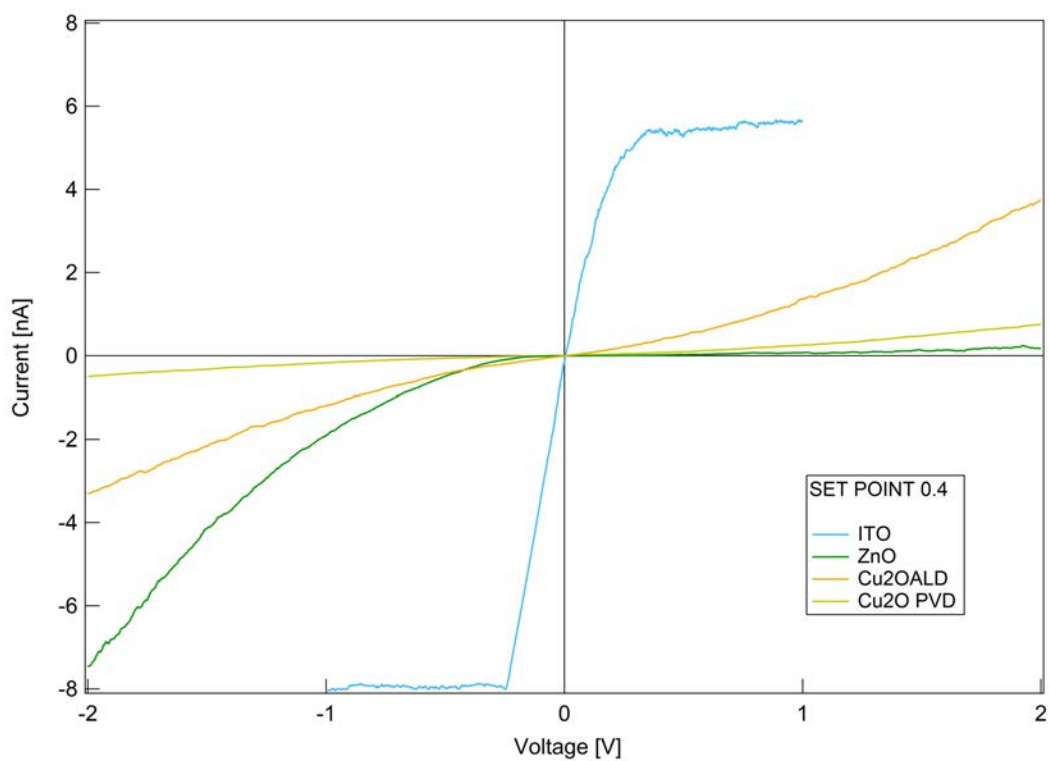


Figure 3.20 Dark I-V curves taken on different spots of Cu_2O/ZTF .

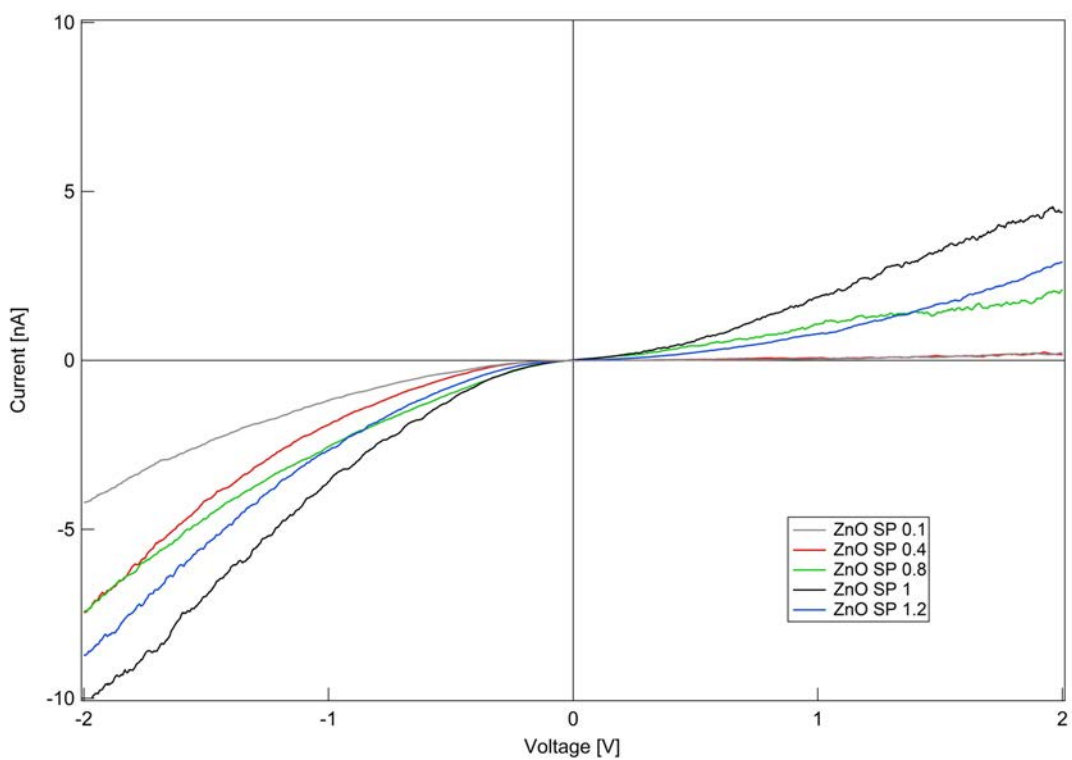


Figure 3.21 Dark I-V curves for the ZnO layer at different values of set-point.

Conductive AFM can be combined with a light source for investigating the local photo-properties. A small white LED is mounted on the sample holder, in such a way to make the light pass from the bottom of the sample (ITO) to the absorbing layers. The emission spectrum of the white LED is shown in *Figure 3.22*. Although the shape of the curves does not correspond to a diode behavior (probably due to unwanted local phenomena), a clear photovoltaic effect is observed in *Figure 3.23a* and *Figure 3.23d*. The same effect at 0 bias voltage was not noticed in the ZnO layer (*Figure 3.24*). Hence, the light response is reliable and not due to charge effects on the tip. It is possible to conclude that the Cu₂O ALD layer promotes the charge separation after the generation of electrons in the CB and holes in VB due to the light absorption.

As in the case of macro-measurements, the photoresponsivity can be studied through dark/light cycles. The I-V curves refer to the current profiles shown in *Figure 3.23b* and *Figure 3.23c*. The light effect is more evident in the ALD layer, in which the current at 0 V is 0.8 nA.

Lastly, the variation of current with time was measured by switching the light on/off during 10 s cycles. *Figure 3.25* shows that the light has a strong effect on the current when a positive voltage is applied on the sample. The same effect occurs at 0V (photovoltaic effect). Hence, enhanced response and recovery times are confirmed by the photoconductive AFM (pC-AFM).

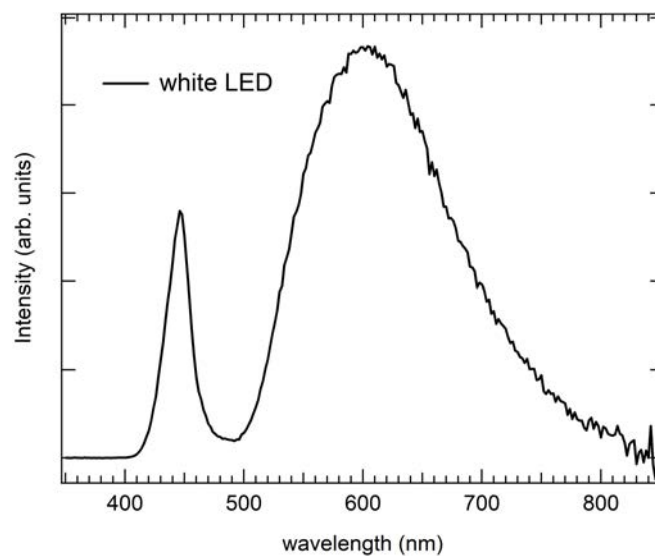


Figure 3.22 Emission spectrum of the low-intense white LED.

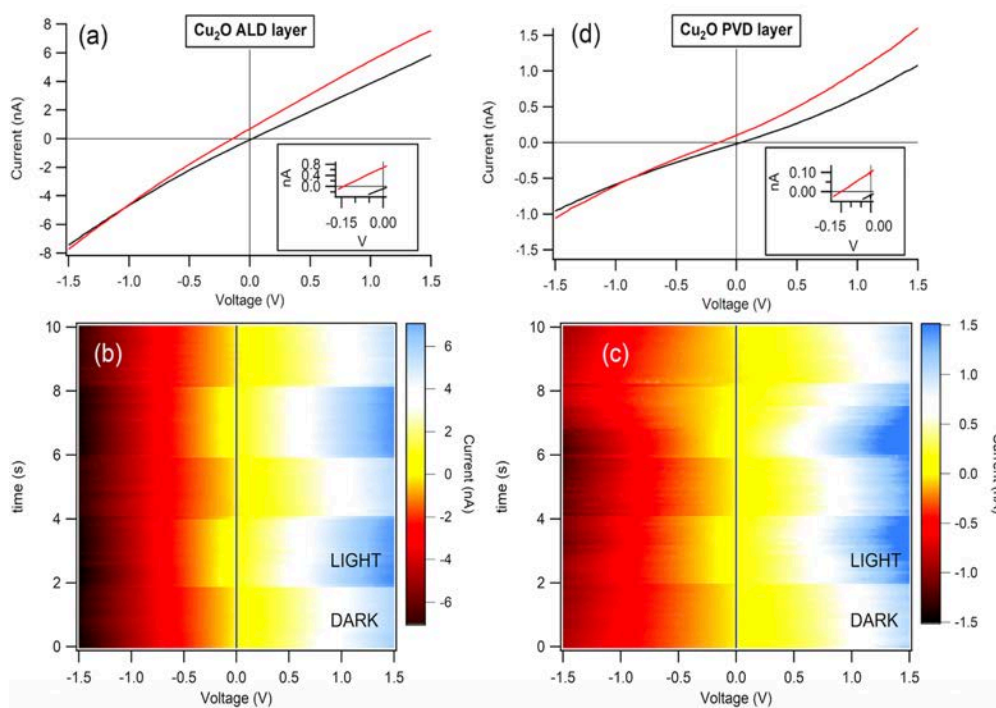


Figure 3.23 a) Local I-V curves of Cu₂O ALD layer in in dark (black line) and light (red line); b) Nanoscale photocurrent profiles of Cu₂O ALD layer from dark/light cycles c) Local I-V curves of Cu₂O PVD layer in in dark (black line) and light (red line); d) Nanoscale photocurrent profiles of Cu₂O PVD layer from dark/light cycles

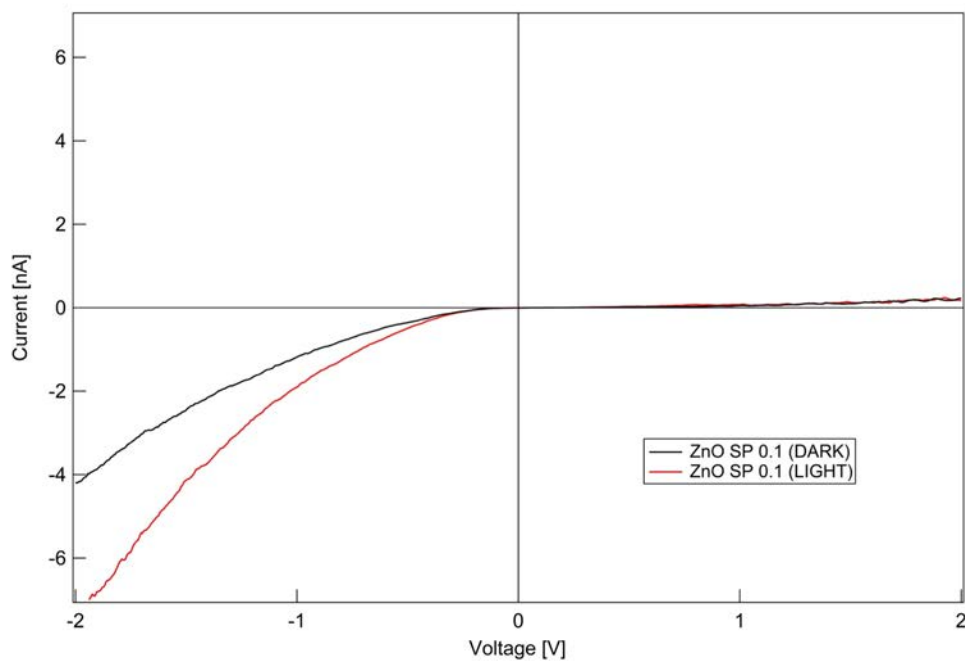


Figure 3.24 Local I-V curves of ZnO PVD layer in dark (black line) and light (red line).

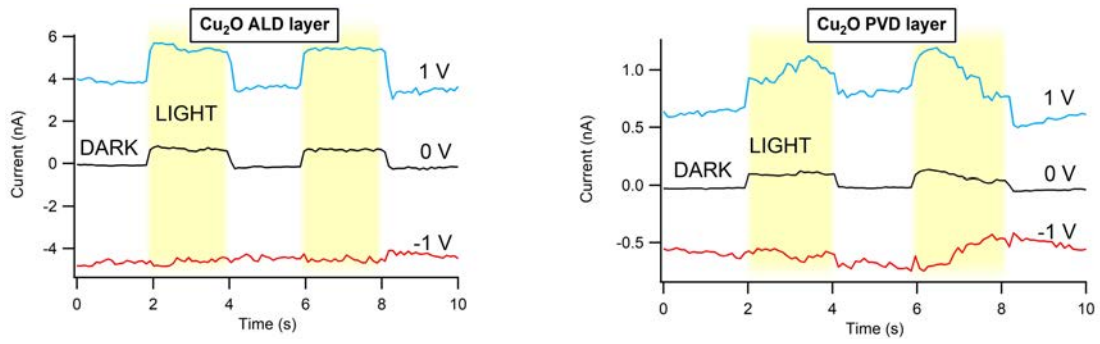


Figure 3.25 Effect of light on the current for Cu₂O ALD layer and Cu₂O PVD layer.

3.4 State-of-the-art p-n heterojunctions

Section 3.5 and *Section 3.6* represent the core of this thesis work. In the scientific literature, it is possible to find many articles concerning the application of metal oxides in the photovoltaic field. Most of them rely on Cu_2O as the absorbing layer, most likely in a thin film architecture. New perspectives are focused on other p-type oxides, such as Co_3O_4 , which can be used as the active layer thanks to its favorable energy band gap. Moreover, its electronic band structure, in terms of positioning of conduction and valence bands with respect to vacuum, matches very well the position of ZnO and TiO_2 conduction band to build-up an efficient p-n heterojunction. In this study, besides the thin film geometry, new p-n junction nanostructures based on conformal $\text{ZnO-Co}_3\text{O}_4$ and $\text{TiO}_2\text{-Co}_3\text{O}_4$ core-shell nanowires system are proposed.

3.5 Co₃O₄/ZnO heterostructures

3.5.1 Optical properties

3.5.1.1 Transmittance

Figure 3.26 and *Figure 3.27* show the optical transmittance of the five samples, before and after the deposition of cobalt oxide. All the spectra are collected in the spectral interval 350-750 nm. The transmission of the ZnO thin films (250 and 500 nm) results around 70-80% for wavelengths greater than the absorption edge. As can be observed in *Figure 3.26*, the light transmitted through the sample decreases when the thickness of the ZnO layer increases. On the contrary, ZnO NWs show a much lower transmission, in particular for low wavelengths. When a layer of ZnO covered the NWs (blue and red lines), the optical transmittance is further reduced.

As expected, the transmittance of the samples after the cobalt oxide deposition is lower than the n-type material, thanks to the absorption of Co₃O₄ in the UV-vis-NIR range. The transmittance of the coated ZnO NWs is then reduced to 20%, whereas no transmittance is recorded for $\lambda < 600$ nm in the bare ZnO NWs/Co₃O₄ sample.

3.5.1.2 Reflectance

Regardless of their thickness, ZnO thin films show very low reflectance signal. On the other hand, the NWs configuration promotes the scattering of the light, confirmed by the high diffuse reflectance (yellow curve in *Figure 3.28*). In the bare Zn NWs, the peak of reflectance ($R = 14\%$) is observed at 390 nm. The value for higher energy decays to zero, indicating that all this portion of spectrum must be absorbed. When they are coated (blue and red curves in *Figure 3.28*), the maximum intensity is shifted towards lower wavelengths.

As a consequence of the cobalt oxide deposition by ALD, the reflectance of the pristine Zn NWs considerably decreases (*Figure 3.29*). A reflectance reduction does not occur in the other samples, in which its value remains slightly the same.

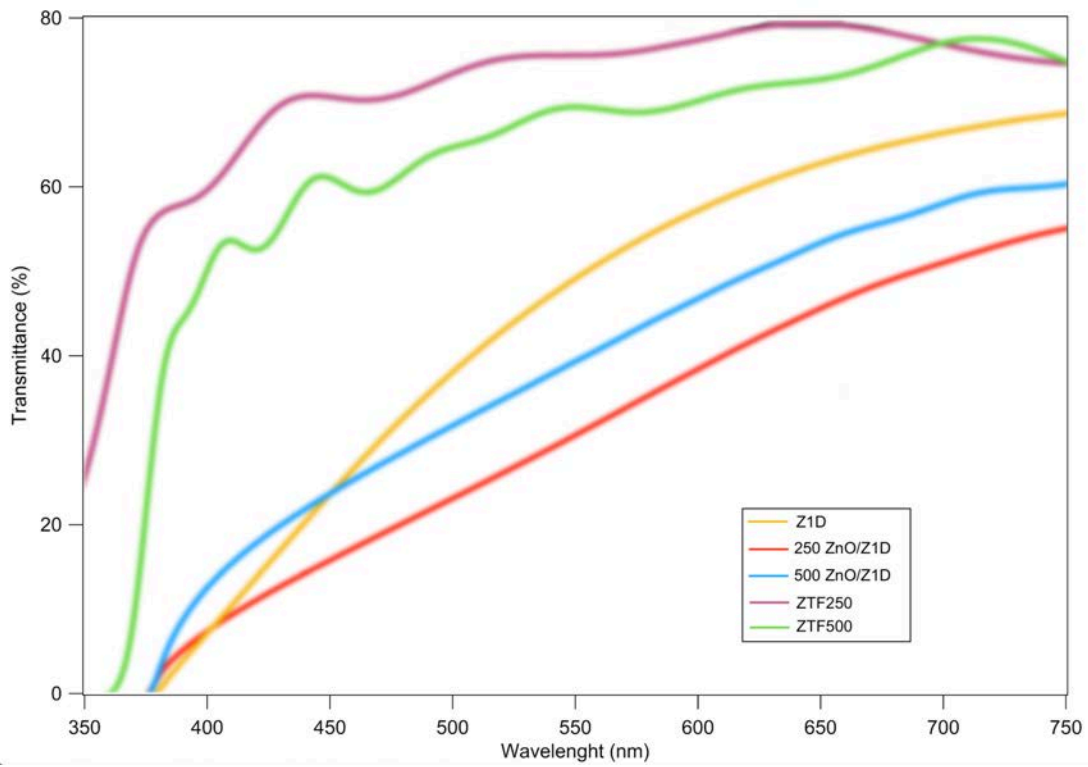


Figure 3.26 Transmittance spectra of ZnO samples before the deposition of Co₃O₄.

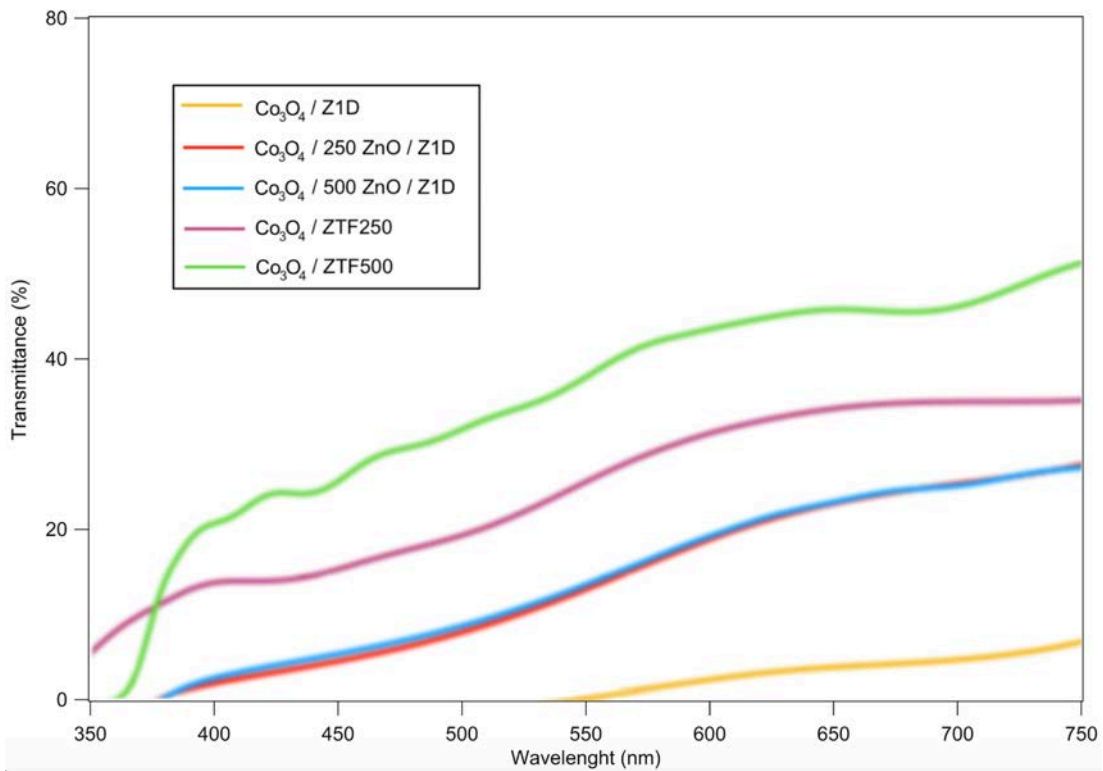


Figure 3.27 Transmittance spectra of ZnO samples after the deposition of Co₃O₄.

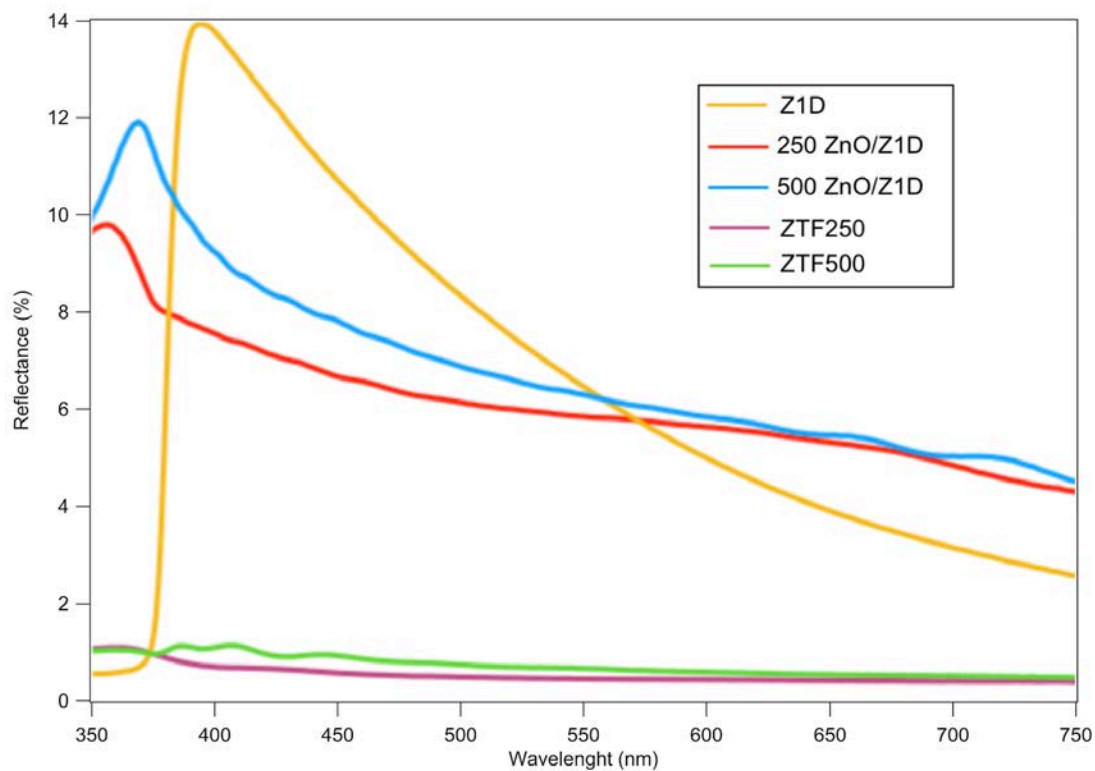


Figure 3.28 Reflectance spectra of ZnO samples before the deposition of Co_3O_4 .

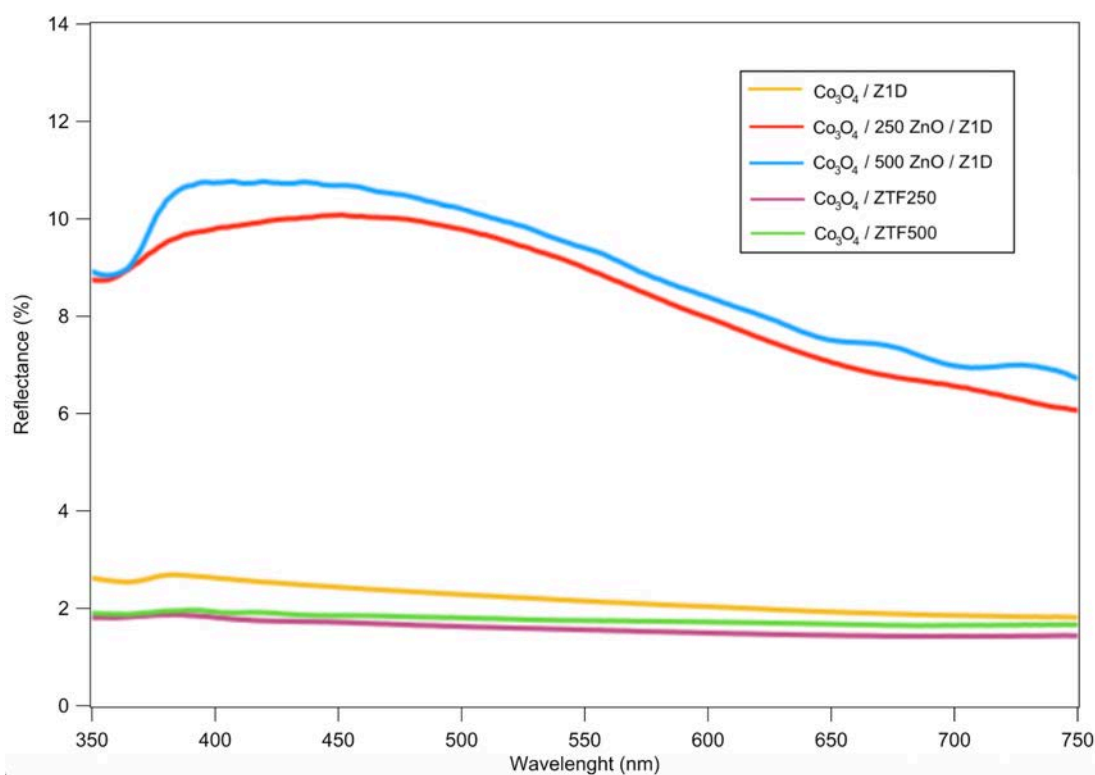


Figure 3.29 Reflectance spectra of ZnO samples after the deposition of Co_3O_4 .

3.5.1.3 Photoluminescence

Photoluminescence (PL) of the samples was performed using an excitation wavelength $\lambda_{\text{exc}} = 270$ nm. In the bare ZnO NWs sample (green curve in Figure 3.30), the peak at 377 nm is attributed to the near band edge emission (NBE), which is caused by direct recombination of excitons through an exciton-exciton collision process. The same peak is present when a ZnO layer covers the NWs. The second broad peak in the visible range ($\lambda_{\text{peak}} = 600$ nm) is called deep level emission (DLE) and is related to ZnO surface defects in the crystalline structure. The presence of these impurities (e.g., oxygen vacancies or interstitial) creates trap levels within the energy band gap. As depicted in Figure 3.30, ZnO thin films have fewer defects than their 1D counterparts. The emission peak centered at 600 nm disappears when the NWs are coated by the ZnO layer. The effect of the presence of Co₃O₄ on top of ZnO results in a decreased emission intensity (Figure 3.31), for both the emission bands.

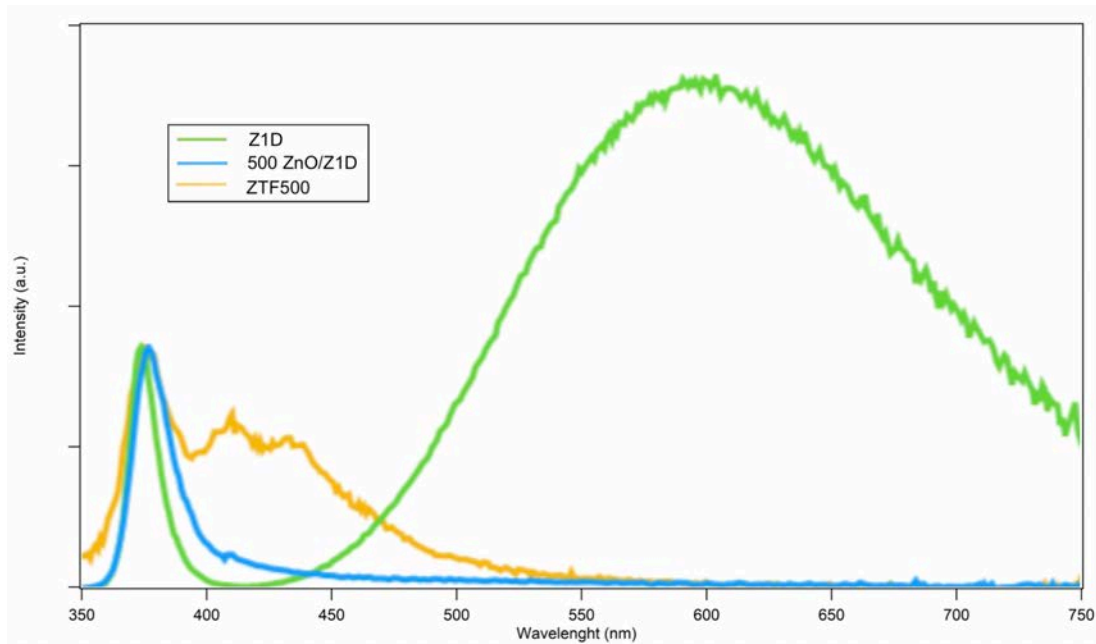


Figure 3.30 Photoluminescence spectra of ZnO samples (bare NWs and 500 nm thin film) before the deposition of Co₃O₄.

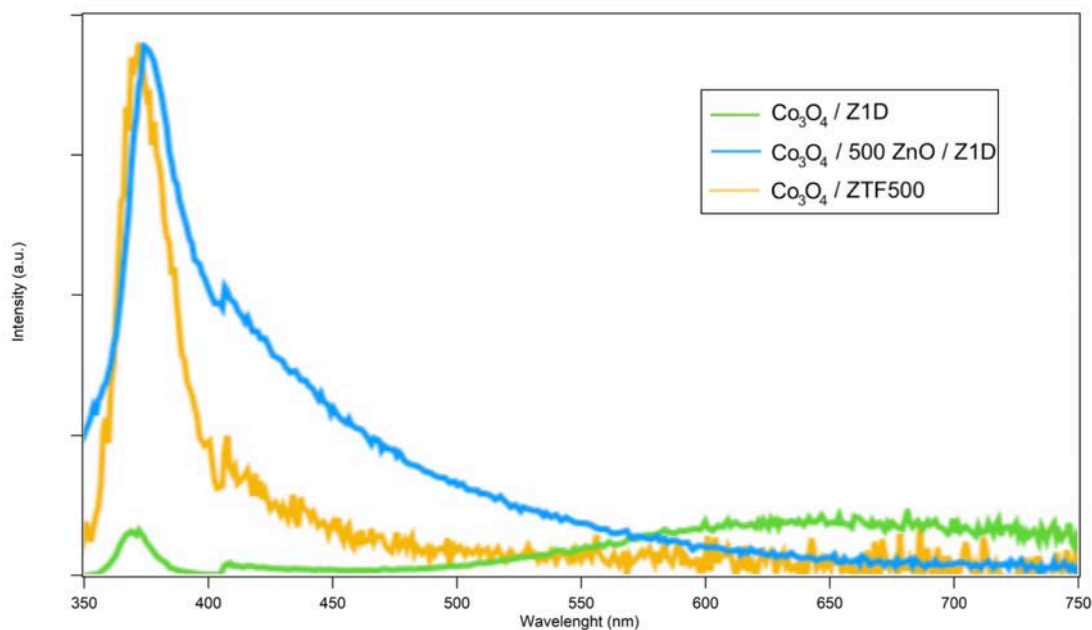


Figure 3.31 Photoluminescence spectra of ZnO samples (bare NWs and 500 nm thin film) after the deposition of Co_3O_4 .

3.5.2 Morphological and structural characterization

The morphology of the samples was studied through SEM and AFM images. In this paragraph, only the former is shown, while the latter is discussed afterward, together with the electrical behavior at the nanoscale. SEM images were collected both in planar and cross-sectional view. As can be observed in *Figure 3.32a*, bare ZnO NWs have a hexagonal shape, with an average diameter in the range of 40-50 nm. When covered by 250 or 500 nm of ZnO, their cross sections increase, and the surface appears smooth (*Figure 3.32b*). The general distribution of the nanowires can be analyzed from a low magnification view while more details, like the hexagonal cross section typical of the wurtzite structure, require higher magnification. The SEM images of the cross section after the Co_3O_4 deposition are reported in *Figure 3.32c*. Bare ZnO NWs covered by 100 nm of Co_3O_4 show an average diameter of 128.4 nm, and it is possible to notice a core-shell structure, in which the Co_3O_4 layer forms a quite conformal shell on top of the ZnO NWs. However, as depicted in *Figure 3.32d*, part of the Co_3O_4 passed through the NW array, covering the initial seed layer. This fact can justify the unexpected electrical behavior of these heterostructures.

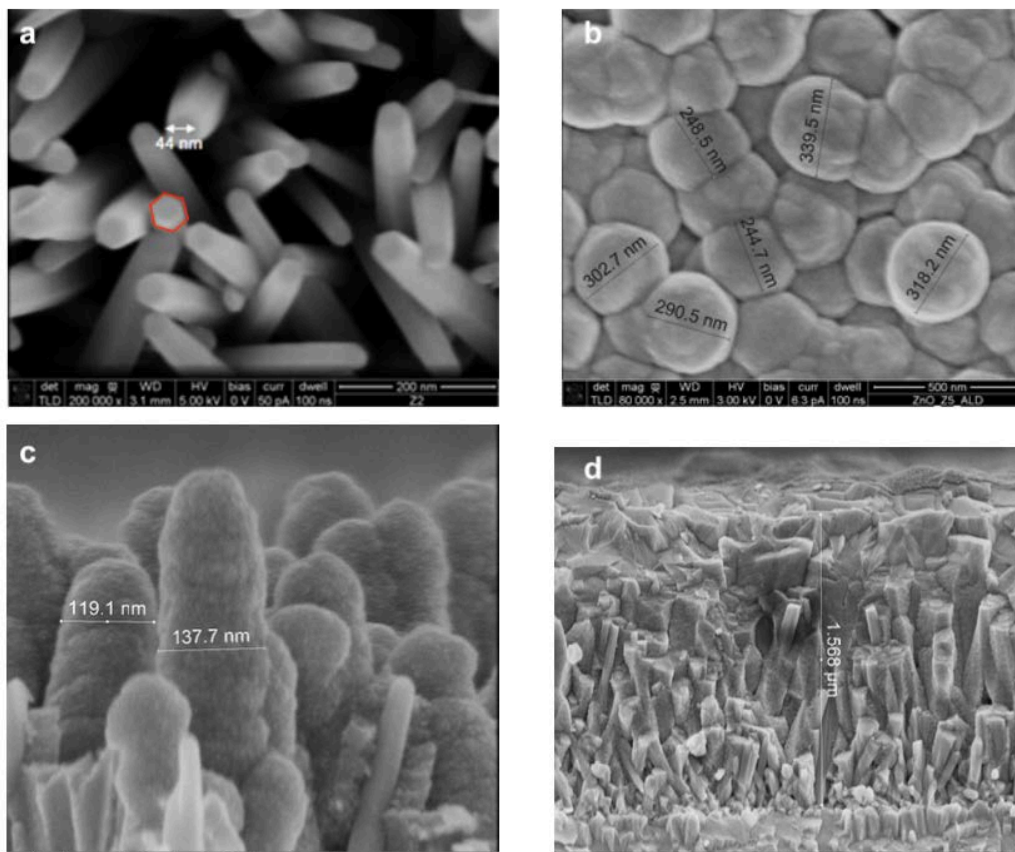


Figure 3.32 SEM images of the plane view of (a) ZID; b) 500ZnO/ZID, and the cross-section of c) and d) Co₃O₄/ZID.

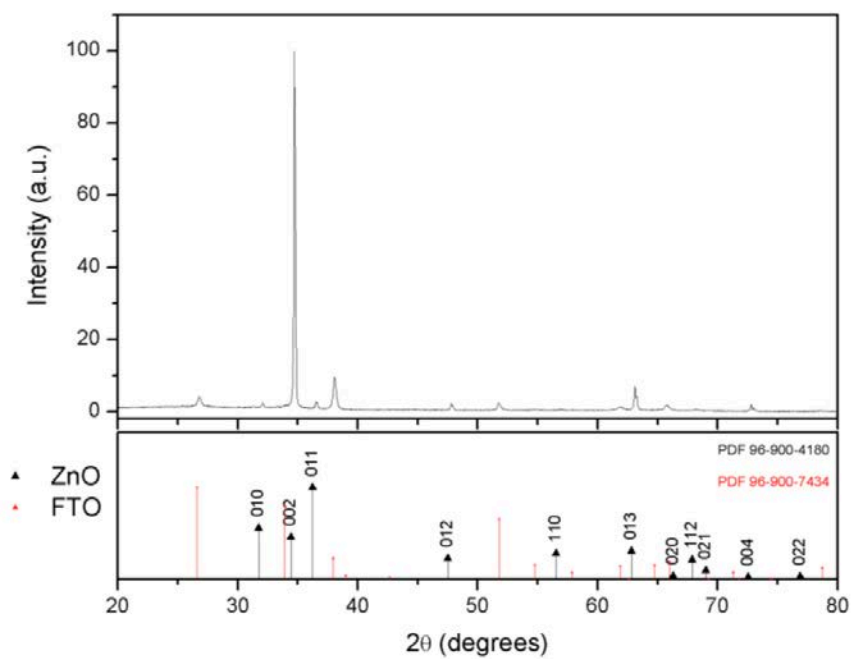


Figure 3.33 XRD patterns of bare ZnO NWs.

XRD analysis was applied to ZnO NWs before any ALD depositions to analyze their crystalline structure (which is expected to be wurtzite, according to the literature). The resulting XRD pattern (*Figure 3.33*) is compared with existing data about wurtzite structure for ZnO and cassiterite phase, typical of FTO film. All the peaks correspond either to cassiterite (Ref. code 96-900-7434) of FTO or wurtzite hexagonal phase (Ref. code 96-900-4180) of ZnO. The highest relative intensity refers to reflections from the (002) crystallographic plane. This peculiarity confirms the growth of the nanowires in a single crystalline arrangement, following a preferred orientation (c-axis of the hexagonal wurtzite structure).

3.5.3 AFM analysis: local morphology and electrical behavior

3.5.3.1 Bare ZnO nanowires

C-AFM is used to measure topography and current distribution simultaneously at the nanoscale. A small LED can shine the sample from the bottom, while the grounded tip scans the surface of the NWs (see the sketch in *Figure 3.34*). The voltage is applied on the FTO substrate, and a current distribution at fixed bias is recorded (Scanning Spreading Resistance Microscopy, SSRM). Once again, the first graph (*Figure 3.35*) is a force curve: given the initial set-point (0.5), the force applied is roughly 1100 nN.

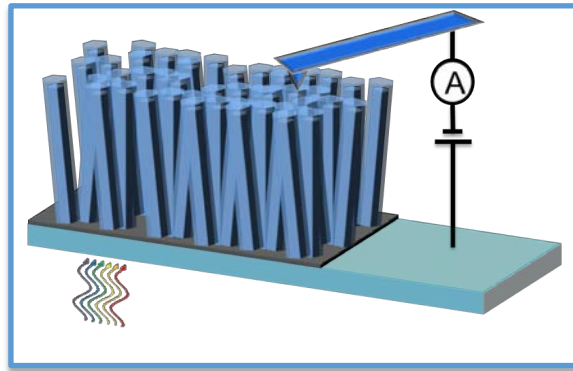


Figure 3.34 Sketch of the ZnO NWs and C-AFM set-up (light from the bottom).

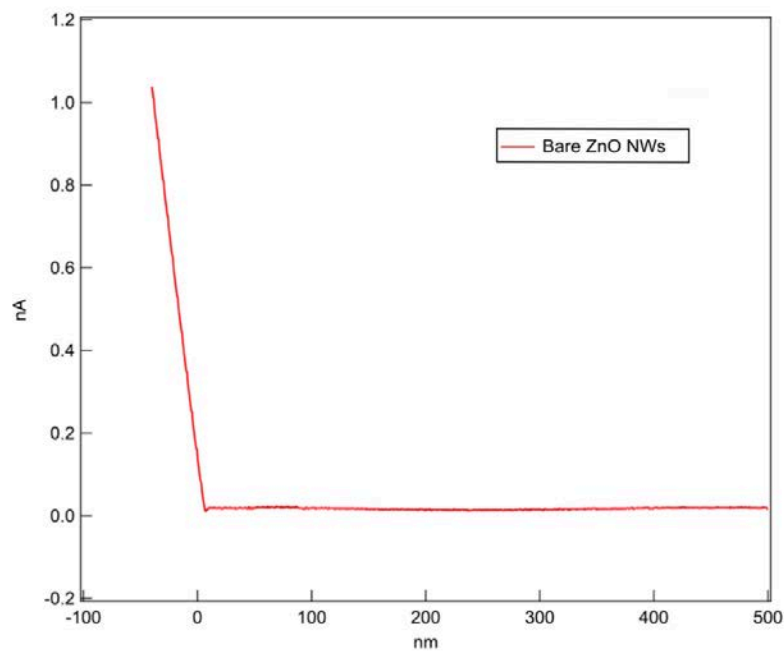


Figure 3.35 Force curve on bare ZnO NWs.

The morphology of the sample and the current distribution at -1 V are shown in *Figure 3.36*. The topography (*Figure 3.36a*) has poor quality due to continuous tip-sample contact that produces high frictional force. Moreover, different heights of the NWs can reduce the accuracy of the acquired measurement. There is a strong link between the current image and the morphology of the sample: the conductivity follows the shape of the nanowires, with high nano-current at the edges (darkest zone in *Figure 3.36b*). Local I-V (*Figure 3.37*) curves were taken on conductive spots of the sample. In dark, the Schottky junction between the metal probe and the nanowires leads to a rectifying behavior. When the NWs are illuminated, they become more conductive for both negative (forward bias) and positive (reverse bias) voltages. However, no photovoltaic effect is measured at 0 V. These results are consistent with those concerning the ZnO NWs, already discussed in the previous paragraphs.

The same measurements were repeated after the deposition of Co_3O_4 by ALD. The morphology (*Figure 3.38*) was taken together with two electrical images at -2 V (*Figure 3.39a*) and 2 V (*Figure 3.39b*). The first result is that some ZnO nanowires are not conductive and they do not form a p-n junction with cobalt oxide. The I-V curves are taken by sweeping the voltage between -2 V and 2V. *Figure 3.40* refers to a “working” p-n junction, which allows current only at negative voltages. No light effect is observed in the reverse bias, while the current slightly increases in the forward region.

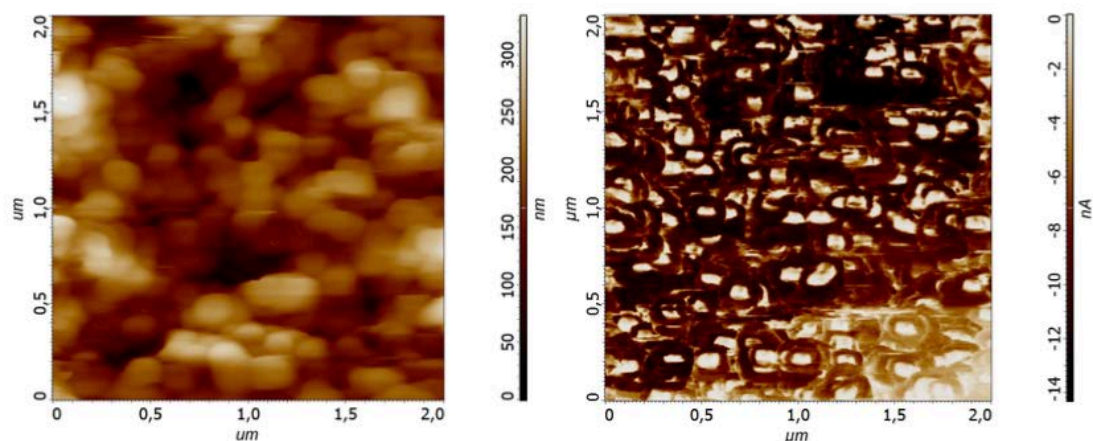


Figure 3.36 a) AFM surface morphology of ZID; b) Local current map of ZID collected with C-AFM by applying -1V.

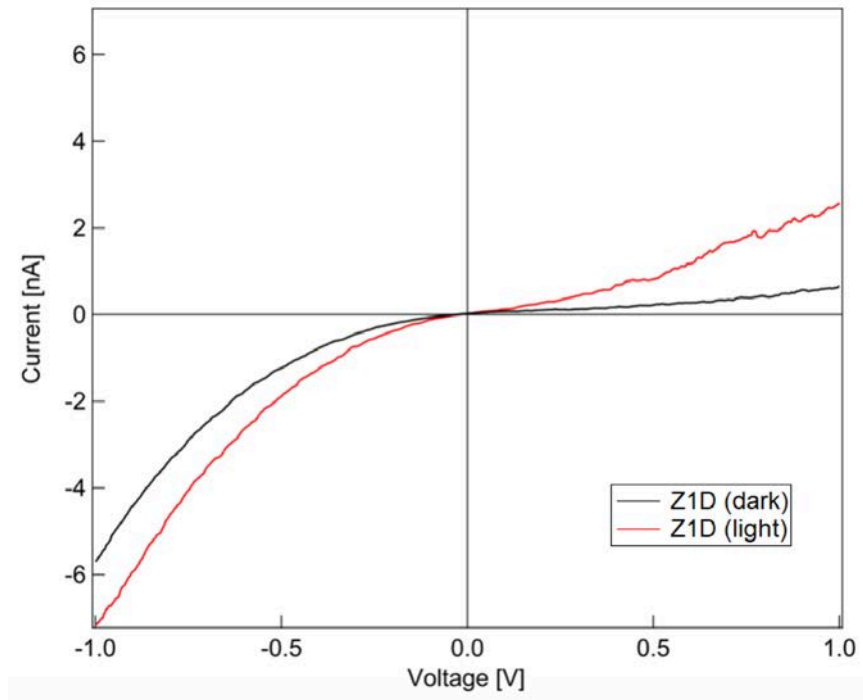


Figure 3.37 Average of 10 I-V curve in dark (black line) and light (red line) for Z1D.

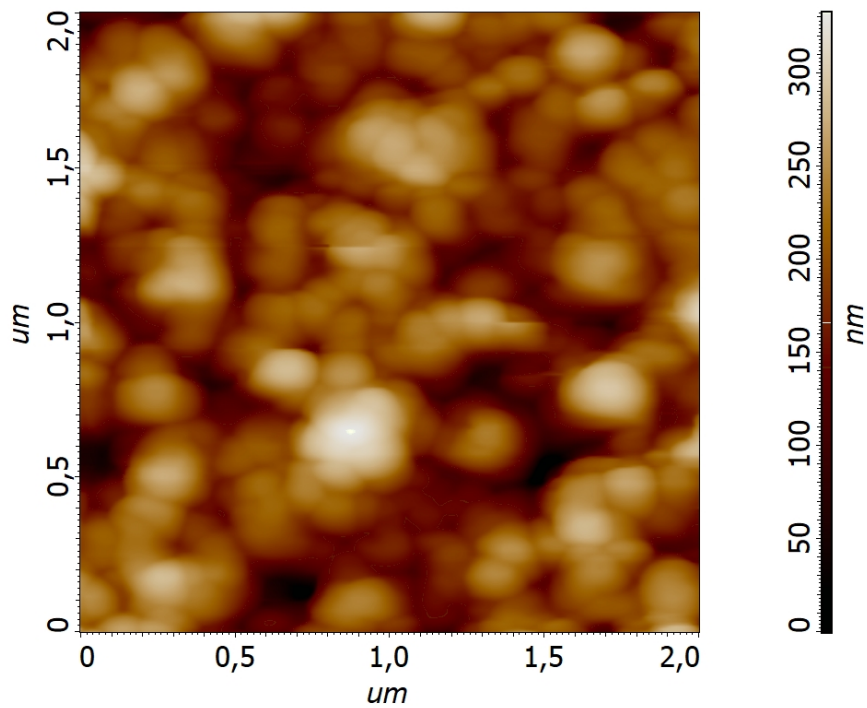


Figure 3.38 AFM surface morphology of Co₃O₄/Z1D.

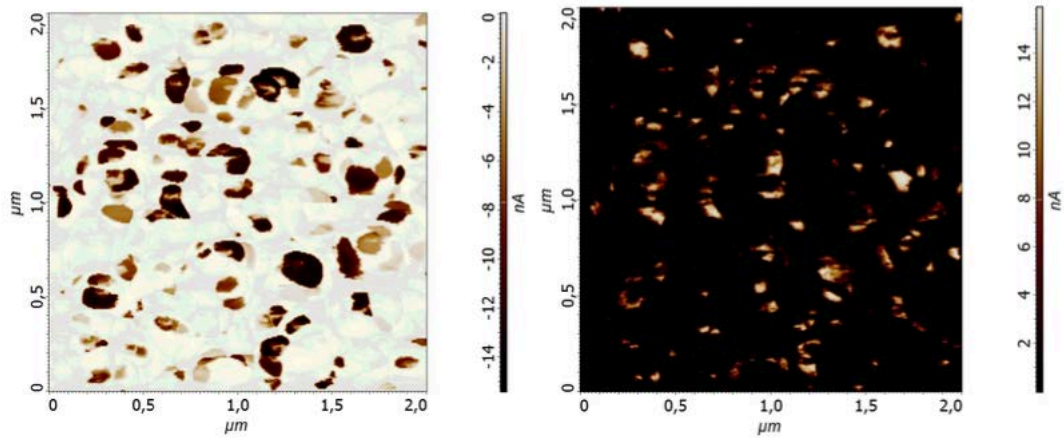


Figure 3.39 Local electrical image of $Co_3O_4/Z1D$ a) $BV = -2V$; b) $BV = +2V$.

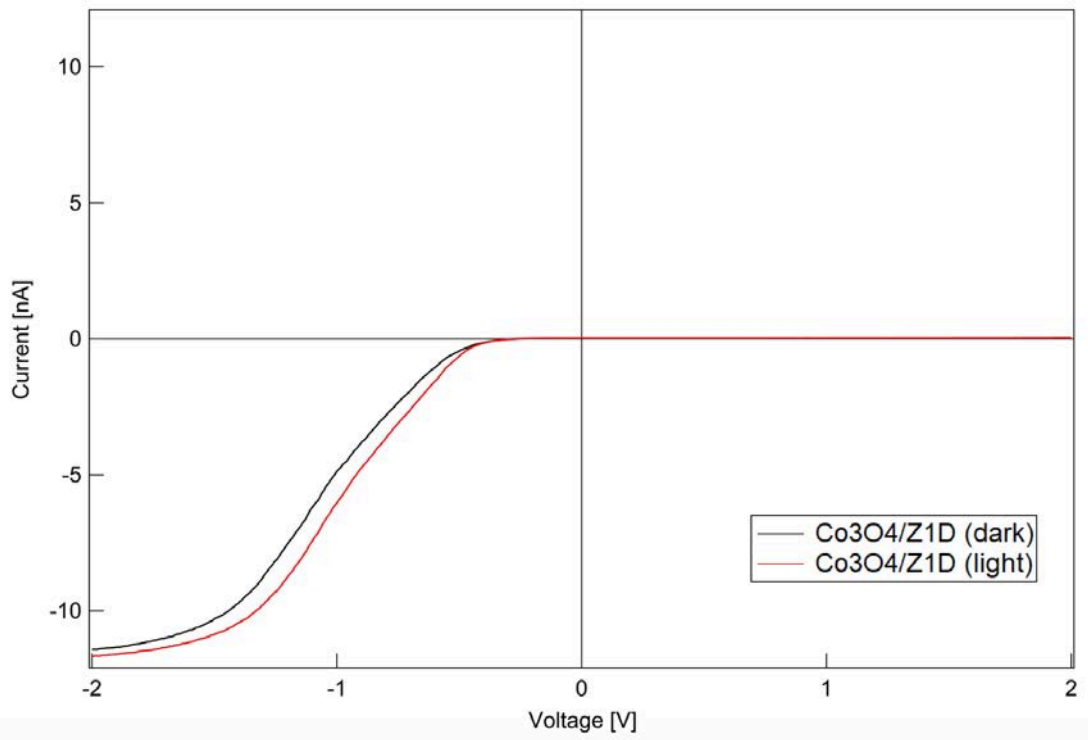


Figure 3.40 Average of 10 I-V curve in dark (black line) and light (red line) for $Co_3O_4/Z1D$.

3.5.3.2 ZnO thin film on top of ZnO NWs

The best results from the C-AFM are relative to ZnO NWs coated with 250 nm of ZnO. The size of the NWs (*Figure 3.41*) is consistent with the SEM images discussed in *subsection 3.5.2*. The sample shows really high current, even with a low applied voltage. When the I-V curves were taken under illumination, a small photovoltaic effect is observed (*Figure 3.42*). Both the presence of the extra layer of ZnO above the NWs and its dimension is important. The same effect is indeed not noticed neither in the bare configuration nor when the layer has a thickness of 500 nm. The further deposition of the p-type oxide (Co₃O₄) does not change the morphology of the sample (*Figure 3.43*). Conformal ZnO-Co₃O₄ core-shell nanowires with a diameter of about 200-300 nm are obtained. However, the p-n junction does not show a rectifying behavior at the nanoscale, and, unlike the bare ZnO NWs, the deposition of Co₃O₄ causes a substantial reduction of the current (*Figure 3.44*). No light effect is then observed in the sample. Similar results are achieved when the thickness of ZnO is 500 nm. The only differences regard the I-V curves in dark (*Figure 3.45*), which are more rectifying, and the absence of the light effect at 0 V.

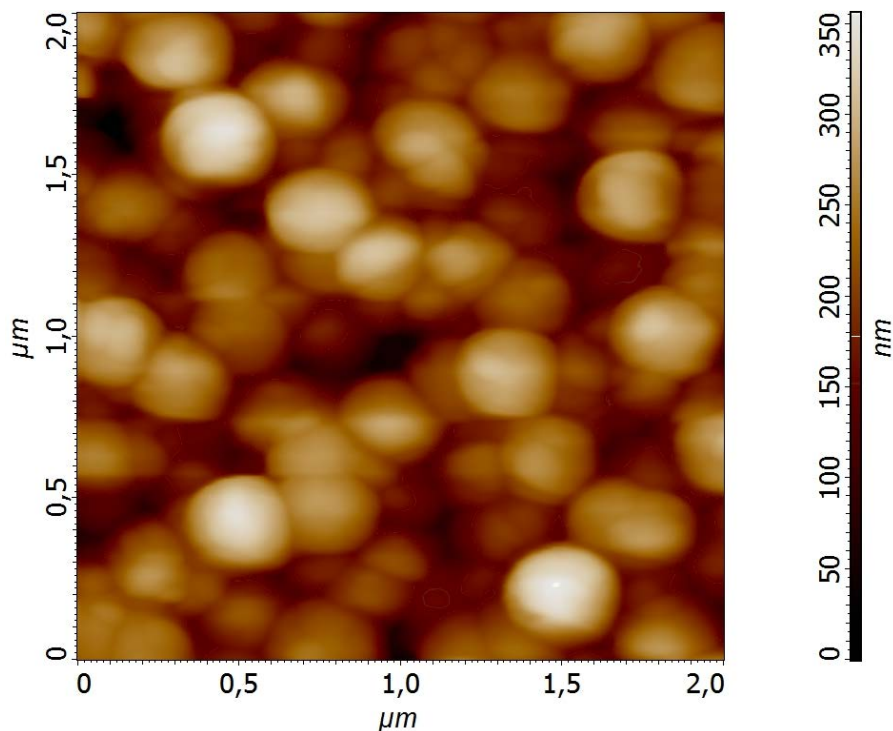


Figure 3.41 AFM surface morphology of 250ZnO/Z1D.

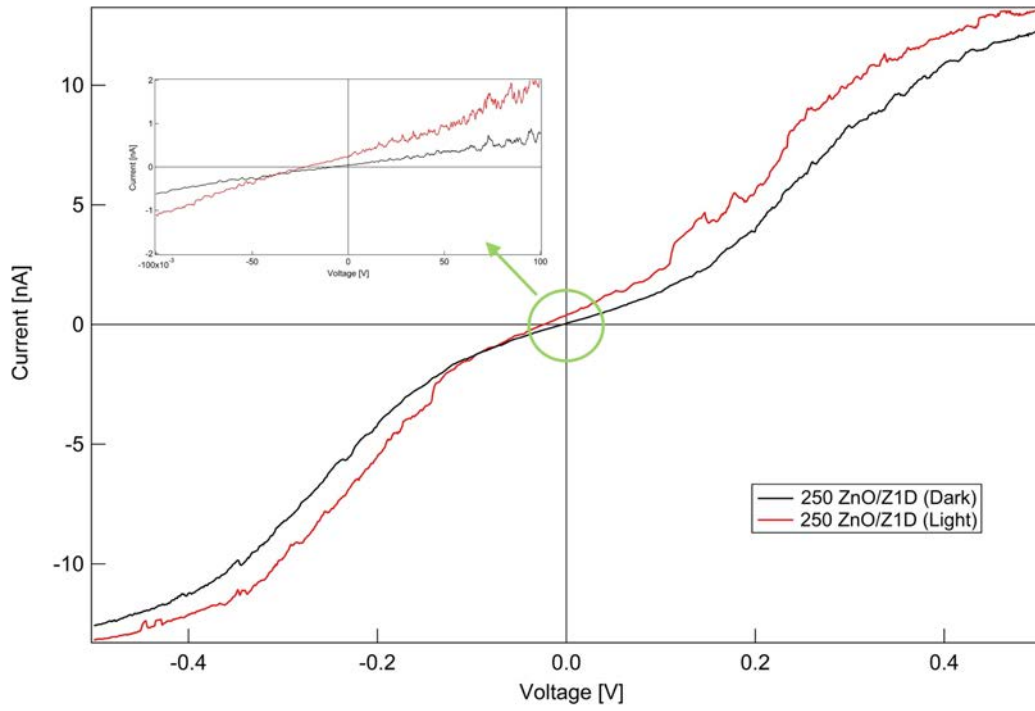


Figure 3.42 Average of 10 I-V curve in dark (black line) and light (red line) for 250ZnO/Z1D.

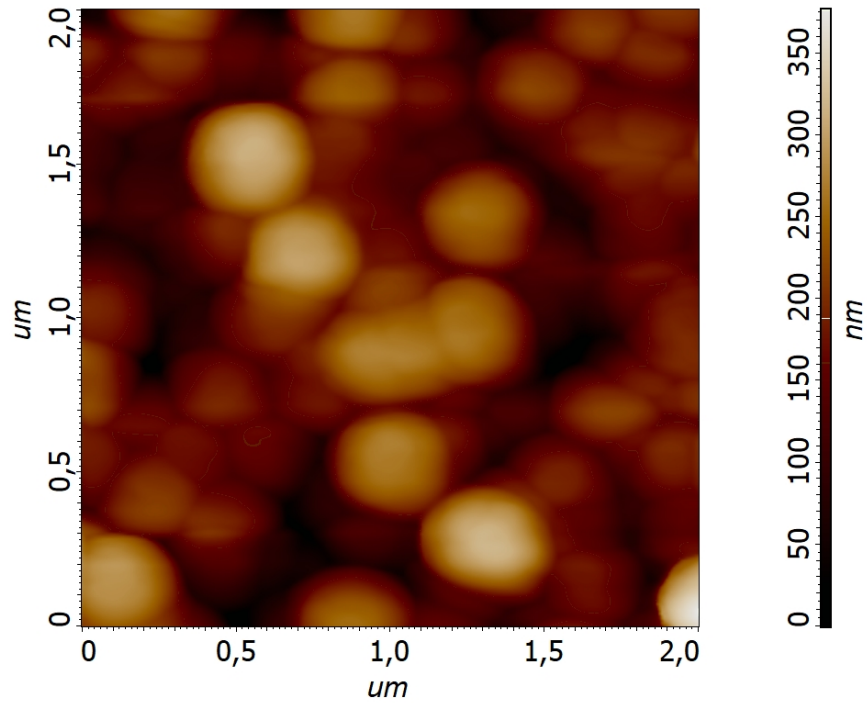


Figure 3.43 AFM surface morphology of Co₃O₄/250ZnO/Z1D.

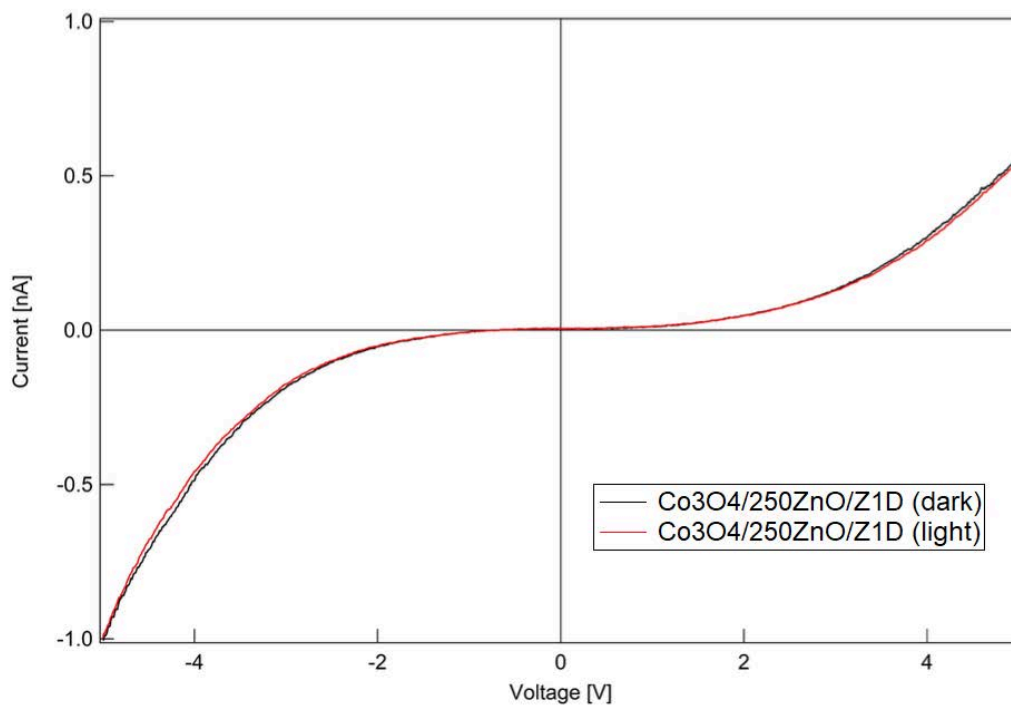


Figure 3.44 Average of 10 I-V curve in dark (black line) and light (red line) for Co₃O₄/250ZnO/Z1D.

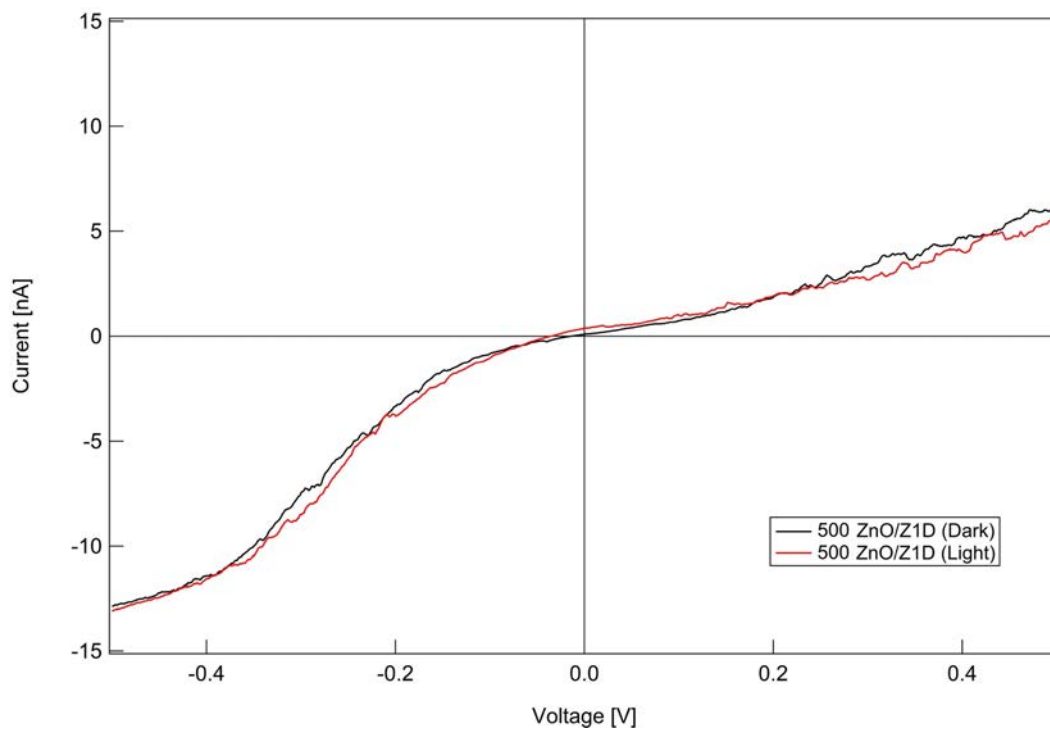


Figure 3.45 Average of 10 I-V curve in dark (black line) and light (red line) for 500ZnO/Z1D.

3.5.3.3 ZnO thin film

AFM surface images of ZnO thin film look like *Figure 3.46*. The morphology is mainly formed by small granular structures, which must not be confused with the circular shape of the nanowires. As a matter of fact, the y-axis scale reveals a smoother surface in the thin film morphology, with a maximum height of about 50 nm. A SSRM was made on the ZnO thin film and I-V curves were taken in the conductive zones. *Figure 3.47* and *Figure 3.48* are relative to two different thicknesses, 250 nm and 500 nm. Similarly to the covered ZnO NWs, 250 nm ZnO thin film show a strong response to the illumination, which overcome the weak effect of junction with the metal tip. When the thickness is 500 nm, a strong rectifying behavior is observed in the characteristic I-V curves and the light increases the current only in the forward region. Once again, the same measurements were repeated after the deposition of Co_3O_4 . A remarkable decrease of current is observed in the I-V curve depicted in *Figure 3.49*. In particular, it can be noticed that, for bias voltage lower than $\pm 2\text{V}$, the current flow among the junction is almost null.

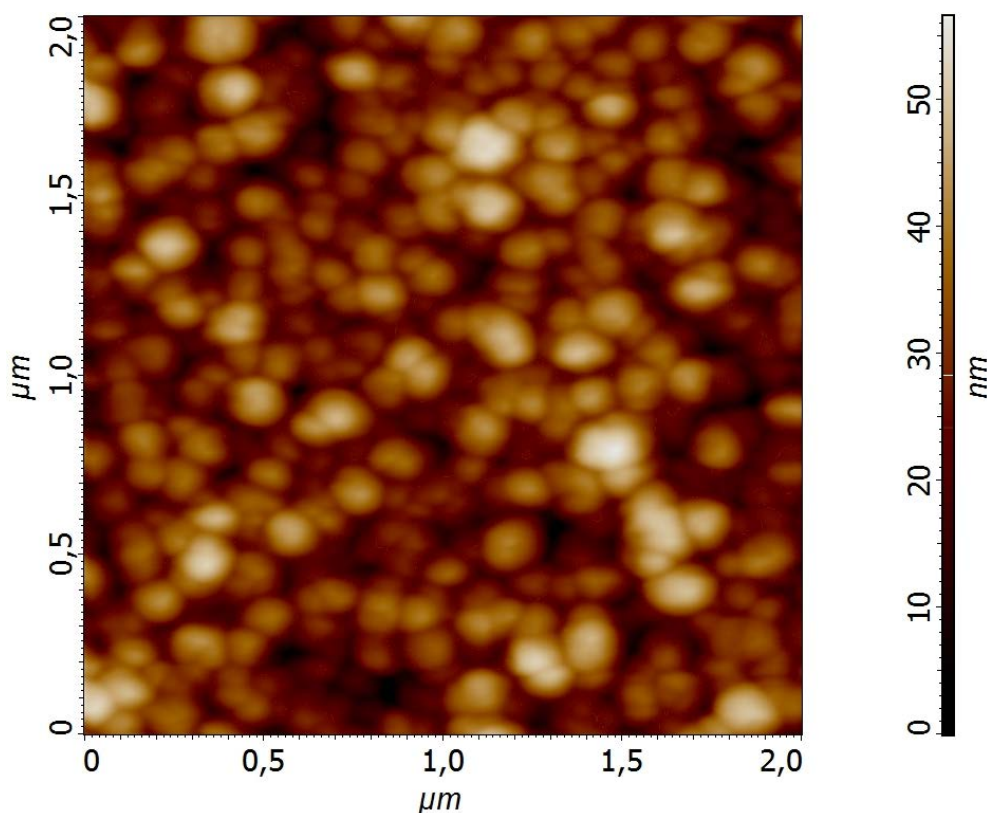


Figure 3.46 AFM surface morphology of ZTF250.

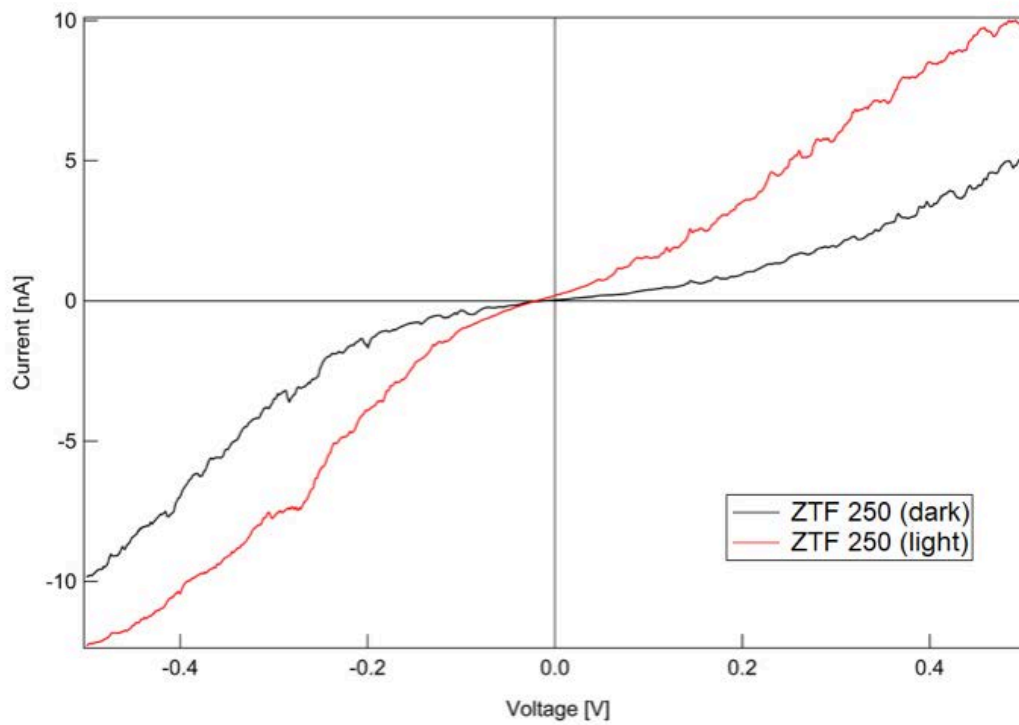


Figure 3.47 Average of 10 I-V curve in dark (black line) and light (red line) for ZTF250.

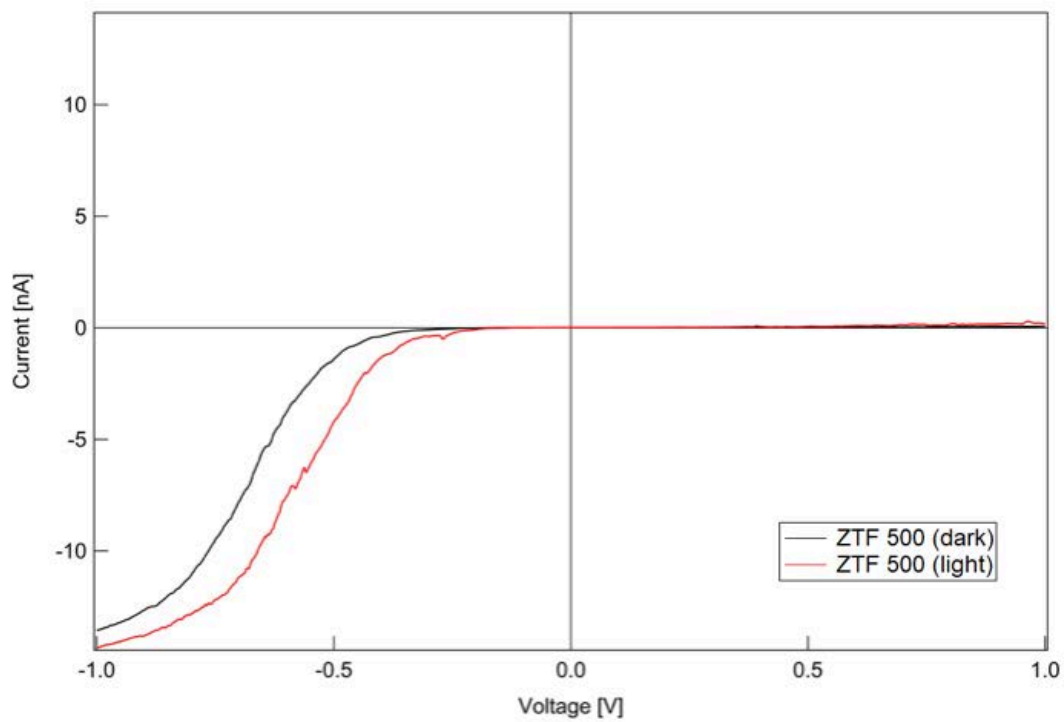


Figure 3.48 Average of 10 I-V curve in dark (black line) and light (red line) for ZTF500.

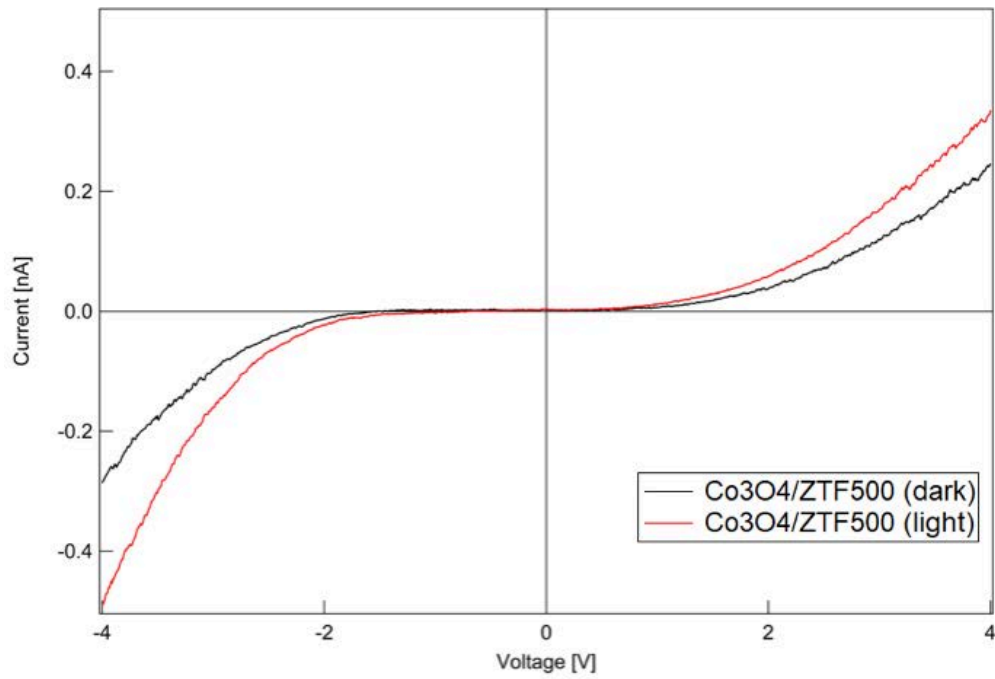


Figure 3.49 Average of 10 I-V curve in dark (black line) and light (red line) for $Co_3O_4/ZTF500$.

3.5.4 Macro electrical measurements

The electrical measurements do not show the desired results. The samples are tested both in dark and light, but the rectifying behavior of the formed p-n junction is not clear. The reason could be ascribed on technical issues during the measurements, such as too high pressures applied to the samples by the metal screws. A small light effect is pointed out only for the bare ZnO NWs, both before (*Figure 3.51*) and after (*Figure 3.52*) the deposition of Co₃O₄. The current increases in the reverse and forward bias when the light shined the sample, but no photovoltaic effect is observed at 0 V. The I-V curves concerning the other samples (coated ZnO NWs and thin films) show a linear ohmic behavior (*Figure 3.50*), with an overlap between the dark and light curves (no light effect).

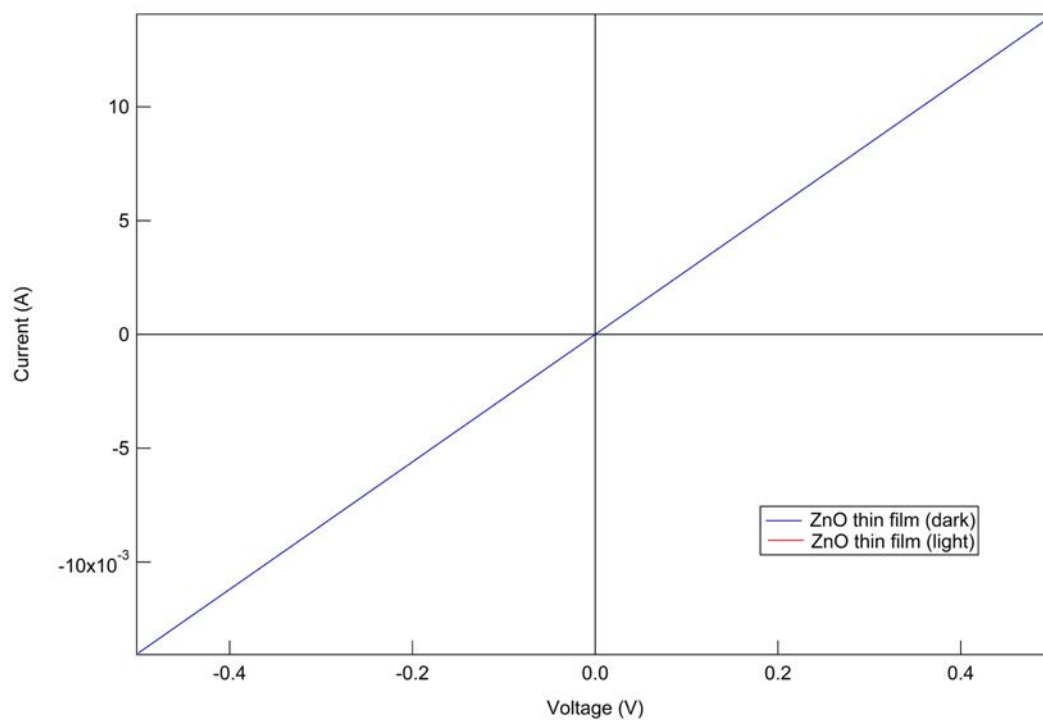


Figure 3.50 Macro I-V curves for ZTF500.

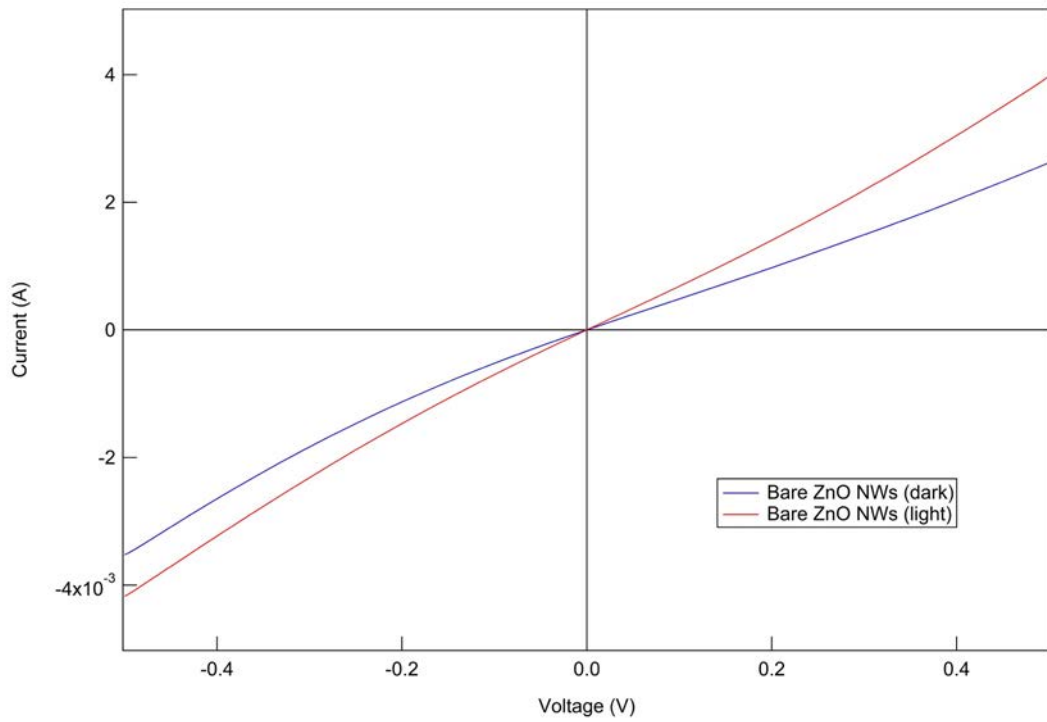


Figure 3.51 Macro I-V curves for ZrO_2/ZnO , in dark (blue line) and light (red line).

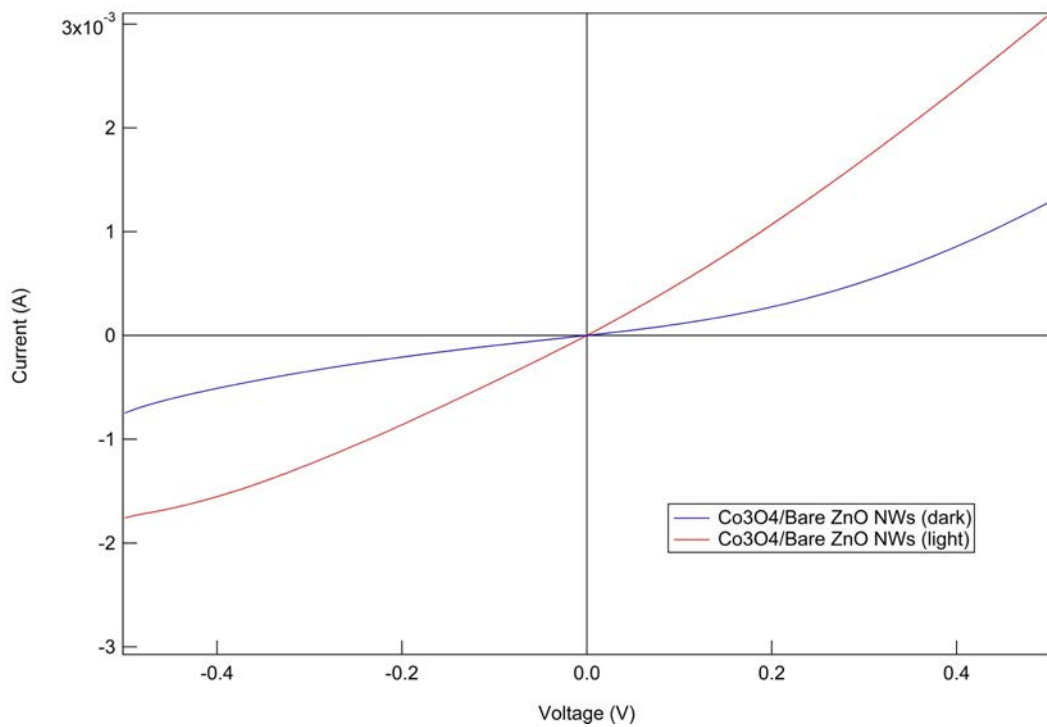


Figure 3.52 Macro I-V curves for $Co_3O_4/ZrO_2/ZnO$, in dark (blue line) and light (red line).

3.6 Co₃O₄/TiO₂ heterostructures

The second typology of novel heterostructure involves TiO₂ as n-type oxide. Solvothermal and hydrothermal techniques have been used for the synthesis of the TiO₂ nanowires, while the thin films have been deposited by ALD.

3.6.1 Morphological and structural characterization

Scanning Electron Microscopy (SEM) is used to characterize the morphology of the samples. The planar morphology of the sample obtained by the solvothermal method is shown in *Figure 3.53a*. The surface looks more like a thin film rather than nanowires, which are evident only from the picture of the cross section (*Figure 3.53c*). The forest is compacted, with each nanowire really close to the others. From the SEM images, they look like a continuous layer, having a thickness of about 4.4 μm. This sample will be called “compacted nanowires” later in this thesis. After the deposition of cobalt oxide (*Figure 3.53e*), the microstructure seems to be denser as the cavities have been filled with the new species.

Concerning the sample obtained with the hydrothermal method, the structure is more spaced. These “separated nanowires” (called TiO₂ NWs later in this work) are clearly noticeable in *Figure 3.53b*, in which the zoom reveals bundles of nanowires more than single structures. The cross section of the sample (*Figure 3.53d*) well defines the FTO substrate, the seed layer of titania, and the length of the wires (<1 μm). Then, the Co₃O₄ layer forms a conformal shell on top of the TiO₂ array (*Figure 3.53f*). As shown in *Figure 3.54*, the core-shell structure is better highlighted in the colored version of the SEM images.

Lastly, the cross section of the sample synthesized by ALD (TiO₂ thin film) is set out in *Figure 3.55*. The expected dimensions of the deposited layers were 100 nm, for both TiO₂ and Co₃O₄. The real width, measured from the SEM images, is 88 nm for the former and 36 nm for the later. This fact can justify unexpected results from other characterizations.

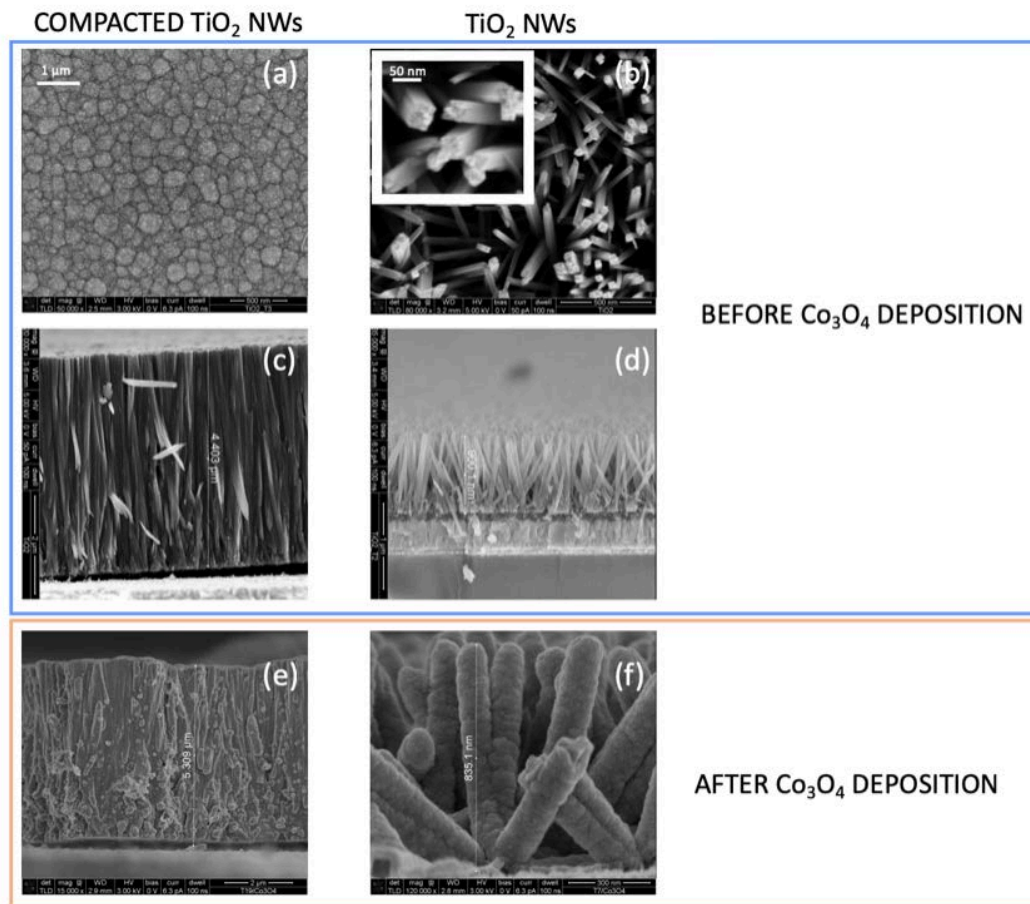


Figure 3.53 a) SEM plane view of *TiO₂* (compact); b) SEM plane view of *TiO₂*; c) Cross-section of *TiO₂* (compact); d) Cross-section of *TiO₂*; e) Cross-section of *Co₃O₄/TiO₂* (compact); f) Cross-section of *Co₃O₄/TiO₂*.

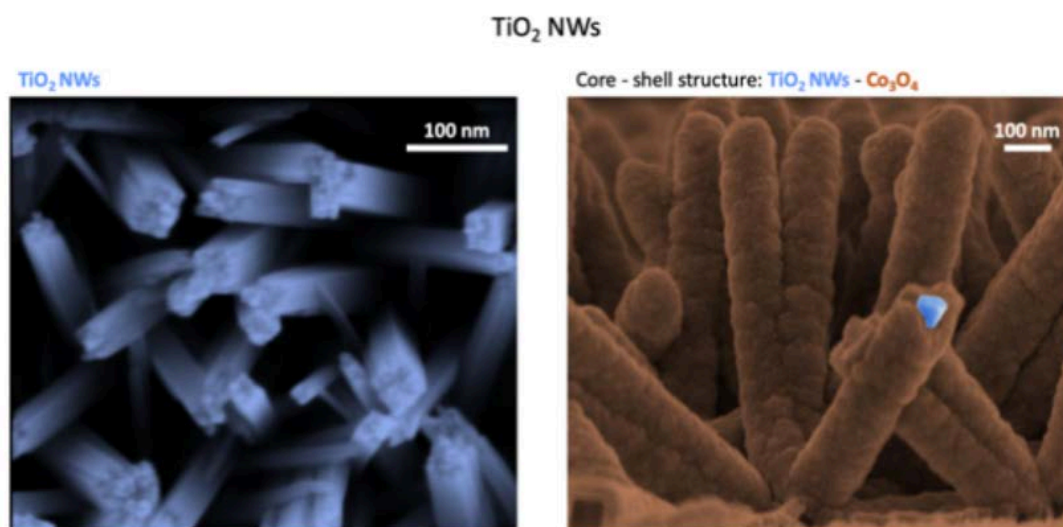


Figure 3.54 SEM images of *TiO₂* and *Co₃O₄/TiO₂*.

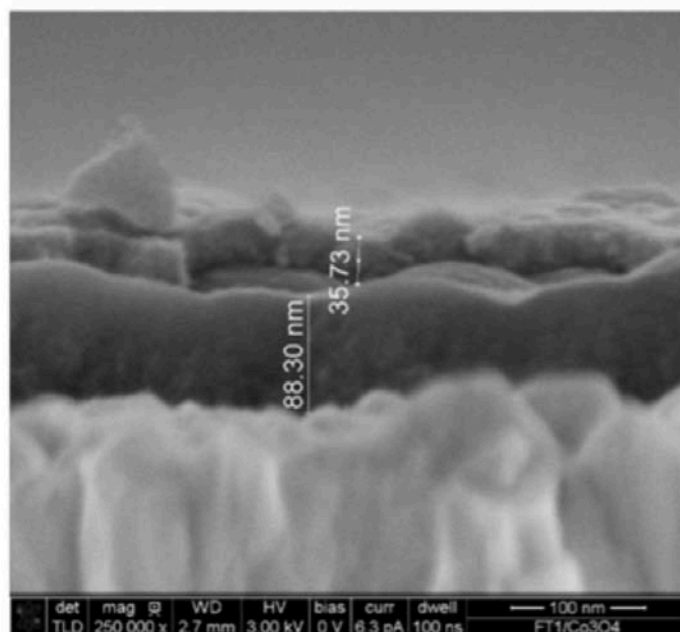


Figure 3.55 SEM cross section of TiO₂ thin film.

Undoubtedly, the most attractive samples are those concerning TiO₂ nanowires. Further information about their crystalline structures has been obtained through Raman spectra. This technique determines the form (anatase or rutile) of titanium dioxide present in the sample. The rutile phase has four active modes, two with a strong signal at 447 and 613 cm⁻¹, and two low-intensity peaks located at 143 and 236 cm⁻¹. On the other hand, the anatase phase has six Raman vibrational modes. A high-intensity peak at 144 cm⁻¹ is followed by weaker signals appearing at 197, 399, 513, 519, and 641 cm⁻¹. In the case of TiO₂ nanowires (*Figure 3.56*), the main peak of anatase and those of rutile are present at the same time. Compacted TiO₂ nanowires seem to be mainly made of Rutile (*Figure 3.57*), since there are not peaks referring to the anatase phase. According to [175], the phase mixture of different polymorphs leads to enhanced photocatalytic properties compared to pure phases. From these results, different response under illumination and electrical properties are expected from the two nanostructures.

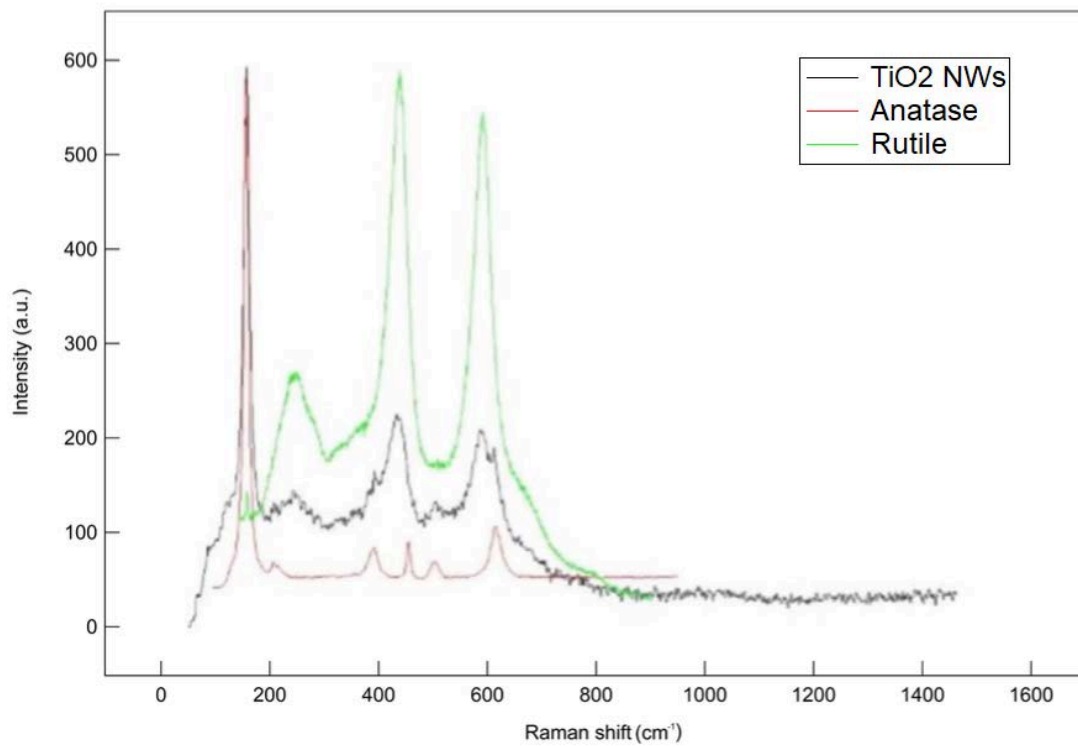


Figure 3.56 Raman spectra of *TID*.

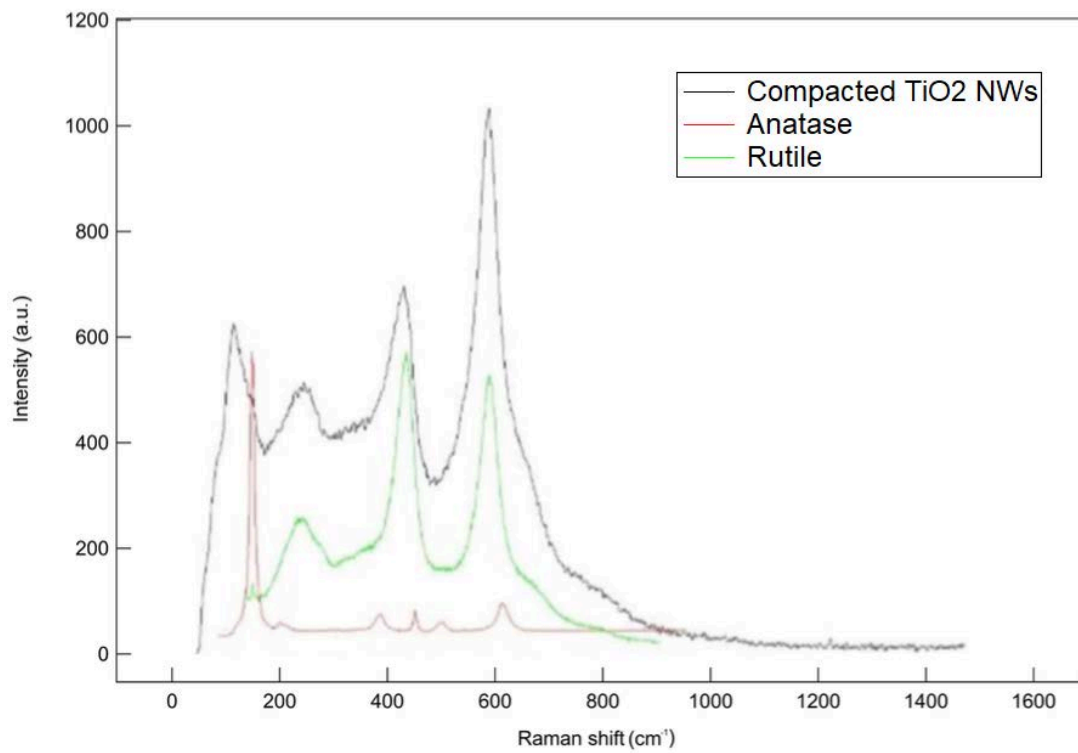


Figure 3.57 Raman spectra of *TID (compacted)*.

3.6.2 Optical properties

Photoluminescence spectra (*Figure 3.58* and *Figure 3.60*) are obtained using an excitation wavelength $\lambda_{\text{exc}} = 270$ nm. In TiO₂ NWs before the deposition of Co₃O₄, one strong peak can be observed at around 330 nm and a small one at around 420 nm. The peak at 330 nm may be due to the direct vertical transition of photo-induced electrons and holes in TiO₂ [176], whereas the one at 420 nm can be due to the band edge free exciton luminescence [177]. In the other samples, there is a peak at 355 nm, which might be due to the band to band recombination in TiO₂.

Transmittance and absorbance were measured through a spectrophotometer, in the range 350-800 nm. The TiO₂ thin film shows higher transmittance compared to the NWs, both before and after the formation of the p-n junction. The transmittance of the compacted nanowires is lower than the one of TiO₂ nanowires for wavelengths higher than 550 nm and higher for wavelengths lower than 550 nm (*Figure 3.59*). After the deposition of Co₃O₄, which is the absorbing layer, the transmitted light is reduced (*Figure 3.61*). Interference phenomena are observed in the compacted nanowires. The oscillatory character may be due to surface homogeneity and uniformity of the surface. This can cause multiple reflections between the layer and lead to interferences.

From the optical measurements, it is possible to determine the band gap of the semiconductor (TiO₂ and Co₃O₄), through the so-called Tauc Plot. Typically, a Tauc plot shows the energy of the light on the x-axis and the quantity $(\alpha E)^n$ on the y-axis, where α is the absorption coefficient. The latter can be determined from the Lambert-Beer equation, while n is equal to 2 for direct band gap semiconductors. *Figure 3.62* is relative to TiO₂ NWs, which have $E_g = 3.02$ eV. The same graphs are plotted for the other samples, and the values of the energy band gaps are reported in *Table 3.4*.

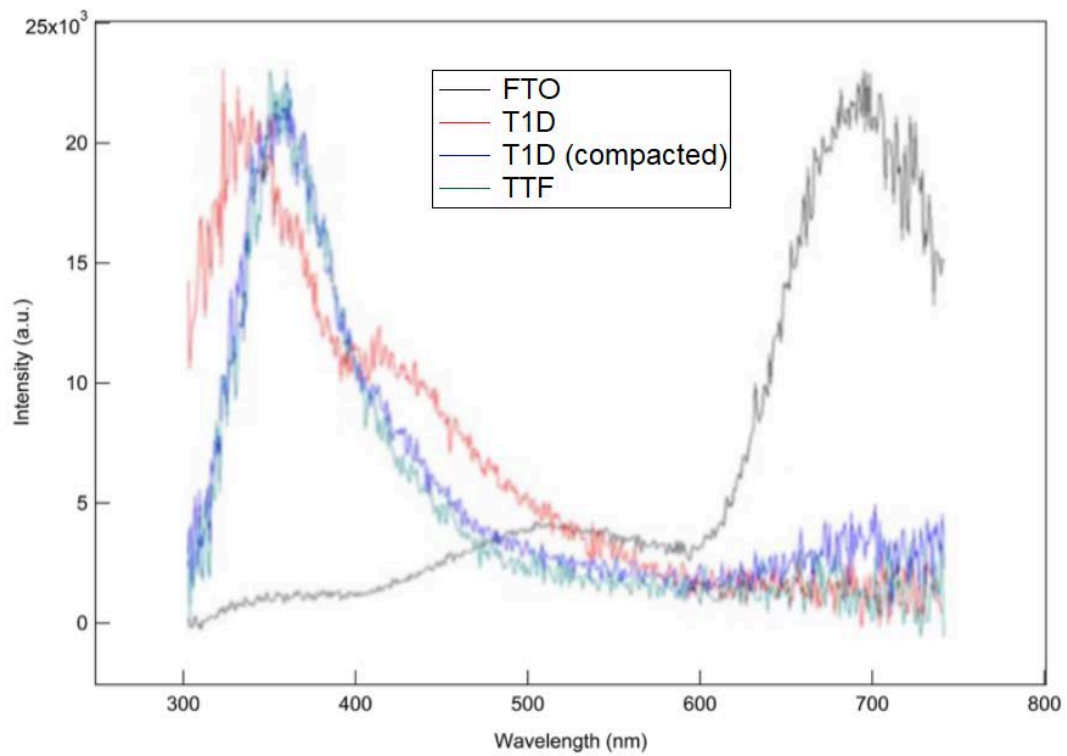


Figure 3.58 Photoluminescence spectra of TiO₂ samples before the deposition of Co₃O₄.

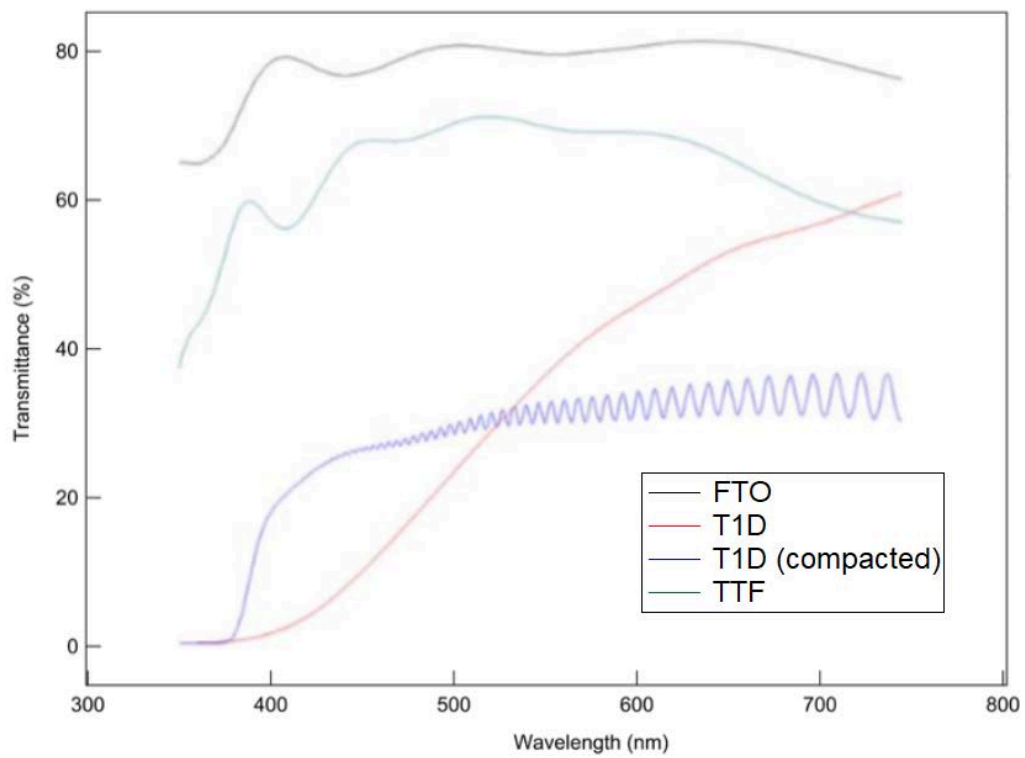


Figure 3.59 Transmittance spectra of TiO₂ samples before the deposition of Co₃O₄.

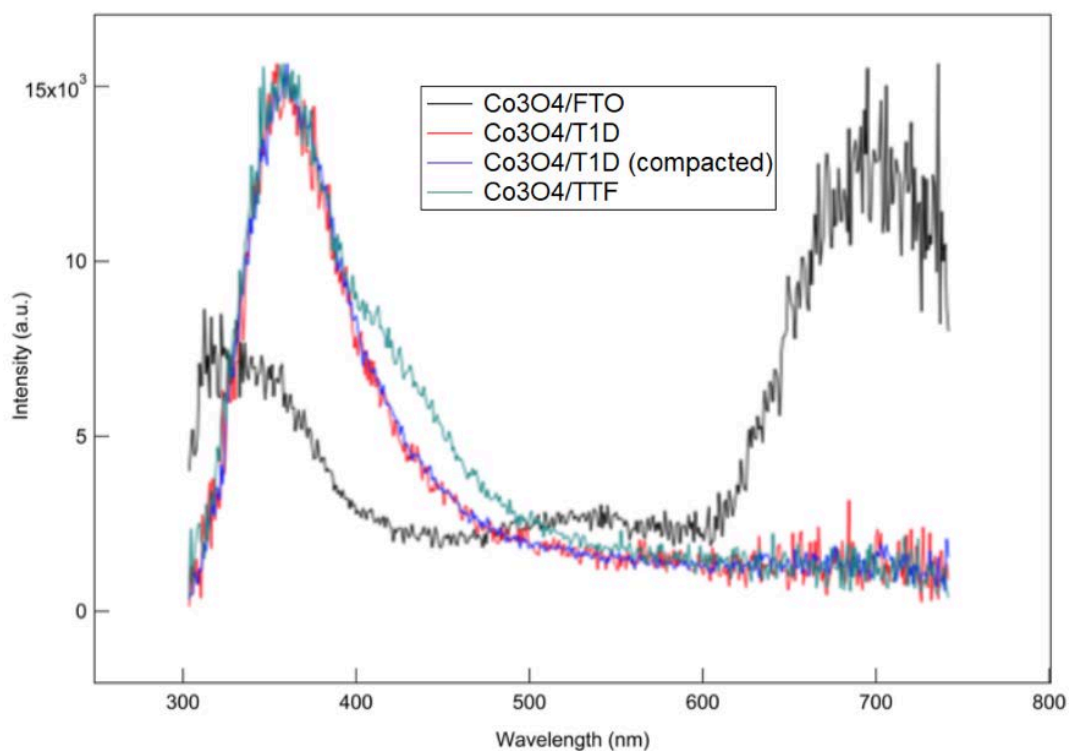


Figure 3.60 Photoluminescence spectra of TiO₂ samples after the deposition of Co₃O₄.

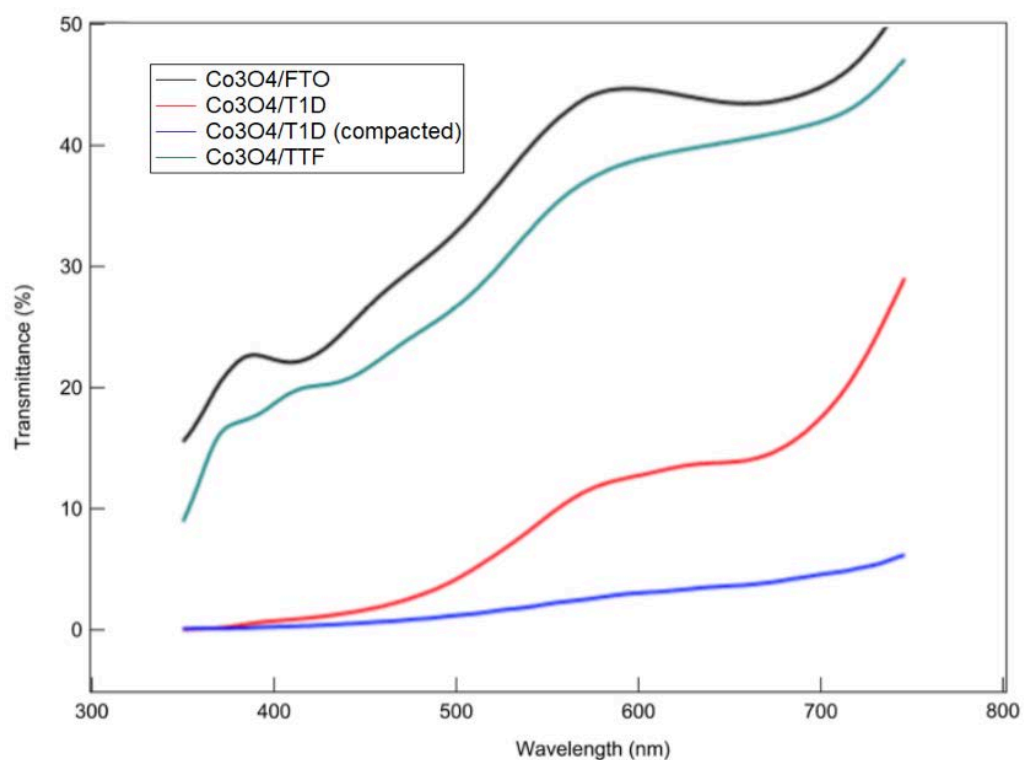


Figure 3.61 Transmittance spectra of TiO₂ samples after the deposition of Co₃O₄.

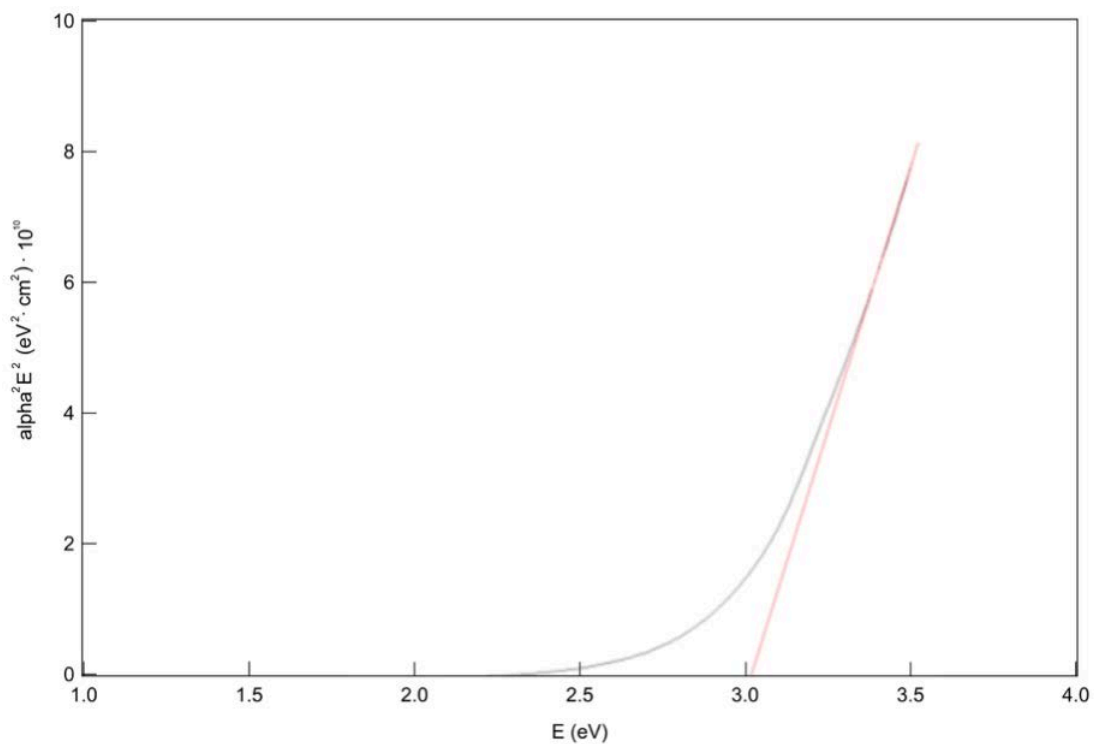


Figure 3.62 Tauc plot of *TiO₂*.

Table 3.4 Energy band gap of the different samples, calculated through the Tauc plot.

<i>Sample</i>	<i>Energy band gap</i>
TiO ₂ NWs	3.02 eV
Compacted TiO ₂ NWs	3.25 eV
TiO ₂ thin film	3.13 eV
Co ₃ O ₄ thin film	2.03 eV

3.6.3 Electrical properties

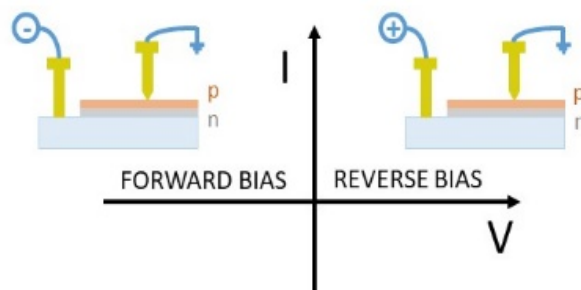


Figure 3.63 Forward and reverse bias configuration during the macro-electrical measurements.

Macro I-V curves were recorded according to the configuration illustrated in *Figure 3.63*. When a negative voltage is applied on the substrate (FTO, which is an n-type material), the p-n junction operates in forward bias. The TiO₂ layer (thin film or 1D) has been electrically characterized before (*Figure 3.64*) and after the formation of the p-n junction with Co₃O₄. The thin film of TiO₂ coated with Co₃O₄ (*Figure 3.65*) shows higher current density compared to the 1D nanostructures. Although a light effect is visible, the electrical behavior is not completely rectifying, probably due to the low thickness of the absorbing layer.

Both the samples concerning TiO₂ NWs exhibit an unexpected behavior before the cobalt oxide deposition. When the sample is under illumination, the I-V curves reveal current in the reverse bias region (*Figure 3.66* and *Figure 3.67*). This behavior is also founded in the local I-V curves obtained with the C-AFM, and it may be due to micro-junctions within the device. The best results are obtained when the real p-n junction is formed, in particular for TiO₂ NWs. Light enters the cell from the glass substrate through the FTO, the seed layer and the TiO₂ NW array. Photons are then absorbed on the Co₃O₄ active layer, and metal contacts (gold spots) are placed at the top of the most performing devices. *Figure 3.68* reports the response of the three samples to an applied voltage, in dark and light. The best photovoltaic properties are relevant to the TiO₂-Co₃O₄ core-shell NW structure (green curve) obtained by the hydrothermal method (Co₃O₄/TID). In *Figure 3.69*, the electrical behavior of the samples is studied after the deposition of Au contacts. The graphs show the voltage on the abscissa (from -0.5 V to +0.5 V) and the current density on the ordinate.

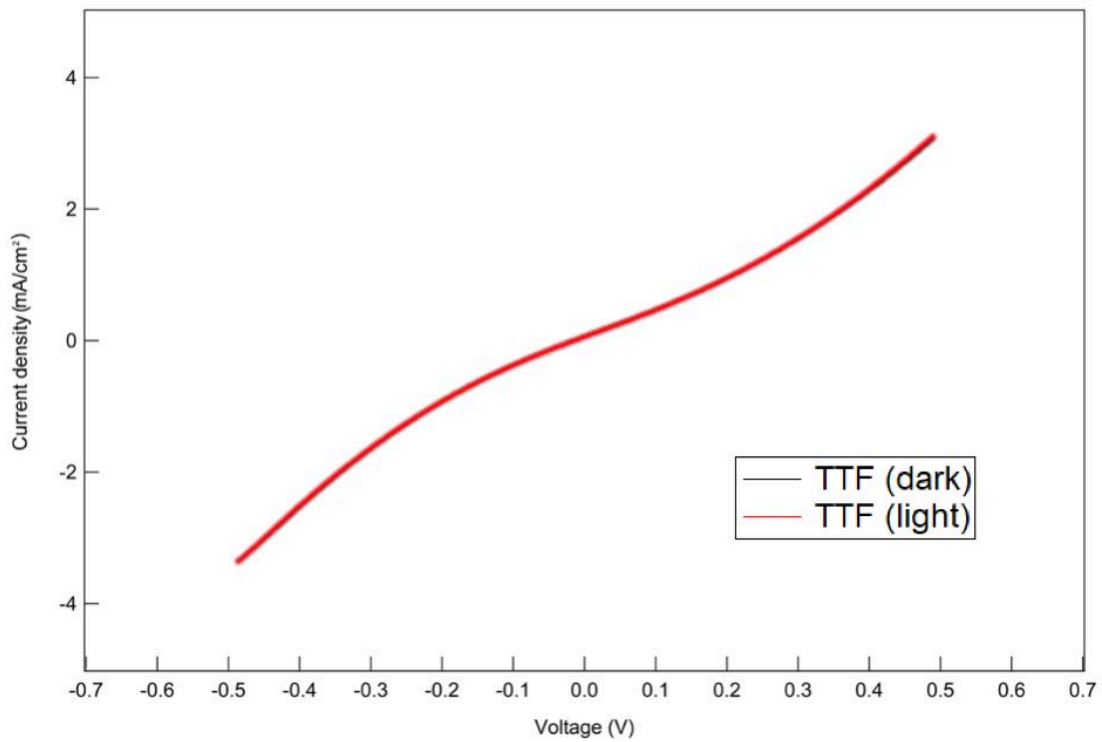


Figure 3.64 J-V curves carried out in dark and under 1 Sun illumination for *TTF*.

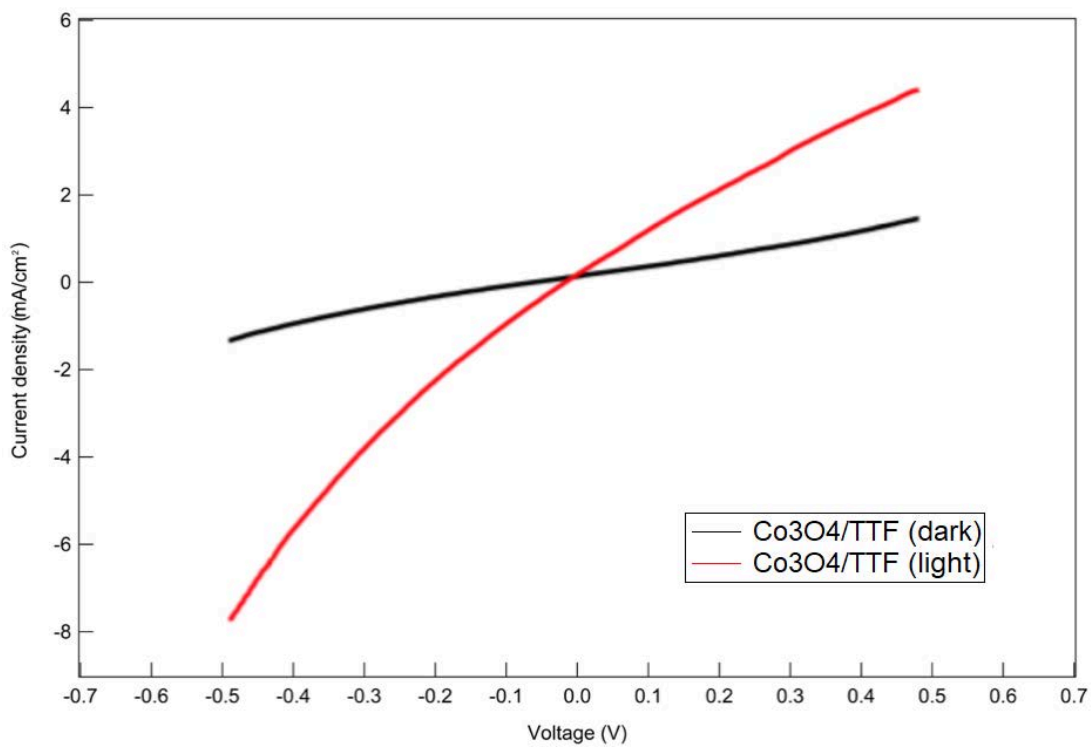


Figure 3.65 J-V curves carried out in dark (black line) and under 1 Sun illumination (red line) for *Co₃O₄/TTF*.

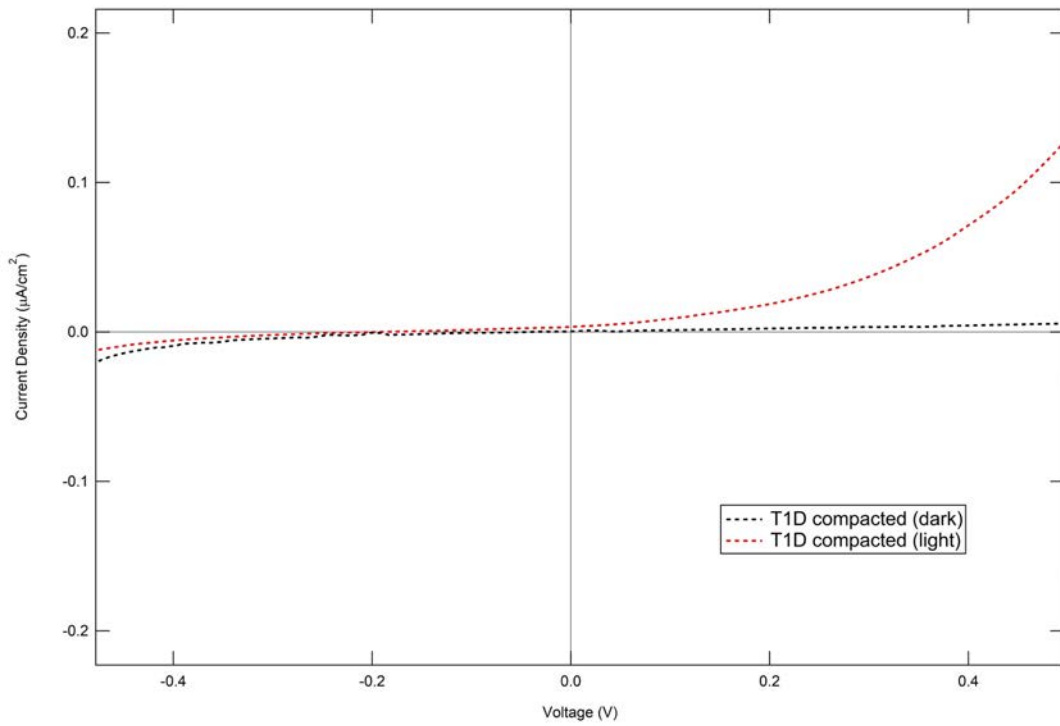


Figure 3.66 J-V curves carried out in dark (black line) and under 1 Sun illumination (red line) for *T1D (compacted)*.

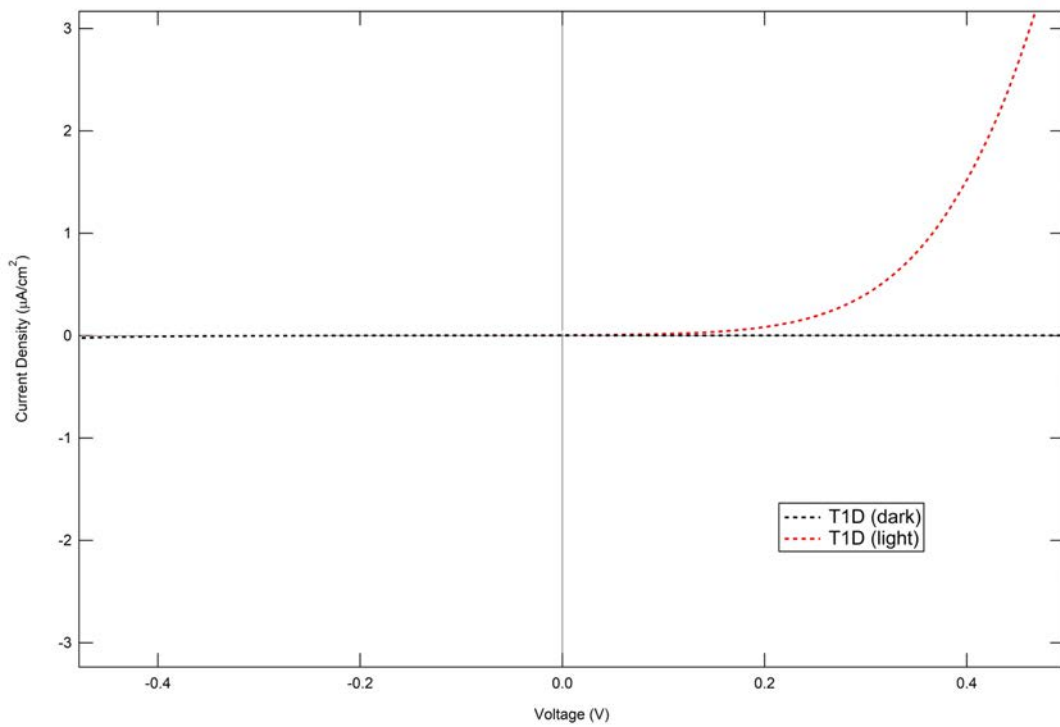


Figure 3.67 J-V curves carried out in dark (black line) and under 1 Sun illumination (red line) for *T1D*.

The current density is calculated dividing the current by the illuminated area. The diameter of the Au contact is 0.1 cm, then the illuminated area is

$$A = \pi r^2 = 0.0078 \text{ cm}^2$$

The near-ideal rectifying J-V curves under dark condition directly confirm the formation of a high-quality p-n heterojunction between Co₃O₄ and TiO₂. As can be observed in *Figure 3.69*, metal contacts help the charge carriers transfer and separation. From the green curve, it is possible to determine the PV parameters for calculating the efficiency of the cell:

- Open circuit voltage (V_{OC}) = 0.34 V
- Short-circuit current density (J_{SC}) = 50 $\mu\text{A}/\text{cm}^2$
- $V_{max} = 0.23 \text{ V}$; $J_{max} = 33.7 \mu\text{A}/\text{cm}^2$
- Fill factor (FF) (1.15) = 0.45

Taking into account that the incident light power density is 1000 W/m², the power conversion efficiency (1.16) is $0.77 * 10^{-2} \%$. Although the small value of PCE, this sample represents the first TiO₂-Co₃O₄ core-shell nanowires system that can find application in the PV area. As a matter of fact, only the thin film structure reported by Kupfer et al. [107] shows photovoltaic properties when TiO₂ and Co₃O₄ are used as window and absorbing layer, respectively.

Lastly, the photocurrent response was tested through alternating dark/light cycles (*Figure 3.70* and *Figure 3.71*). As already observed, the photocurrent density is considerably higher in the sample Co₃O₄/T1D which also has a really fast response to light. The better response and recovery to light may be due to slower recombination processes and higher quality of the interface at Co₃O₄/TiO₂ heterojunction. Moreover, the enhanced photo-response can be ascribed to the favorable Co₃O₄ band gap (2.03 eV), which plays a key role in the absorption of the photons. A scheme of the photocarrier generation is shown in *Figure 3.72*, where the band bending and the depletion region are crucial aspects for the separation of charge carriers generated under illumination.

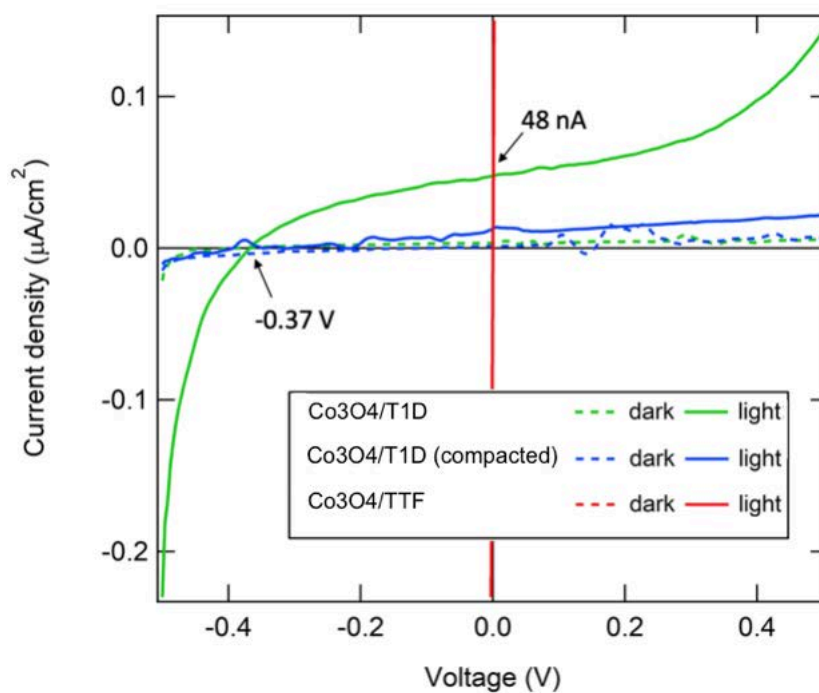


Figure 3.68 J-V curves carried out in dark (dashed lines) and under 1 Sun illumination (solid lines) for $\text{Co}_3\text{O}_4/\text{T1D}$, $\text{Co}_3\text{O}_4/\text{T1D}$ (compact), and $\text{Co}_3\text{O}_4/\text{TTF}$, before the deposition of metal contacts.

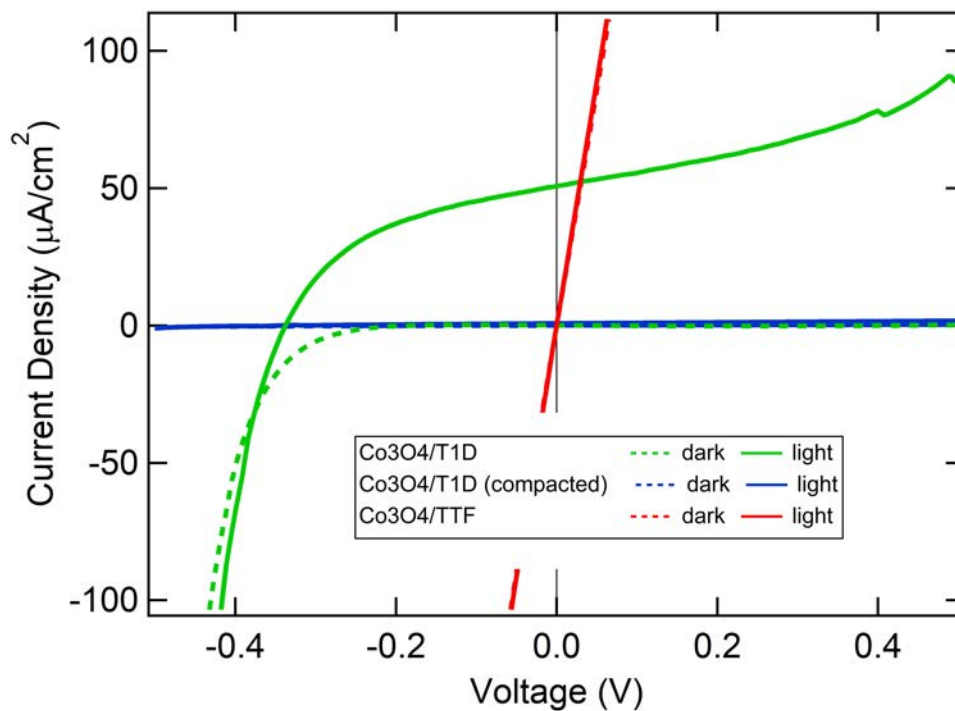


Figure 3.69 J-V curves carried out in dark (dashed lines) and under 1 Sun illumination (solid lines) for $\text{Co}_3\text{O}_4/\text{T1D}$, $\text{Co}_3\text{O}_4/\text{T1D}$ (compact), and $\text{Co}_3\text{O}_4/\text{TTF}$, after the deposition of metal contacts.

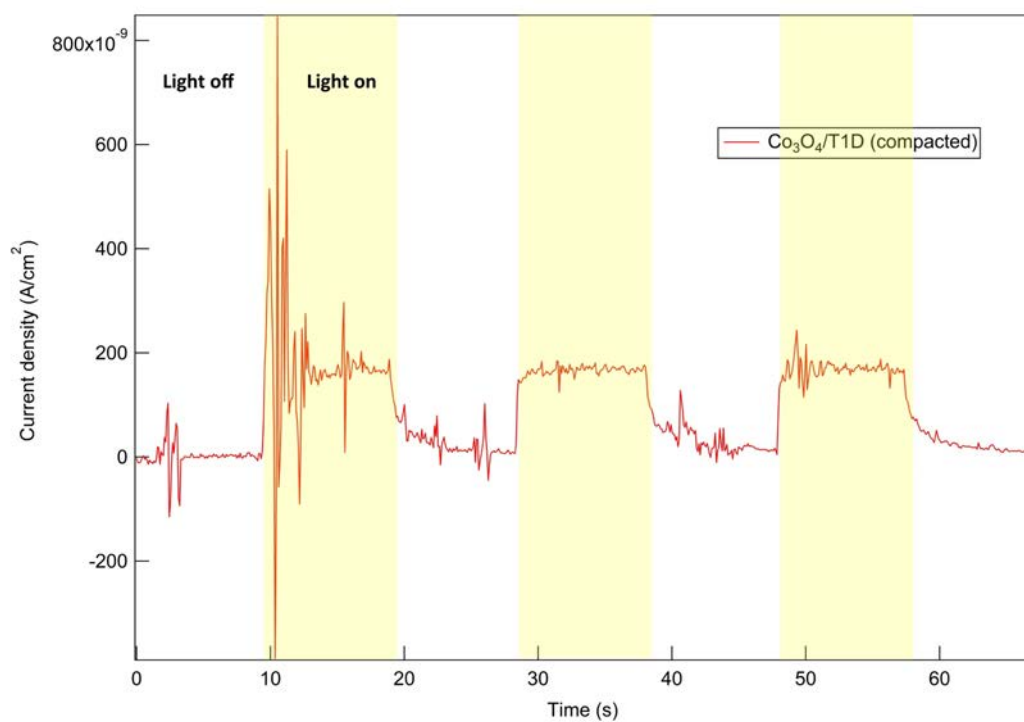


Figure 3.70 Current density vs time during dark/light cycles of 10 s at 0 V bias voltage applied to *Co₃O₄/T1D compacted*.

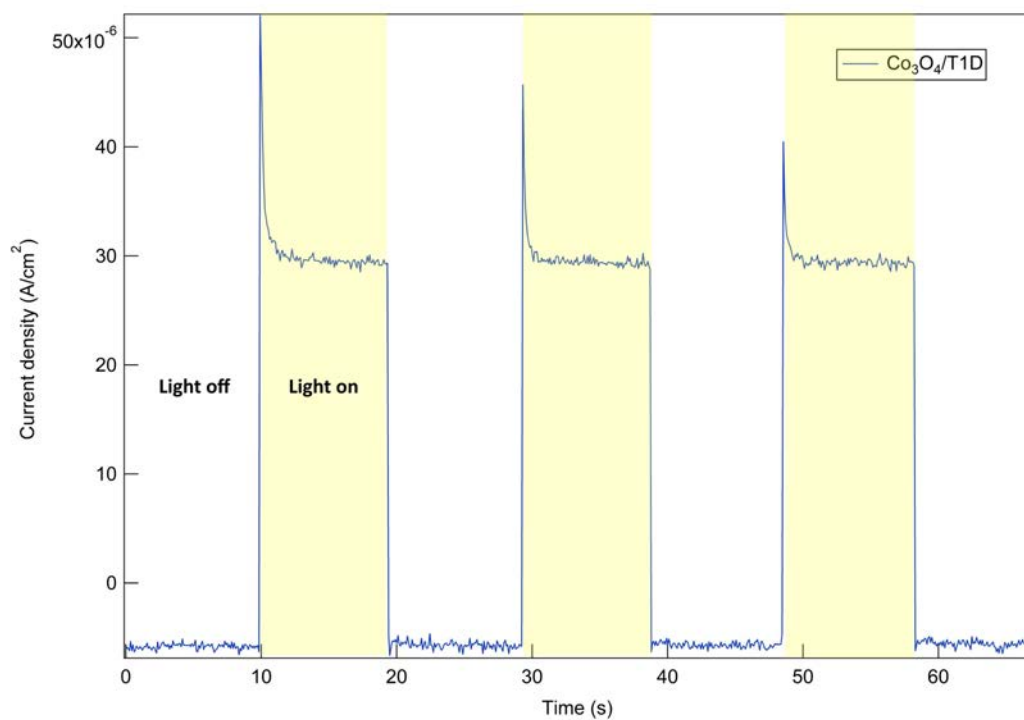


Figure 3.71 Current density vs time during dark/light cycles of 10 s at 0 V bias voltage applied to *Co₃O₄/T1D*.

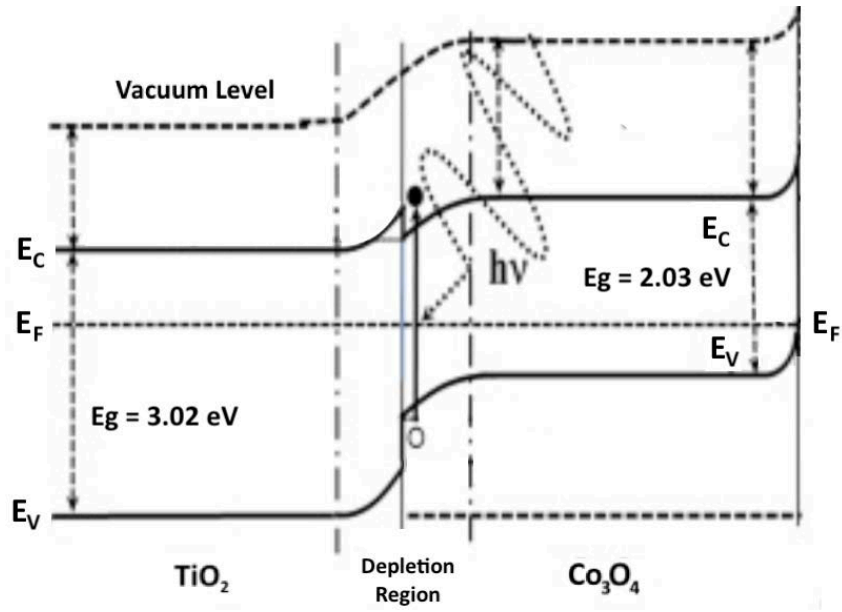


Figure 3.72 Electronic band bending and photo-response mechanism of $\text{Co}_3\text{O}_4/\text{TiO}_2$ heterojunction.

3.6.4 AFM analysis: local morphology and electrical behavior

3.6.4.1 TiO₂ nanowires

Based on the promising results gained from the macro electrical measurements, TiO₂ nanowires were ultimately characterized by C-AFM. A DCP-20 nanoprobe was used for investigating the local properties of the samples down to the nanoscale. The approach of the tip through the sample is one of the most critical issues. It has been observed that the most stable contact is obtained with a set-point equal to 0.5. Force curves similar to the one reported in *Figure 3.73* are witnesses of a good approach. From the slope of the curve and the spring constant of the tip ($k = 48$ N/m), an applied force of about 1000 nN was calculated. Then, SSRM and I-V curves in specific zones of the sample were taken at different voltages, both in dark and light. All these measurements require a protective hood and an insulating system, which shield the sample from external vibrations.

Figure 3.75 and *Figure 3.77* show the morphology and the local current distribution (at 1 V) of compacted TiO₂ NWs, respectively. The circular shape of the wires is also confirmed at the nanoscale. However, it is important to have in mind that artefacts due to the shape of the tip can be present in this AFM contact-mode configuration. A horizontal profile was taken at the same line in both the previous images: the highest peak in the local surface topography (*Figure 3.76*) corresponds to the highest electrical peak (*Figure 3.78*).

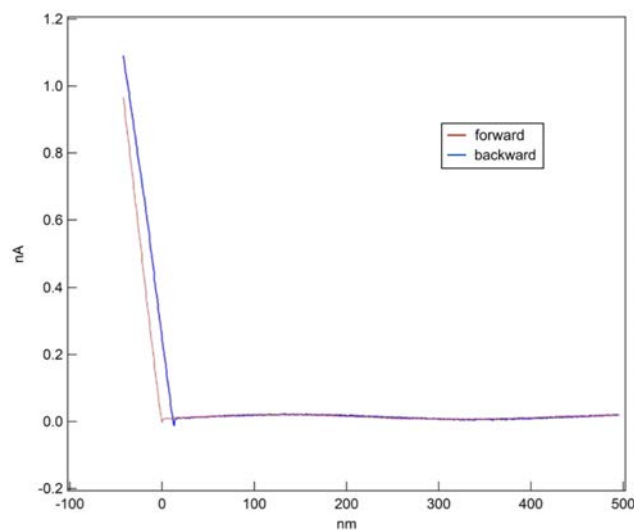


Figure 3.73 Force curve on TiO₂ NWs.

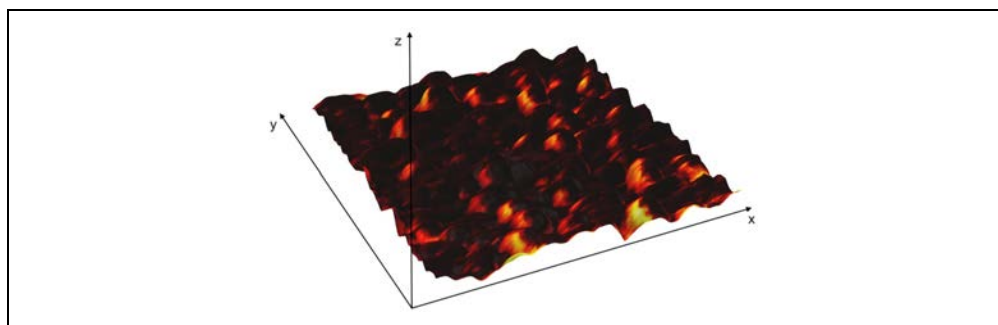


Figure 3.74 Overlap between the surface morphology and the local current distribution of *TID (compacted)*.

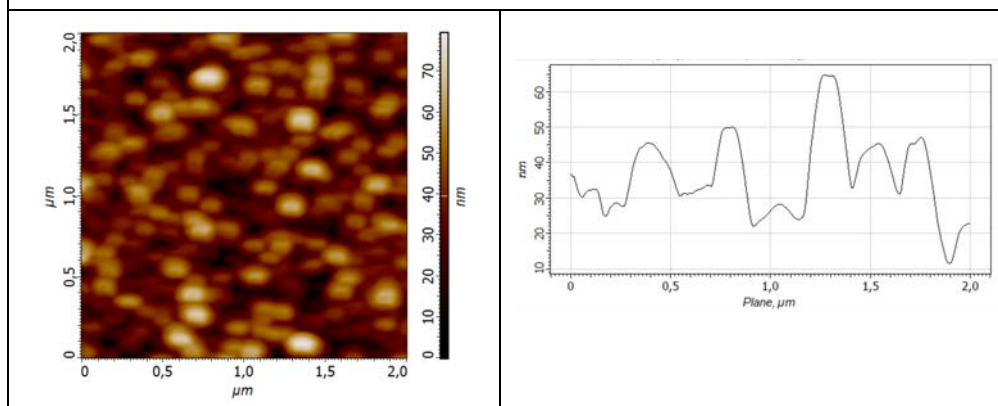


Figure 3.75 AFM surface morphology of *TID (compacted)*.

Figure 3.76 Morphology line profile of *TID (compacted)*.

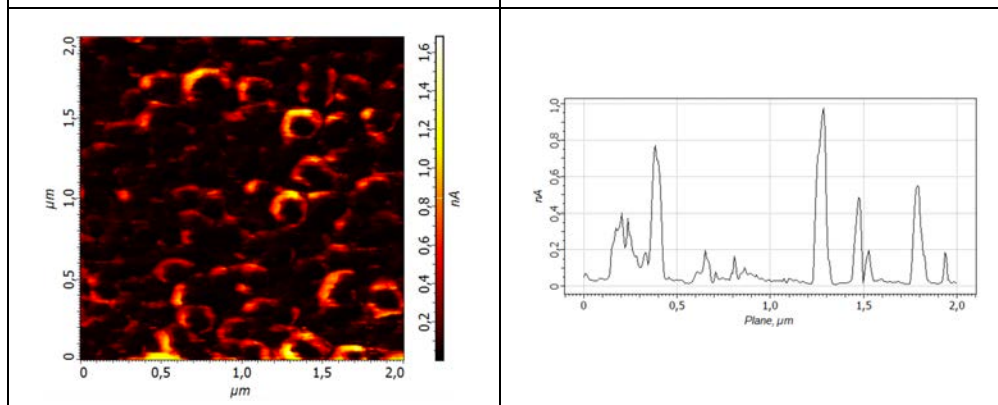


Figure 3.77 Local current map of *TID (compacted)* collected by applying 1V.

Figure 3.78 Current line profile of *TID (compacted)*.

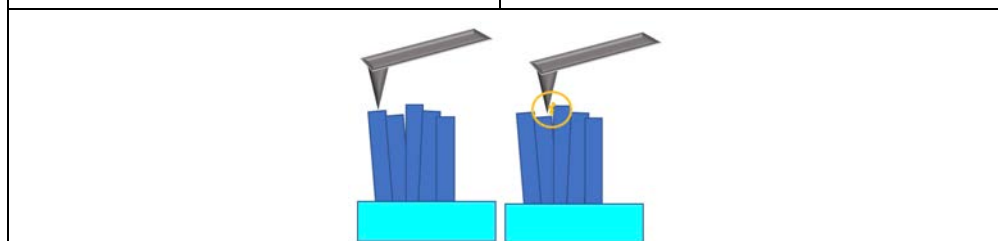


Figure 3.79 Sketch of the contact between compacted TiO_2 NWs and the tip.

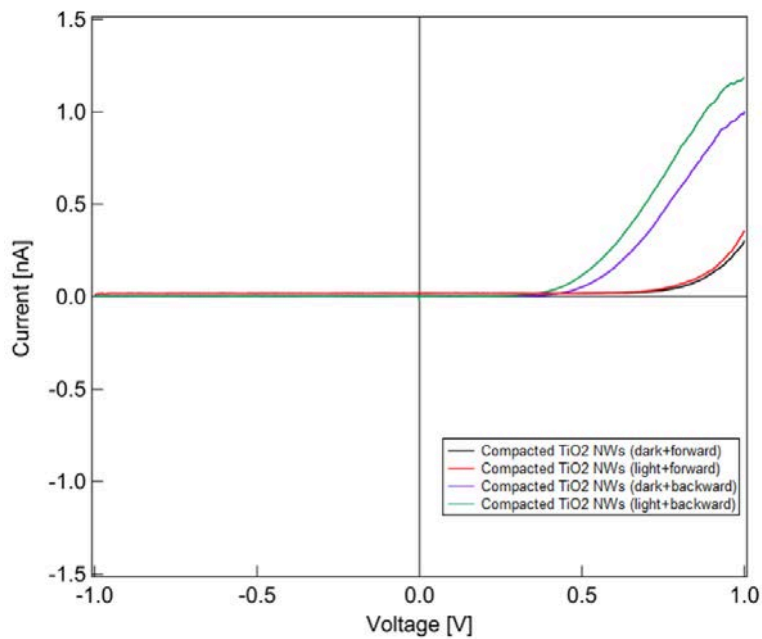


Figure 3.80 Forward and backward I-V curves in dark and light for *T1D* (compacted).

The electrical image reveals a not homogenous current distribution. As a matter of fact, the conductivity is higher at the edges of the nanowires, which seems to be insulated at the top. This phenomenon could have a physical explanation as the nanoprobe has a bigger contact area at the edges of the wires during the scanning (see the sketch in *Figure 3.79*). The overlap between the surface morphology and the local current distribution (*Figure 3.74*) confirms that the big values of the current derive from the contact of the edges of the tip and the highest nanowires.

When the applied voltage was changed to -1 V, there was no current flow within the sample (only few pA, related to noise). This behavior was also confirmed by the local I-V curves, obtained by sweeping the voltage between -1 V and +1 V. In all the previous I-V characteristics the forward curve overlapped the backward curve. In the case of TiO₂ NWs, it is worth to plot both of them (*Figure 3.80*), since different values of current are measured. The sample behaves like a diode, allowing current only in one direction. The same behavior was observed in the macro I-V curves when the nanowires were characterized under illumination. However, according to the C-AFM set-up, this is not the normal rectification direction. In an ideal Schottky diode, the forward bias current (at negative bias in the present case) is dominant. Contrary, a reversed behavior with a high tunneling current at positive voltages (reverse bias) is observed.

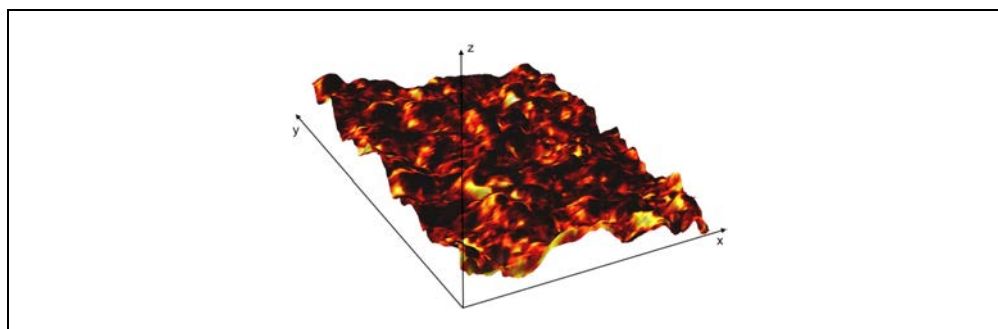


Figure 3.81 Overlap between the surface morphology and the local current distribution of *TID*.

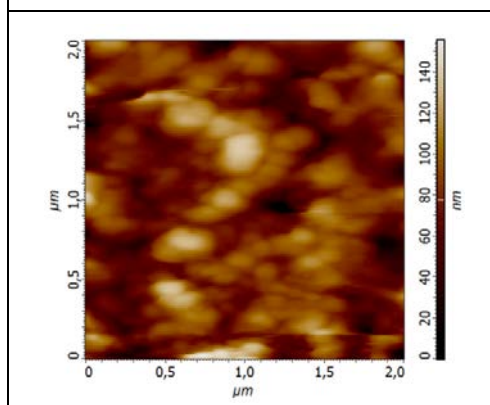


Figure 3.82 AFM surface morphology of *TID*.

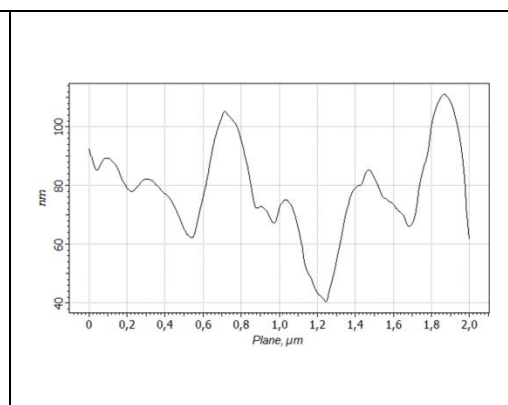


Figure 3.83 Morphology line profile of *TID*.

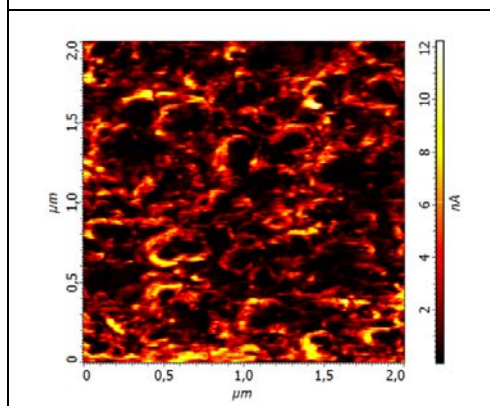


Figure 3.84 Local current map of *TID* collected by applying 1V.

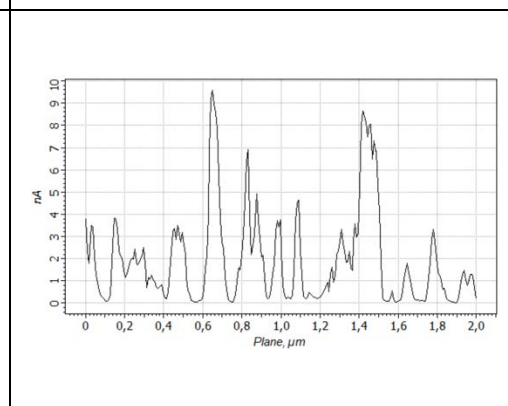


Figure 3.85 Current line profile of *TID*

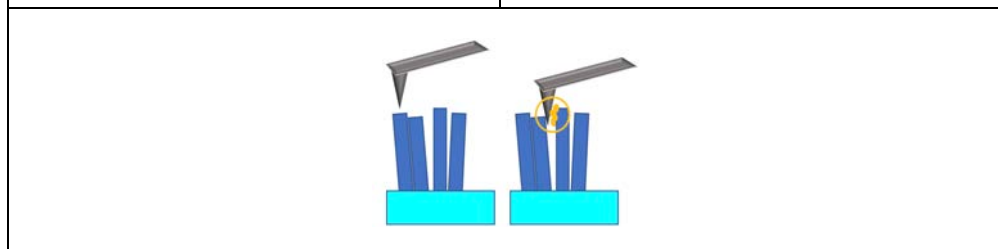


Figure 3.86 Sketch of the contact between TiO_2 NWs and the tip.

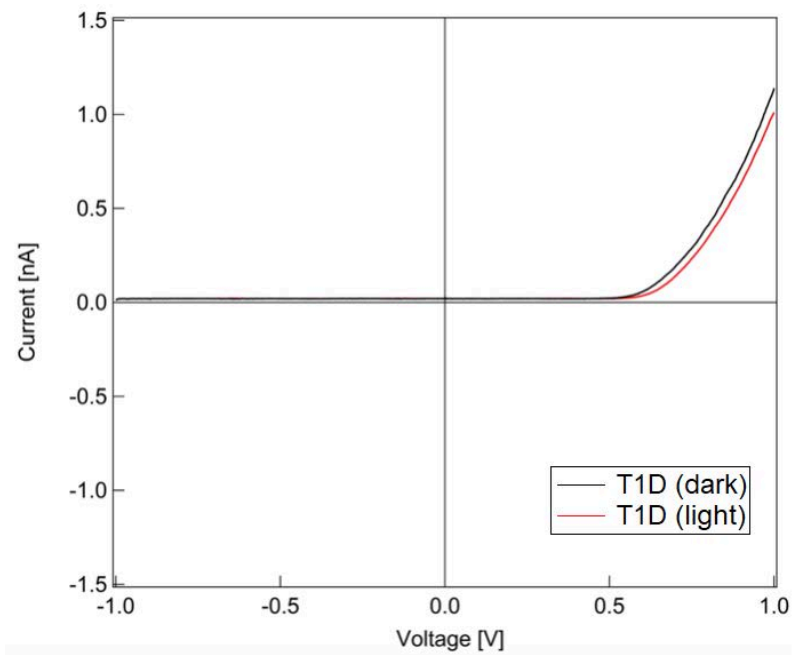


Figure 3.87 Average of 10 I-V curves in dark (black line) and light (red line) for *T1D*.

As concern TiO₂ nanowires (sample *T1D*), similar results are obtained. The worst quality of the topography (*Figure 3.82*) is due to a lack of homogeneity, which can be scratched by the tip during the scanning. As in the previous sample, the conductivity is higher at the edges of the wires (*Figure 3.84*). The larger current in this sample (10 nA vs 1 nA) may be ascribed to the spaced nanowires configuration, which leads to a bigger contact area at the edges (see sketch in *Figure 3.86*).

Once again, the correlation between the morphology and the current distribution is studied through the line profiles shown in *Figure 3.83* and *Figure 3.85*. The highest peaks in local current distribution are generally related to the highest peaks in the surface morphology of the nanowires, as it also shown in the overlap of the two images in *Figure 3.81*.

The reverse rectifying behavior is also observed in TiO₂ nanowires (*Figure 3.87*). The shape of the I-V does not change when the light is turned on.

3.6.4.2 TiO₂-Co₃O₄ core-shell nanowires

After the deposition of Co₃O₄, core-shell TiO₂-Co₃O₄ NWs show interesting results. SSRM was carried out in air by applying +2 V and -2 V on the sample, while the scanning tip is grounded. Measurements in dark (*Figure 3.88* and *Figure 3.89*) and light (*Figure 3.90* and *Figure 3.91*) are used to study the effect of the incoming photons, which can generate photocarriers. The current scale on the right points out an enhanced current when the sample is under illumination, which means that the photons making up the light induce electrons and holes. Unfortunately, it is not possible to observe the rectifying behavior of the junction at the nanoscale, probably because of local physical phenomena that interfere with the measurements, or because of the different contact between the AFM tip and the Co₃O₄ layer. In any case, the sample with TiO₂ nanowires is more conductive than the one with compacted nanowires (see I-V curves in *Figure 3.92*). The power of the small LED that shines the sample from the bottom is not high enough to see a clear light effect. Unlike the macro electrical measurements, no PV effect is pointed out with C-AFM.

The low local current measured on the p-n junction can be ascribed to the ALD Co₃O₄ layer. To study the behavior of the p-layer, an FTO glass was covered by a thin layer of Co₃O₄. *Figure 3.93* shows its I-V curve, in the bias range ± 4 V. Macro-electrical measurements previously revealed that the cobalt oxide layer reduces the conductivity of FTO, and the light does not have an effect on the sample. The local I-V curves nothing but confirm these aspects.

Among the DCP20, it was planned to test other tips during the AFM measurements. However, lower radius tip, such as NSC14/Cr-Au, lead to bad approaches, which did not allow any further measurements.

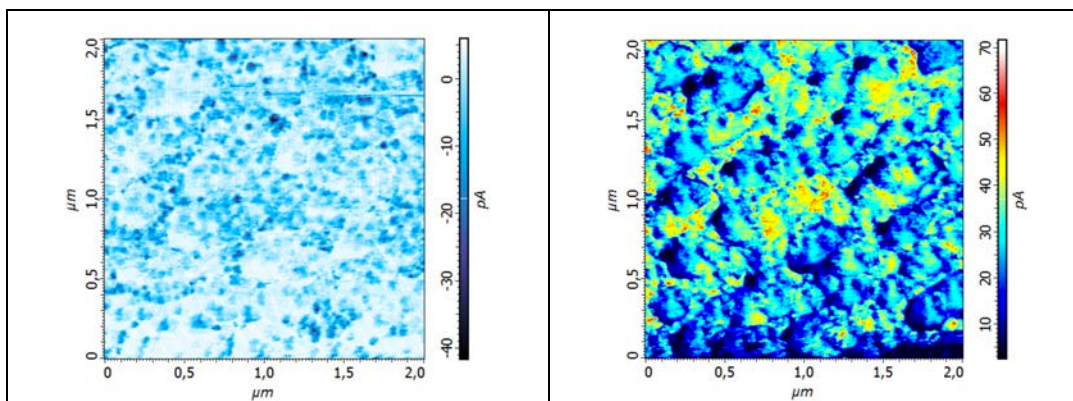


Figure 3.88 Local current map of Co₃O₄/TiD collected with C-AFM by applying -2V (dark).

Figure 3.89 Local current map of Co₃O₄/TiD collected with C-AFM by applying +2V (dark).

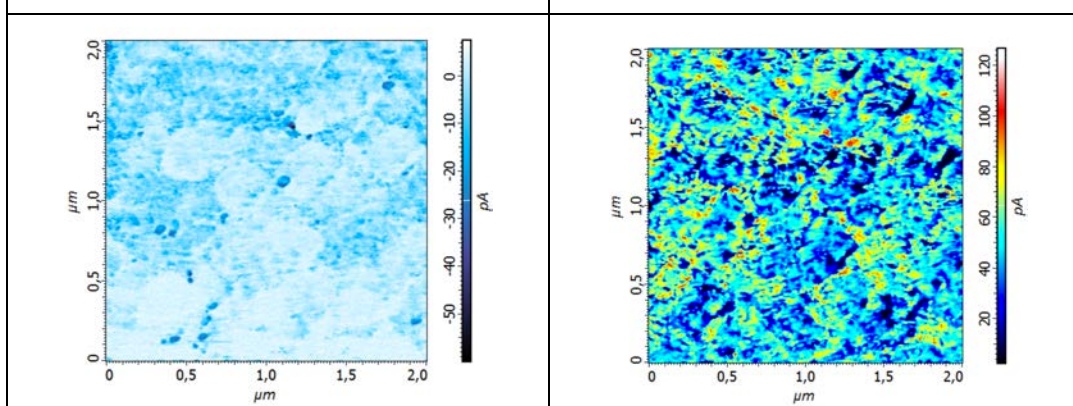


Figure 3.90 Local current map of Co₃O₄/TiD collected with C-AFM by applying -2V (light).

Figure 3.91 Local current map of Co₃O₄/TiD collected with C-AFM by applying +2V (light).

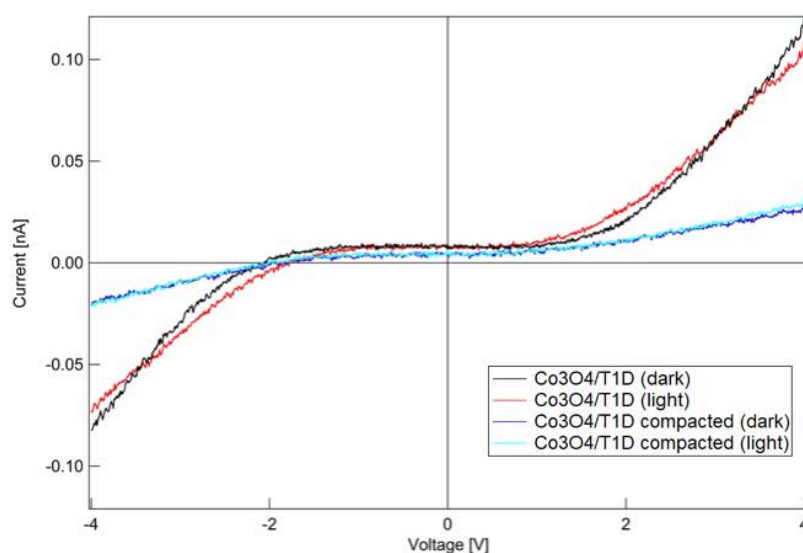


Figure 3.92 Dark and light local I-V curves for Co₃O₄/TiD and Co₃O₄/TiD (compacted).

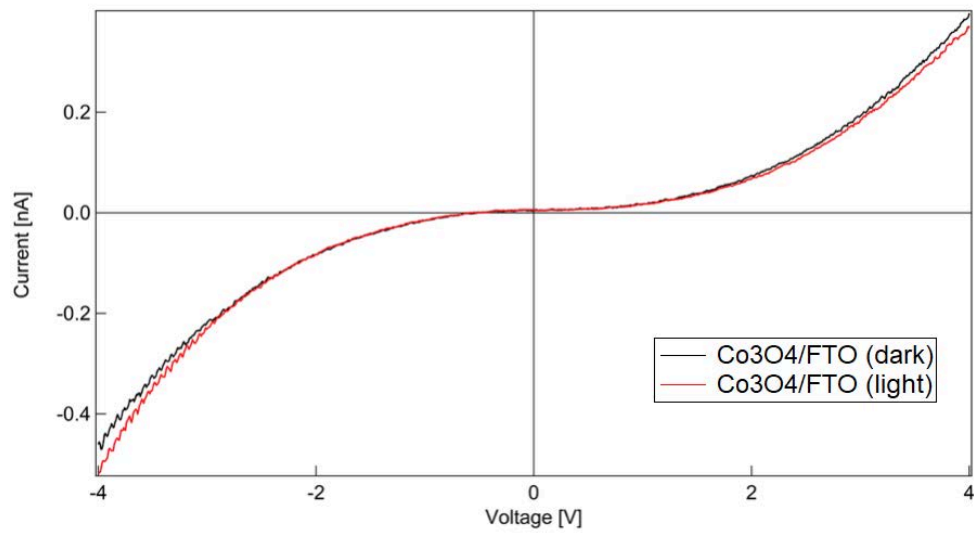


Figure 3.93 Dark and light local I-V curves for $\text{Co}_3\text{O}_4/\text{FTO}$.

4 CONCLUSIONS AND FUTURE WORKS

In this work, hydrothermally grown nanowires (ZnO and TiO₂) of n-type oxides have been conformally covered by p-type oxides (Cu₂O and Co₃O₄) by different deposition methods, like ALD, CVD and reactive magnetron sputtering. Compared to the traditional thin film geometry, the obtained core-shell p-n nanostructure shows:

- Enhanced light trapping (multiple reflections).
- Improved charge collection and transport.
- Reduced use of materials.
- Decoupled light absorption and carrier collection pathways.

Cu₂O/ZnO, Co₃O₄/ZnO, and Co₃O₄/TiO₂ heterojunctions have been investigated by means of structural, morphological, optical and electrical techniques. Core-shell TiO₂-Co₃O₄ NWs exhibit good photodetection (with a fast response time <0.1 s) and photovoltaics performances (achieving V_{OC} = 0.34 V, J_{SC} 50 = μA/cm² and FF = 45%, in the macroscopic J-V characteristic). The suitable energy gap of Co₃O₄ (two optical direct band gaps in the visible region, 1.5 and 2.1 eV) and its electronic band structure in terms of positioning of conduction and valence bands with respect to vacuum, matches very well the position of TiO₂ conduction band to build-up an efficient p-n heterojunction.

Furthermore, the use of C-AFM and IS-AFM as characterization techniques allowed to obtain the local photo-electrical properties of the investigated oxide materials at the nanoscale. A photovoltaic effect has been pointed out in ZnO nanowires by means of C-AFM, which also confirms the presence of a p-n rectifying junction when Cu₂O was deposited onto bare ZnO NWs.

Lastly, a novel thin film geometry consisting of an ALD Cu₂O layer sandwiched between two sputtered layers of ZnO and Cu₂O has been studied. The additional Cu₂O film acts as “blocking layer”, which helps the charge separation. Good photovoltaics performances have been measured both in the macroscopic J-V characteristic (achieving V_{OC} = 0.32 V and J_{SC} = 0.8 μA/cm²) and in the C-AFM measurements.

These exciting results open to new possible oxides combinations, such as TiO_2 as n-type nanostructured material and Cu_2O as p-type material, to form core-shell NWs. Moreover, different thickness of the absorbing layer may lead to higher power conversion efficiency. Although the photovoltaic performances are still much lower than the traditional devices, all-oxides solar cells are widely investigated because of their inexpensiveness, chemical stability, and non-toxicity.

5 ITALIAN SUMMARY

L'attività di ricerca legata alla stesura della tesi è stata condotta presso Luleå University of Technology (Svezia), nei laboratori di ricerca del professor Alberto Vomiero (*Experimental Physics Group, Division of Materials Science*). Questo lavoro si colloca all'interno di un progetto relativo alla sintesi e caratterizzazione di dispositivi fotovoltaici basati sull'impiego di ossidi di tipo n e di tipo p, di varie forme (1-dimensionali e film sottili) e combinazioni. L'obiettivo futuro è quello di aumentare l'efficienza e diminuire il costo delle celle solari, le quali rappresentano l'alternativa più promettente ai combustibili fossili. La ricerca sul fotovoltaico è notevolmente cresciuta negli ultimi anni e, accanto alle consolidate tecnologie che impiegano il silicio nella conversione della luce solare in energia elettrica, nuove tipologie di celle sono state sviluppate. Tra di esse è possibile ricordare le celle perovskitiche (*perovskite solar cells*) e le celle di Grätzel (*dye-sensitized solar cells*), nelle quali l'impiego di ossidi risulta di fondamentale importanza nell'ottenimento di elevate efficienze.

Una nuova classe costituita da celle interamente basate sull'utilizzo di ossidi di metalli di transizione (ZnO , TiO_2 , Co_3O_4 , Cu_2O , ...) prende il nome di *all-oxide solar cells*. In esse, gli ossidi di tipo p (Cu_2O e Co_3O_4) agiscono come strato attivo, in cui la luce viene assorbita e convertita in corrente elettrica mediante la promozione di elettroni nella banda di conduzione e lacune nella banda di valenza. Il crescente interesse verso questa nuova generazione è dovuto al fatto che gli ossidi metallici sono stabili chimicamente, abbondanti in natura e non tossici. Inoltre, essendo anche realizzate attraverso metodi di produzione e materiali poco costosi, le celle solari a base ossidi risultano essere ecologiche, stabili nel tempo ed economiche. Negli ultimi anni il maggiore interesse dei ricercatori è legato all'utilizzo di ZnO come ossido di tipo n, sintetizzato sia come film sottile sia in strutture 1-dimensionali di dimensioni nanometriche (es. *nanowires* e *nanorods*). Queste ultime configurazioni portano ad un trasporto di carica più veloce e ad una maggiore probabilità di assorbimento per i fotoni, in quanto la luce rimane confinata all'interno del *nanoarray*. Il dispositivo optoelettronico è completato con la deposizione dell'ossido di tipo p, che porta alla formazione di una giunzione p-n all'interfaccia tra i due ossidi. Cu_2O o Co_3O_4 possono essere depositati in forma di film sottile oppure possono uniformemente coprire i *nanowires*, in una configurazione chiamata *core-shell*.

In questa tesi, diverse tipologie di ossidi e di combinazioni sono state caratterizzate. L'obiettivo principale del progetto riguarda la caratterizzazione elettrica dei dispositivi, a partire da un punto di vista macroscopico arrivando alle proprietà locali a livello nanometrico. *Nanowires* di ZnO e TiO₂ sono stati idrotermicamente sintetizzati e uniformemente coperti dagli ossidi di tipo p (Cu₂O and Co₃O₄) mediante differenti metodi di deposizione, come ALD (*atomic layer deposition*), CVD (*chemical vapor deposition*) e sputtering. La caratterizzazione dei campioni è stata eseguita attraverso misure ottiche, elettriche e morfologiche. Le immagini SEM hanno confermato la presenza di TiO₂-Co₃O₄ *core-shell nanowires*, caratterizzati inoltre da buone proprietà fotovoltaiche. Dalle curve J-V a livello macroscopico si sono ricavati il voltaggio a circuito aperto ($V_{OC} = 0.34$ V), la densità di corrente a circuito chiuso ($J_{SC} = 50$ μ A/cm²) e il fattore di riempimento (FF = 45%). I gap di energia e la struttura elettronica di Co₃O₄ in termini di posizionamento della banda di conduzione e della banda di valenza rispetto al vuoto si combinano in modo perfetto con la banda di conduzione del TiO₂ nel formare un'efficiente eterogiunzione p-n.

Accanto alle tradizionali caratterizzazioni quali XRD e proprietà ottiche, il cuore centrale di questo lavoro è relativo all'impiego del microscopio a forza atomica (AFM), appartenente alla classe dei microscopi a scansione di sonda, sia per valutare proprietà morfologiche sia per studiare fenomeni elettrici locali che avvengono su scala nanometrica. La topografia superficiale dei campioni viene riprodotta con risoluzione sub-nanometrica misurando le forze di interazione tra una sonda (*probe*) o punta (*tip*) montata all'estremità di una micro-leva (*cantilever*) e la superficie del campione in esame. L'implementazione dello strumento con una punta conduttiva e un preamplificatore consente di misurare la distribuzione locale di corrente elettrica. La tecnica in questione prende il nome di *conductive-AFM* e consente di collegare informazioni elettriche con la morfologia superficiale del campione. Misure in luce e buio consentono inoltre di ottenere proprietà fotoelettriche a livello locale, le quali possono confermare o meno la presenza di una giunzione p-n. È importante ricordare che una giunzione p-n si comporta come un diodo, ovvero consente il passaggio di corrente solo in polarizzazione diretta. Questo comportamento rettificante è confermato nei campioni di ZnO *nanowires* uniformemente coperti da Cu₂O o Co₃O₄. Il microscopio a forza atomica può essere inoltre accoppiato con un potenziostato per

condurre misure di spettroscopia di impedenza a livello locale, la quale permette di analizzare la resistenza elettrica dei campioni.

Infine, un campione a film sottile è stato testato per valutare l'effetto di uno strato di Cu_2O depositato mediante ALD tra due strati di ZnO e Cu_2O sintetizzati per sputtering. Buone performance fotovoltaiche sono state misurate dalle curve J-V caratteristiche ($V_{\text{OC}} = 0.32 \text{ V}$ and $J_{\text{SC}} = 0.8 \mu\text{A}/\text{cm}^2$) sia a livello macroscopico sia mediante C-AFM.

Questo studio rappresenta il primo passo verso la sintesi di dispositivi a base ossido sempre più efficienti. Nuove combinazioni, quali TiO_2 come materiale di tipo n e Co_3O_4 come materiale di tipo p, sono attualmente in fase di studio nei laboratori di ricerca dell'università di Luleå. Nonostante le efficienze siano al giorno d'oggi molto inferiori rispetto ai dispositivi tradizionali, gli interessi in questo ambito sono destinati ad aumentare, con ricercatori guidati dall'affascinante idea di poter realizzare celle *environmentally friendly*, che al tempo stesso siano economiche e stabili chimicamente.

6 BIBLIOGRAPHY

- [1] IEA, “World Energy Outlook 2015. Executive Summary,” 2015.
- [2] Intergovernmental Panel on Climate Change, *Climate Change 2014 Synthesis Report - IPCC*. 2014.
- [3] International Energy Agency, “Key World Energy Statistics,” *Statistics*. 2018.
- [4] International Energy Agency, “Energy Efficiency Market Report:Executive Summary,” 2014.
- [5] Epia, “Global market outlook for photovoltaics 2014-2018.” 2014.
- [6] C. J. Yang, “Reconsidering solar grid parity,” *Energy Policy*, 2010.
- [7] G. Chen, J. Seo, C. Yang, and P. N. Prasad, “Nanochemistry and nanomaterials for photovoltaics,” *Chemical Society Reviews*. 2013.
- [8] L. M. Fraas, *Low-cost solar electric power*. 2014.
- [9] V. G. Belessiotis and E. Papanicolaou, “History of solar energy,” in *Comprehensive Renewable Energy*, 2012.
- [10] H. Z. Å and Wei, “The history of solar,” *Solar Energy Materials and Solar Cells*, 2011.
- [11] Fraunhofer Institute for Solar Energy Systems ISE, “New world record for solar cell efficiency at 46%,” *Fraunhofer Institute for Solar Energy Systems ISE*, 2014.
- [12] K. Mertens and K. Hanser, “Photovoltaics : Fundamentals, Technology and Practice,” in *Photovoltaics : Fundamentals, Technology and Practice*, 2013.
- [13] G. Otnes, *III-V Nanowire Solar Cells : Growth and Characterization*. Lund University, 2018.
- [14] D. Neaman, *Semiconductor physics and devices - Basic Principles*. 2006.
- [15] F. Gaspari, “Semiconductors,” in *Comprehensive Energy Systems*, 2018.
- [16] F. A. de S. Lima, “Application of Transition-Metal-Oxide-Based Nanostructured Thin Films on Third Generation Solar Cells Application of Transition-Metal-Oxide-Based Nanostructured Thin Films on Third Generation Solar Cells,” pp. 1–247, 2015.
- [17] R. Eisberg, R. Resnick, and J. Brown, “*Quantum Physics of Atoms, Molecules, Solids, Nuclei, and Particles*,” *Phys. Today*, 1986.
- [18] A. Razumovsky, “Energy-band theory.” [Online]. Available:

<http://eng.thesaurus.rusnano.com/wiki/article853>.

- [19] R. F. Pierret, "Semiconductor Device Fundamentals," *New York*, 1996.
- [20] A. Castro, *Proprietà fisiche della materia*. Padova, 2009.
- [21] S. M. Sze and K. N. Kwok, *Physics of Semiconductor Devices*. 2007.
- [22] R. Hummel, *Electronic Properties of Materials*. 2011.
- [23] W. Shockley, "The Theory of p-n Junctions in Semiconductors and p-n Junction Transistors," *Bell Syst. Tech. J.*, 1949.
- [24] D. J. Fitzgerald and A. S. Grove, "Surface recombination in semiconductors," *Surf. Sci.*, 1968.
- [25] M. De Bastiani, "The stability of third generation solar cells," King Abdullah University of Science and Technology, 2016.
- [26] A. S. Sedra and K. C. Smith, *Microelectronic Circuits, Seventh Edition*. 2014.
- [27] M. S. Rogalski and S. B. Palmer, *Solid state physics*. 2014.
- [28] M. Rudan, *Physics of Semiconductor Devices*. 2015.
- [29] T. Soga, "Fundamentals of Solar Cell," in *Nanostructured Materials for Solar Energy Conversion*, 2006.
- [30] L. T. Wong and W. K. Chow, "Solar radiation model," *Appl. Energy*, 2001.
- [31] P. Wurfel, "The chemical potential of radiation," *J. Phys. C Solid State Phys.*, 1982.
- [32] The National Renewable Energy Laboratory (NREL), "Reference Solar Spectral Irradiance: Air Mass 1.5," *American Society for Testing and Materials (ASTM) - Terrestrial Reference Spectra for Photovoltaic Performance Evaluation*, 2012. .
- [33] A. Mohammad Bagher, "Types of Solar Cells and Application," *Am. J. Opt. Photonics*, 2015.
- [34] S. Honsberg, Christiana; Bowden, "Solar Cell Efficiency | PVEducation," © 2018 PVEducation, 2018. .
- [35] P. Sidi, D. Sukoco, W. Purnomo, H. Sudiby, and D. Hartanto, "Electric Energy Management and Engineering in Solar Cell System," in *Solar Cells - Research and Application Perspectives*, 2013.
- [36] A. Luque and S. Hegedus, *Handbook of Photovoltaic Science and Engineering*. 2011.
- [37] J. L. Gray, "The Physics of the Solar Cell," in *Handbook of Photovoltaic Science and Engineering*, 2011.

- [38] A. Blakers, N. Zin, K. R. McIntosh, and K. Fong, "High Efficiency Silicon Solar Cells," *Energy Procedia*, vol. 33, pp. 1–10, 2013.
- [39] K. Ranabhat, L. Patrikeev, A. A. evna Revina, K. Andrianov, V. Lapshinsky, and E. Sofronova, "An introduction to solar cell technology," *J. Appl. Eng. Sci.*, 2016.
- [40] First solar, "First Solar achieves yet another cell conversion efficiency world record," 2016.
- [41] M. A. Green, Y. Hishikawa, E. D. Dunlop, D. H. Levi, J. Hohl-Ebinger, and A. W. Y. Ho-Baillie, "Solar cell efficiency tables (version 52)," *Prog. Photovoltaics Res. Appl.*, 2018.
- [42] C. A. Nelson, N. R. Monahan, and X. Y. Zhu, "Exceeding the Shockley-Queisser limit in solar energy conversion," *Energy and Environmental Science*. 2013.
- [43] A. V. Shah, *Thin-film silicon solar cells*. 2010.
- [44] S. F. K.K., "Solar Frontier Achieves World Record Thin-Film Solar Cell Efficiency: 22.9 %," *Online*, 2017. .
- [45] "NREL." [Online]. Available: <https://www.nrel.gov>.
- [46] B. E. McCandless and J. R. Sites, "Cadmium Telluride Solar Cells," in *Handbook of Photovoltaic Science and Engineering*, 2011.
- [47] G. jiang, J. Bi, M. Song, J. Liu, W. Xiong, and M. Huang, "III-V Multi-Junction Solar Cells," in *Optoelectronics - Advanced Materials and Devices*, 2013.
- [48] M. A. Green, "Third generation photovoltaics: Solar cells for 2020 and beyond," in *Physica E: Low-Dimensional Systems and Nanostructures*, 2002.
- [49] J. Burschka *et al.*, "Sequential deposition as a route to high-performance perovskite-sensitized solar cells," *Nature*, 2013.
- [50] L. Meng *et al.*, "Organic and solution-processed tandem solar cells with 17.3% efficiency," *Science (80-.)*, 2018.
- [51] OXFORD_PV, "Oxford PV sets world record for perovskite solar cell." [Online]. Available: <https://www.oxfordpv.com/news/oxford-pv-sets-world-record-perovskite-solar-cell>.
- [52] P. Ghamgosar, "Advanced Metal Oxide Semiconductors for Solar Energy Harvesting and Solar Fuel Production Experimental physics," Luleå University of Technology, 2017.
- [53] R. Ameta, S. Benjamin, S. Sharma, and M. Trivedi, "Dye-sensitized solar

-
- cells,” in *Solar Energy Conversion and Storage: Photochemical Modes*, 2015.
- [54] A. Pandikumar, S. P. Lim, S. Jayabal, N. M. Huang, H. N. Lim, and R. Ramaraj, “Titania gold plasmonic nanoarchitectures: An ideal photoanode for dye-sensitized solar cells,” *Renewable and Sustainable Energy Reviews*. 2016.
- [55] B. O’Regan and M. Grätzel, “A low-cost, high-efficiency solar cell based on dye-sensitized colloidal TiO₂ films,” *Nature*, 1991.
- [56] L. Han *et al.*, “High-efficiency dye-sensitized solar cell with a novel co-adsorbent,” *Energy Environ. Sci.*, 2012.
- [57] G. Yu, J. Gao, J. C. Hummelen, F. Wudl, and A. J. Heeger, “Polymer photovoltaic cells: Enhanced efficiencies via a network of internal donor-acceptor heterojunctions,” *Science (80-.)*, 1995.
- [58] H. Hoppe and N. S. Sariciftci, “Organic solar cells: An overview,” *J. Mater. Res.*, 2004.
- [59] J. J. M. Halls *et al.*, “Efficient photodiodes from interpenetrating polymer networks,” *Nature*. 1995.
- [60] W. Cao and J. Xue, “Recent progress in organic photovoltaics: Device architecture and optical design,” *Energy and Environmental Science*. 2014.
- [61] M. Hösel, D. Angmo, and F. C. Krebs, “Organic solar cells (OSCs),” in *Handbook of Organic Materials for Optical and (Opto)Electronic Devices: Properties and Applications*, 2013.
- [62] M. T. Dang, L. Hirsch, and G. Wantz, “P3HT:PCBM, best seller in polymer photovoltaic research,” *Adv. Mater.*, 2011.
- [63] K. Mondal and A. Sharma, “Photocatalytic Oxidation of Pollutant Dyes in Wastewater by TiO₂ and ZnO nano-materials – A Mini-review,” *indian Inst. Technol.*, 2016.
- [64] A. Elschner, S. Kirchmeyer, W. Lövenich, U. Merker, and K. Reuter, *PEDOT: Principles and applications of an intrinsically conductive polyme*. 2010.
- [65] S. R. Forrest, “The limits to organic photovoltaic cell efficiency,” *MRS Bulletin*. 2005.
- [66] F. Fariq Muhammad, “Design Approaches to Improve Organic Solar Cells,” *J. Technol. Innov. Renew. Energy*, vol. 3, pp. 63–71, 2014.
- [67] J. P. Correa-Baena *et al.*, “Promises and challenges of perovskite solar cells,” *Science*. 2017.
- [68] Y. Zhao, A. M. Nardes, and K. Zhu, “Solid-state mesostructured perovskite

- CH₃NH₃PbI₃ solar cells: Charge transport, recombination, and diffusion length,” *J. Phys. Chem. Lett.*, 2014.
- [69] T. Dittrich, C. Awino, P. Prajontat, B. Rech, and M. C. Lux-Steiner, “Temperature Dependence of the Band Gap of CH₃NH₃PbI₃ Stabilized with PMMA: A Modulated Surface Photovoltage Study,” *J. Phys. Chem. C*, 2015.
- [70] C. S. Ponseca *et al.*, “Organometal halide perovskite solar cell materials rationalized: Ultrafast charge generation, high and microsecond-long balanced mobilities, and slow recombination,” *J. Am. Chem. Soc.*, 2014.
- [71] M. Shahiduzzaman, “Investigation of Nanoparticles and Interface Effects on Organometal Halide Perovskite Solar Cells Fabricated By Wet Process,” Kanazawa University, 2016.
- [72] D. Bi, L. Yang, G. Boschloo, A. Hagfeldt, and E. M. J. Johansson, “Effect of different hole transport materials on recombination in CH₃NH₃PbI₃ perovskite-sensitized mesoscopic solar cells,” *J. Phys. Chem. Lett.*, 2013.
- [73] J. Liu *et al.*, “Employing PEDOT as the p-type charge collection layer in regular organic-inorganic perovskite solar cells,” *J. Phys. Chem. Lett.*, 2015.
- [74] Y. Zhao, A. M. Nardes, and K. Zhu, “Mesoporous perovskite solar cells: Material composition, charge-carrier dynamics, and device characteristics,” *Faraday Discuss.*, 2014.
- [75] K. Domanski, “The Quest for Stability of Perovskite Solar Cells: Understanding Degradation, Improving Lifetimes and Towards Experimental Standards,” ÉCOLE POLYTECHNIQUE FÉDÉRALE DE LAUSANNE, 2018.
- [76] N. G. Park, “Perovskite solar cells: An emerging photovoltaic technology,” *Materials Today*. 2015.
- [77] S. Rühle *et al.*, “All-oxide photovoltaics,” *Journal of Physical Chemistry Letters*. 2012.
- [78] T. Minami, Y. Nishi, and T. Miyata, “Heterojunction solar cell with 6% efficiency based on an n-type aluminum-gallium-oxide thin film and p-type sodium-doped Cu₂O sheet,” *Appl. Phys. Express*, vol. 8, no. 2, 2015.
- [79] A. Pérez-Tomás, A. Mingorance, D. Tanenbaum, and M. Lira-Cantú, *Metal Oxides in Photovoltaics: All-Oxide, Ferroic, and Perovskite Solar Cells*. Elsevier Inc., 2017.
- [80] H. Wei *et al.*, “Three kinds of Cu₂O/ZnO heterostructure solar cells fabricated with electrochemical deposition and their structure-related photovoltaic

-
- properties,” *CrystEngComm*, vol. 13, no. 20, pp. 6065–6070, 2011.
- [81] S. P. Chang and K. J. Chen, “Zinc oxide nanoparticle photodetector,” *J. Nanomater.*, 2012.
- [82] S. Rudisill, “Metal Oxide Thin Films for LED Applications,” pp. 92–93, 2008.
- [83] L. Petti *et al.*, “Metal oxide semiconductor thin-film transistors for flexible electronics,” *Applied Physics Reviews*. 2016.
- [84] N. Yamazoe, G. Sakai, and K. Shimanoe, “Oxide semiconductor gas sensors,” *Catal. Surv. from Asia*, 2003.
- [85] T. Dimopoulos, *All-Oxide Solar Cells*. Elsevier Inc., 2017.
- [86] J. Lyons, A. Janotti, and C. Van de Walle, “Theory and Modeling of Oxide Semiconductors,” *Semiconductors and Semimetals*. University of California, 2013.
- [87] T. L. Le, “Preparation of transition metal oxide thin films used as solar absorbers,” Université Paul Sabatier-Toulouse III, 2017.
- [88] Q. Zhang, C. S. Dandeneau, X. Zhou, and C. Cao, “ZnO nanostructures for dye-sensitized solar cells,” *Advanced Materials*. 2009.
- [89] A. Janotti and C. G. Van De Walle, “Fundamentals of zinc oxide as a semiconductor,” *Reports Prog. Phys.*, 2009.
- [90] Ü. Özgür *et al.*, “A comprehensive review of ZnO materials and devices,” *J. Appl. Phys.*, vol. 98, no. 4, pp. 1–103, 2005.
- [91] H. Morkoç and Ü. Özgür, *Zinc Oxide: Fundamentals, Materials and Device Technology*. 2009.
- [92] U. O. Hadis Morkoc, *ZnO: Fundamentals, materials and device technology*. 2008.
- [93] A. Janotti and C. G. Van De Walle, “Oxygen vacancies in ZnO,” *Appl. Phys. Lett.*, 2005.
- [94] T. Pauporté, *Synthesis of ZnO Nanostructures for Solar Cells-A Focus on Dye-Sensitized and Perovskite Solar Cells*. Elsevier Inc., 2017.
- [95] C. F. Klingshirn, “ZnO: Material, physics and applications,” *ChemPhysChem*. 2007.
- [96] K. Hashimoto, H. Irie, and A. Fujishima, “TiO₂ photocatalysis: A historical overview and future prospects,” *Japanese J. Appl. Physics, Part 1 Regul. Pap. Short Notes Rev. Pap.*, 2005.
- [97] W. Weppner, “Oxide semiconductors for solar energy conversion: titanium

- dioxide,” *Int. J. Hydrogen Energy*, 2012.
- [98] Y. Bai, I. Mora-Seró, F. De Angelis, J. Bisquert, and P. Wang, “Titanium Dioxide Nanomaterials for Photovoltaic Applications,” *Chem. Rev.*, 2014.
- [99] University of Liverpool, “Copper (I) Oxide-Cu₂O,” *ChemTube 3D*. [Online]. Available: [http://www.chemtube3d.com/solidstate/SS-Cu₂O.htm](http://www.chemtube3d.com/solidstate/SS-Cu2O.htm).
- [100] C. J. Barbé *et al.*, “Nanocrystalline Titanium Oxide Electrodes for Photovoltaic Applications,” *J. Am. Ceram. Soc.*, 2005.
- [101] B. P. Rai, “Cu₂O solar cells: a review,” *Sol. Cells*, vol. 25, no. 3, pp. 265–272, 1988.
- [102] S. Rühle, “Tabulated values of the Shockley-Queisser limit for single junction solar cells,” *Sol. Energy*, 2016.
- [103] P. A. Korzhavyi and B. Johansson, “Literature review on the properties of cuprous oxide Cu₂O and the process of copper oxidation,” *C. Grup. AB*, 2012.
- [104] T. Minami, Y. Nishi, and T. Miyata, “Cu₂O-based solar cells using oxide semiconductors,” *J. Semicond.*, vol. 37, 2016.
- [105] R. J. Iwanowski and D. Trivich†dr, “Enhancement of the photovoltaic conversion efficiency in Cu/Cu₂O schottky barrier solar cells by H⁺ ion irradiation,” *Phys. Status Solidi*, vol. 95, no. 2, pp. 735–741, 1986.
- [106] P. Review and C. Matter, “Electronic structure and bonding properties of cobalt oxide in the spinel structure,” *Phys. Rev. B*, vol. 83, 2015.
- [107] B. Kupfer *et al.*, “Thin film Co₃O₄/TiO₂ heterojunction solar cells,” *Adv. Energy Mater.*, vol. 5, no. 1, pp. 2–6, 2015.
- [108] L. Qiao *et al.*, “Nature of the band gap and origin of the electro-/photo-activity of Co₃O₄,” *J. Mater. Chem. C*, vol. 1, no. 31, pp. 4628–4633, 2013.
- [109] V. Neburchilov, H. Wang, J. J. Martin, and W. Qu, “A review on air cathodes for zinc-air fuel cells,” *Journal of Power Sources*. 2010.
- [110] H. J. Kim and J. H. Lee, “Highly sensitive and selective gas sensors using p-type oxide semiconductors: Overview,” *Sensors and Actuators, B: Chemical*. 2014.
- [111] Y. Liang *et al.*, “Co₃O₄ nanocrystals on graphene as a synergistic catalyst for oxygen reduction reaction,” *Nat. Mater.*, 2011.
- [112] V. R. Shinde, S. B. Mahadik, T. P. Gujar, and C. D. Lokhande, “Supercapacitive cobalt oxide (Co₃O₄) thin films by spray pyrolysis,” *Appl. Surf. Sci.*, 2006.
- [113] J. G. Cook and M. P. van der Meer, “The optical properties of sputtered Co₃O₄

-
- films,” *Thin Solid Films*, 1986.
- [114] Q. C. Liu, J. J. Xu, Z. W. Chang, and X. B. Zhang, “Direct electrodeposition of cobalt oxide nanosheets on carbon paper as free-standing cathode for Li-O₂ battery,” *J. Mater. Chem. A*, 2014.
- [115] A. Bashir *et al.*, “Spinel Co₃O₄ nanomaterials for efficient and stable large area carbon-based printed perovskite solar cells,” *Nanoscale*, 2018.
- [116] T. Minami, Y. Nishi, T. Miyata, and J. I. Nomoto, “High-efficiency oxide solar cells with ZnO/Cu₂O heterojunction fabricated on thermally oxidized Cu₂O sheets,” *Appl. Phys. Express*, vol. 4, no. 6, pp. 2–5, 2011.
- [117] T. Minami, Y. Nishi, and T. Miyata, “Efficiency enhancement using a Zn_{1-x}Ge_xO thin film as an n-type window layer in Cu₂O-based heterojunction solar cells,” *Appl. Phys. Express*, 2016.
- [118] Y. Luo, L. Wang, Y. Zou, X. Sheng, L. Chang, and D. Yang, “Electrochemically Deposited Cu₂O on TiO₂ Nanorod Arrays for Photovoltaic Application,” *Electrochem. Solid-State Lett.*, 2011.
- [119] Z. Zang, “Efficiency enhancement of ZnO/Cu₂O solar cells with well oriented and micrometer grain sized Cu₂O films,” *Appl. Phys. Lett.*, vol. 112, no. 4, 2018.
- [120] Y. Nishi, T. Miyata, and T. Minami, “Effect of inserting a thin buffer layer on the efficiency in n-ZnO/p-Cu₂O heterojunction solar cells,” *J. Vac. Sci. Technol. A Vacuum, Surfaces, Film.*, vol. 30, no. 4, 2012.
- [121] S. Saehana and Muslimin, “Performance improvement of Cu₂O/TiO₂ heterojunction solar cell by employing polymer electrolytes,” *Int. J. Eng. Technol.*, vol. 13, no. 06, pp. 13–16, 2013.
- [122] F. Wei, M. Jiang, and L. Liu, “Facile Hydrothermal Preparation of ZnO/Co₃O₄ Heterogeneous Nanostructures and its Photovoltaic Effect,” *Int. J. Optomechatronics*, vol. 9, no. 3, pp. 211–220, 2015.
- [123] J. Cui, “Zinc oxide nanowires,” *Materials Characterization*. 2012.
- [124] X. Chen *et al.*, “Three-dimensional ordered ZnO/Cu₂O nanoheterojunctions for efficient metal-oxide solar cells,” *ACS Appl. Mater. Interfaces*, vol. 7, no. 5, pp. 3216–3223, 2015.
- [125] J. Cui and U. J. Gibson, “A simple two-step electrodeposition of Cu₂O/ZnO Nanopillar solar cells,” *J. Phys. Chem. C*, vol. 114, no. 14, pp. 6408–6412, 2010.
- [126] W. Jia *et al.*, “P-Cu₂O/n-ZnO heterojunction fabricated by hydrothermal

- method,” *Appl. Phys. A Mater. Sci. Process.*, vol. 109, no. 3, pp. 751–756, 2012.
- [127] M. Abd-Ellah, J. P. Thomas, L. Zhang, and K. T. Leung, “Enhancement of solar cell performance of p-Cu₂O/n-ZnO-nanotube and nanorod heterojunction devices,” *Sol. Energy Mater. Sol. Cells*, vol. 152, pp. 87–93, 2016.
- [128] L. Zhang *et al.*, “Inorganic Solar Cells Based on Electrospun ZnO Nanofibrous Networks and Electrodeposited Cu₂O,” *Nanoscale Res. Lett.*, vol. 10, no. 1, pp. 1–13, 2015.
- [129] K. P. Musselman *et al.*, “Strong efficiency improvements in ultra-low-cost inorganic nanowire solar cells,” *Adv. Mater.*, vol. 22, no. 35, pp. 254–258, 2010.
- [130] M. Pavan *et al.*, “TiO₂/Cu₂O all-oxide heterojunction solar cells produced by spray pyrolysis,” *Sol. Energy Mater. Sol. Cells*, vol. 132, pp. 549–556, 2015.
- [131] G. Haugstad, *Atomic Force Microscopy: Understanding Basic Modes and Advanced Applications*. 2012.
- [132] B. Voigtländer, *Scanning Probe Microscopy: Atomic Force Microscopy and Scanning Tunneling Microscopy*. 2015.
- [133] J. Bhattacharjee, “Atomic Force Microscope: Fundamental Principles,” 2015. [Online]. Available: <https://www.slideshare.net/joybiitk/atomic-force-microscope-fundamental-principles>.
- [134] Y. Seo and W. Jhe, “Atomic force microscopy and spectroscopy,” *Reports Prog. Phys.*, 2008.
- [135] C. Parigger, “Atomic force microscopy,” in *Handbook of Physics in Medicine and Biology*, 2010.
- [136] M. P. Murrell *et al.*, “Spatially resolved electrical measurements of SiO₂ gate oxides using atomic force microscopy,” *Appl. Phys. Lett.*, 1993.
- [137] D. Mikulik *et al.*, “Conductive-probe atomic force microscopy as a characterization tool for nanowire-based solar cells,” *Nano Energy*, vol. 41, pp. 566–572, 2017.
- [138] V. Castagnola, “Implantable microelectrodes on soft substrate with nanostructured active surface for stimulation and recording of brain activities,” Universite Toulouse III Paul Sabatier, 2014.
- [139] A. Alexeev, J. Loos, and M. M. Koetse, “Nanoscale electrical characterization of semiconducting polymer blends by conductive atomic force microscopy (C-AFM),” *Ultramicroscopy*, 2006.
- [140] I. Beinik, “Electrical Characterization of Semiconductor Nanostructures by

-
- Conductive Probe Based Atomic Force Microscopy Techniques,” Montanuniversitat Leoben, 2011.
- [141] M. Lanza, *Conductive Atomic Force Microscopy Applications in Nanomaterials*. Berlin: Wiley-VCH, 2017.
- [142] M. Rezeq, A. Ali, S. P. Patole, K. Eledlebi, R. K. Dey, and B. Cui, “The dependence of Schottky junction (I-V) characteristics on the metal probe size in nano metal-semiconductor contacts,” *AIP Adv.*, 2018.
- [143] M. Pepper, “Metal-semiconductor contacts,” *Phys. Technol.*, 1974.
- [144] D. C. Coffey, O. G. Reid, D. B. Rodovsky, G. P. Bartholomew, and D. S. Ginger, “Mapping local photocurrents in polymer/fullerene solar cells with photoconductive atomic force microscopy,” *Nano Lett.*, 2007.
- [145] L. Heng *et al.*, “Local photoelectric conversion properties of titanylphthalocyanine (TiOPc) coated aligned ZnO nanorods,” *Chem. Commun.*, 2010.
- [146] R. Shao, S. V. Kalinin, and D. a. Bonnell, “Nanoimpedance Microscopy and Spectroscopy,” *MRS Proc.*, vol. 738, pp. 2–8, 2002.
- [147] I. Mora-Seró, G. Garcia-Belmonte, P. P. Boix, M. A. Vázquez, and J. Bisquert, “Impedance spectroscopy characterisation of highly efficient silicon solar cells under different light illumination intensities,” *Energy Environ. Sci.*, 2009.
- [148] L. Fumagalli, I. Casuso, G. Ferrari, G. Gomila, and M. Sampietro, “Nano-scale Impedance Spectroscopy,” pp. 1–2, 2005.
- [149] K. Darowicki, A. Zieliński, and K. J. Kurzydłowski, “Application of dynamic impedance spectroscopy to atomic force microscopy,” *Sci. Technol. Adv. Mater.*, vol. 9, 2008.
- [150] P. Barthelemy, J. Bertolotti, and D. S. Wiersma, “A Lévy flight for light,” *Nature*, 2008.
- [151] L. Vayssieres, “Growth of arrayed nanorods and nanowires of ZnO from aqueous solutions,” *Adv. Mater.*, 2003.
- [152] D. M. Mattox, *Handbook of Physical Vapor Deposition (PVD) Processing*. 1998.
- [153] Sigma Aldrich, “Physical Vapor Deposition (PVD) - Vapor Deposition Precursors | Sigma-Aldrich,” 2015. [Online]. Available: <http://www.sigmaaldrich.com/materials-science/material-science-products.html?TablePage=108832720>.

- [154] D. M. Mattox, "Physical vapor deposition (PVD) processes," *Met. Finish.*, 2000.
- [155] S. Shahidi, B. Moazzenchi, and M. Ghoranneviss, "A review-application of physical vapor deposition (PVD) and related methods in the textile industry," *Eur. Phys. J. Appl. Phys.*, 2015.
- [156] H. O. Pierson, *Handbook of Chemical Vapor Deposition (CVD)*. 1999.
- [157] K. L. Choy, "Chemical vapour deposition of coatings," *Prog. Mater. Sci.*, 2003.
- [158] S. M. George, "Atomic layer deposition: An overview," *Chem. Rev.*, 2010.
- [159] J. R. J. Gainer, "Challenges for Non-Ideal Atomic Layer Deposition Processes and Systems," *Review of Scientific Instruments*, 2013. [Online]. Available: <http://aip.scitation.org/doi/10.1063/1.4774042>.
- [160] R. W. Johnson, A. Hultqvist, and S. F. Bent, "A brief review of atomic layer deposition: From fundamentals to applications," *Mater. Today*, 2014.
- [161] C. de Melo *et al.*, "Local Structure and Point-Defect-Dependent Area-Selective Atomic Layer Deposition Approach for Facile Synthesis of p-Cu₂O/n-ZnO Segmented Nanojunctions," *ACS Appl. Mater. Interfaces*, vol. 10, pp. 37671–37678, 2018.
- [162] Y. Y. Sun, Z. M. Zong, Z. K. Li, Y. P. Zhao, and X. Y. Wei, "Seed-assisted thermal growth of one-dimensional TiO₂ nanomaterials on carbon fibers," *Ceram. Int.*, 2017.
- [163] S. Wang *et al.*, "TiO₂ seed layer for improving the morphology and photovoltaic performance of single-crystal rutile TiO₂ nanorod arrays," *Int. J. ChemTech Res.*, vol. 6, no. 3, pp. 2035–2038, 2014.
- [164] S.-M. Wang, W.-W. Dong, R.-H. Tao, and Z.-H. Deng, "Optimization of single-crystal rutile TiO₂ nanorod arrays based dye-sensitized solar cells and their electron transport properties," *J. Power Sources*, pp. 193–291, 2013.
- [165] NT-MDT, *NTEGRA Probe NanoLaboratory Performing measurements. Instruction manual*. Moscow, Russia, 2011.
- [166] NT-MDT Spectrum Instruments, "NTEGRA." [Online]. Available: <https://www.ntmdt-si.com/products/modular-afm/ntegra-ii>.
- [167] Nanosurf, "Force Spectroscopy." [Online]. Available: <https://www.nanosurf.com/en/support/afm-modes#cantilever>.
- [168] P. Ghamgosar *et al.*, "ZnO-Cu₂O core-shell nanowires as stable and fast response photodetectors," *Nano Energy*, vol. 51, no. April, pp. 308–316, 2018.

-
- [169] Tim Soderberg, “Ultraviolet and visible spectroscopy,” 2017.
- [170] M. Matsuoka, M. Saito, and M. Anpo, “Photoluminescence Spectroscopy,” in *Characterization of Solid Materials and Heterogeneous Catalysts: From Structure to Surface Reactivity, Volume 1&2*, 2012.
- [171] W. Han, H. Jiao, and D. Fox, “Scanning electron microscopy,” in *Springer Tracts in Modern Physics*, 2018.
- [172] H. Stanjek and W. Häusler, “Basics of X-ray diffraction,” *Hyperfine Interact.*, 2004.
- [173] Anton Paar Research, “X-Ray diffraction (XRD).” [Online]. Available: <https://wiki.anton-paar.com/en/x-ray-diffraction-xrd/>.
- [174] E. Smith and G. Dent, *Modern Raman Spectroscopy - A Practical Approach*. 2005.
- [175] T. Luttrell, S. Halpegamage, J. Tao, A. Kramer, E. Sutter, and M. Batzill, “Why is anatase a better photocatalyst than rutile? Model studies on epitaxial TiO₂ films,” pp. 1–8, 2014.
- [176] B. Liu, L. Wen, and X. Zhao, “The photoluminescence spectroscopic study of anatase TiO₂ prepared by magnetron sputtering,” vol. 106, pp. 350–353, 2007.
- [177] K. A. Ali and A. Z. Abdullah, “Visible light responsive TiO₂ nanoparticles modified using Ce and La for photocatalytic reduction of CO₂: Effect of Ce dopant content,” *Applied Catal. A, Gen.*, 2017.